5-1-2015

Constraining the Progenitor and Central Engine of Gamma-ray Bursts with Observational Data

Lu Houjun
University of Nevada, Las Vegas, lhj@physics.unlv.edu

CONSTRAINING THE PROGENITOR AND CENTRAL ENGINE OF GAMMA-RAY BURSTS WITH OBSERVATIONAL DATA

by

HOUJUN Lü

Bachelor of Science
Neijiang Normal University, China
2007

Master of Science
Guangxi University, China
2010

A dissertation submitted in partial fulfillment
of the requirements for the

Doctor of Philosophy - Astronomy

Department of Physics and Astronomy
College of Sciences
The Graduate College

University of Nevada, Las Vegas
May 2015

UNLV | GRADUATE COLLEGE

We recommend the dissertation prepared under our supervision by

Houjun Lu

entitled

Constraining the Progenitor and Central Engine of Gamma-Ray Bursts with Observational Data

is approved in partial fulfillment of the requirements for the degree of

Doctor of Philosophy - Astronomy

Department of Physics and Astronomy

Bing Zhang, Ph.D., Committee Chair

Daniel Proga, Ph.D., Committee Member

Stephen Lepp, Ph.D., Committee Member

Pengtao Sun, Ph.D., Graduate College Representative

Kathryn Hausbeck Korgan, Ph.D., Interim Dean of the Graduate College

May 2015

ABSTRACT

Constraining the Progenitor and Central Engine of Gamma-ray Bursts with Observational Data

by

HOUJUN Lü

Dr. Bing Zhang, Examination Committee Chair
Professor of Physics
University of Nevada, Las Vegas

Gamma-ray bursts (GRBs) are extremely energetic explosions at cosmological distances. We have made great progress in understanding the mysteries of these events since they were discovered more than forty years ago. However, some open questions still remain, e.g. how many classes of GRBs are there, what are the progenitors of these classes, and what is the central engine powering these huge explosions? Thanks to the NASA missions Swift and Fermi, which are used to detect the multi-wavelength emission from these transients, our understanding of GRBs has been greatly advanced. In this dissertation, I use multi-wavelength data to constrain the progenitor and central engine of GRBs. My dissertation consists of three parts: (1) By adding the third dimension "amplitude" as a complementary criterion in classifying GRBs, we test whether some short GRBs are "tip-of-iceberg" of long GRBs, and explain why some high redshift long GRBs have short durations in the rest frame. (2) Using Swift data, we investigate whether the data are consistent with the hypothesis that there exist millisecond magnetar central engines in some long GRBs. We reach the conclusion that at least some long GRBs have a magnetar central engine. (3) We test how well the data are consistent with the magnetar central engine model for short GRBs. We identify that a good fraction of short GRBs have a supra-massive magnetar central engine, which collapses to a black hole after hundreds of seconds. We use the data to constrain the neutron star equation of state.

ACKNOWLEDGMENTS

First and foremost, I would like to express my gratitude to my supervisor Professor Bing Zhang during more than four years of my Ph.D study at the University of Nevada, Las Vegas (UNLV). I was encouraged and inspired to explore astrophysics by his wide knowledge in high energy astrophysics, especially in the domain of Gamma-ray bursts. Bing taught me how to become an astrophysicist, and how to do astrophysics research. He taught me three general rules: confidence, enjoyment and hard work. This is my first time having confidence in myself in spite of not having any astronomy background before my Ph.D study. He always selflessly shared good ideas with me, and helped me clearly interpret many mysteries of astronomy. He helped me discover the methods of doing research, and how to find the truth in life. Furthermore, many thanks to Bing's family for inviting me into their home for Chinese holiday.

Moreover, I should express my sincere thanks to Professor En-Wei Liang, who was my master's degree supervise. His suggestions, ideas, and comments were extremely helpful for me in learning data analysis and statistics. I also acknowledge Dr. Xue-Feng Wu, Dr. Wei-Hua Lei, and Dr.Bin-Bin Zhang who have contributed to my research and daily life. Many thanks to our group members: Dr. Qiang Yuan, Dr. Xiang-Gao Wang, Dr. He Gao, Wei Deng, Ye Li, Hui Sun, Yuan-Pei Yang, Fu-Wen Zhang, Zhi-Bing Zhang, and Lai-Wei Jia. Also Thanks to my collaborator Paul D Lasky.

It is a pleasure to thank the faulty of the Department of Astronomy and Physics

at UNLV, especially to the professors who have taught me graduate courses: Dr. Daniel Proga, Dr. Stephen Lepp, Dr. George Rhee, Dr. Bernard Zygelman, Dr. Lon Spight, and Dr. Kentaro Nagamine. Special thanks also to Dr. Daniel Proga and Dr. Stephen Lepp for serving in my committee. Also thanks to Dr. Peng-Tao Sun, who is another committee member and graduate faculty representative for my dissertation.

Many thanks to my friends and classmates: Timothy Waters, John Boisvert, Sandamali Weerasooriya, Jared Rice, Gabriel Gobeli. It is my honor to share friendship with all of you.

Last, but most importantly, I should express my appreciation to my mother and passed father. They always have the strongest support behind me although they never know what I am studying. Also, thanks to my wife, Cai-Fei Du, for her love and for never leaving or forsaking. Her support and understanding made the end of this dissertation possible.

TABLE OF CONTENTS

LIST OF TABLES

LIST OF FIGURES

PART I

INTRODUCTION

CHAPTER 1

INTRODUCTION TO GAMMA-RAY BURSTS

Gamma-ray bursts (GRBs) are the most luminous events known in the universe. Since they were discovered forty years ago by the Vela satellite (Klebesadel et al., 1973), GRBs became one of the biggest enigmas in astrophysics. Theoretical astrophysicists model the GRBs to interpret the observational data. I will list the detectors of GRBs and their main contributions. I use five time periods to introduce GRB history:

Dark era (1971-1991): The story of GRB discovery is full of excitements. The first GRB was detected in 1967 by the Vela satellite, which was designed to detect Gamma-ray photons from nuclear testing. The GRB signal was found to be short, intense, and had several spikes in $\sim$ MeV band. The first GRB paper was not published until 1973, which indicated the birth of the GRB research. However, without enough localization data for those events, nobody knew where they came from. At that time, more than one hundred models had been proposed to interpret this phenomenology, and the most major problem was the distance scale of the events.

BATSE era (1991-1997): The Compton Gamma Ray Observatory (CGRO) was used to detect Gamma-ray sources in the 20 keV - 2 MeV energy band. The Burst and Transient Source Experiment (BATSE) was one instrument on board CGRO. BATSE detected more than 2704 GRBs from April 1991 to June 2000, providing a large sample for statistical work. During this period, the cosmological origin of GRBs was first established, because it was found that the GRB spatial distribution was apparently isotropic (Meegan et al., 1992). Simultaneously, with a large sample of BATSE data, identified a bimodal distribution of duration was clearly seen. So two classes of GRBs were born: short duration GRBs ($T_{90} < 2$s) with a hard spectrum; and long duration GRBs ($T_{90} > 2$s) with a softer spectrum (Klebesadel et al., 1973). At this time, two different progenitors were proposed to explain the data: Mergers of

compact star (neutron star and neutron stars, or neutron star and black hole systems), and core collapses of massive stars. The fire-ball model (including the internal and external shock models) was also established (Rees & Mészáros, 1992, 1994; Mészáros & Rees, 1993, 1997) during that time.

BeppoSAX era (1997-2004): The breakthrough instruments of GRB research was BeppoSAX, an Italian-Dutch satellite for X-ray and gamma-ray observations. It had led to the discovery of many new features of GRBs: (1) The X-ray and optical afterglows of GRB 970228 were detected, which opened the afterglow window to multi-wavelength emission, and confirmed the cosmological distance of GRBs (Costa et al., 1997). (2) Later, the optical afterglow of GRB 970508 was detected by Keck II, and a metal absorption line from the optical spectrum at $z = 0.835$ was discovered (Metzger et al., 1997). This settled down the distance debate, and the cosmological origin of GRBs was accepted by astronomers. Knowing the distance and observed fluence, one can estimate the total energy of a GRB to be $10^{49} \sim 10^{55}$ erg[1], and the luminosity of prompt emission to be $10^{47} \sim 10^{53}$erg s^{-1} (Zhang & Mészáros, 2004). (3) Another surprise was that GRB 980425 was possibly associated with supernove (SNe) 1998bw (Galama et al., 1998), which provided the first clue of a connection between GRBs and deaths of massive stars. (4) GRB 990123 was the first time when an optical flash was detected, which was predicted by theoretical models (Mészáros & Rees, 1997). In this era, another satellite, High Energy Transient Explorer (HETE II), also contributed to the first solid case of GRB/SN association. i.e. GRB 030329 associated with SN 2003dh (Stanek et al., 2003).

Swift era (2004-now): Swift, a multi-wavelength gamma-ray burst mission was successfully launched on 2004 Nov. 20 (Gehrels et al., 2004). It consists of three instruments: the Burst Alert Telescope (BAT, Barthelmy et al., 2005), used to detect GRBs in the energy band 15 keV to 150 keV; the X-ray Telescope (XRT, Burrows et

[1]Throughout this dissertation, a concordance cosmology with parameters $H_0 = 71$ km s^{-1} Mpc $^{-1}$, $\Omega_M = 0.30$, and $\Omega_\Lambda = 0.70$ is adopted.

al., 2005), which takes images of GRB X-ray afterglow in the range of 0.3 keV to 10 keV; Ultraviolet/Optical Telescope (UVOT, Roming et al., 2005), which detects an afterglow in the optical band. Swift has an accurate localization capacity, thanks to the rapid slews of XRT and UVOT to the position within tens of seconds. The major breakthroughs by Swift include: (1) A canonical X-ray afterglow lightcurve, which is composed of several segments: an early steep decay segment, a shallow decay phase, a normal decay phase, a post jet break and superposed erratic flares (Zhang et al., 2006; Nousek et al., 2006; Burrows et al., 2005). (2) First discovery the afterglow of a short GRB 050509B (Gehrels et al., 2004). (3) The discovery of the high redshift GRBs 080913 at $z = 6.7$ (Greiner et al., 2009), 090423 at $z = 8.2$ (Tanvir et al., 2009; Salvaterra et al., 2009), and 090429B at $z = 9.4$ (Cucchiara et al., 2011). (4) The detection of nearby long-duration GRB 060614, which had soft extended emission more than 100 seconds following a hard spike in the first several seconds, and without association of the supernova at $z = 0.125$ (Gehrels et al., 2006; Gal-Yam et al., 2006).

Fermi era (2008-now): The Fermi satellite opened a new window in high energy astrophysics. It is a NASA mission launched in 2008, and includes two instruments: Gamma-ray Burst Monitor (GBM) and Large Area Telescope (LAT), covering 7 orders of magnitude in energy space (8 keV to 300 GeV). Fermi also had many discoveries by itself: (1) The high energy photons (GeV) from GRBs are delayed relative to lower energy photons (keV - MeV). (2) The evidence of a magnetically dominated outflow in GRB 080916C (Zhang & Pe'er, 2009). (3) The existence of three spectral components in the GRB spectra (Band function, thermal and power-law; Zhang et al., 2011) (4) The existence of a dominant thermal component in GRB 090902B (Ryde et al., 2010).

MULTI-WAVELENGTH OBSERVATIONS

Observation is the foundation of studying the Universe for an astrophysicist. It can help us understand the underlying physical processes. Since the discovery of the cosmological origin of GRBs, GRB research has become one of the most interesting areas in astrophysics, not only because GRBs are the most luminous events ever known in the universe, but also because it is the right time of reaching the data. The contributions from several satellites and other ground-based telescopes help us understand the physical processes behind the phenomena. I will give a brief introduction to the observational properties of prompt emission and afterglow in the temporal and spectral space.

Prompt Emission

Temporal properties: Observationally, the initial γ-ray (or sub-MeV) emission is often called the "prompt emission". The duration of prompt emission is described by T_{90}, which is defined as the time interval between the epochs when 5% and 95% of the total fluence was recorded by the detector (Fig. 1; von Kienlin et al., 2014). It tell us the duration of a burst's prompt emission. The range of duration (T_{90}) from BATSE is milliseconds to thousands of seconds. When analyzing the distribution of T_{90} for all BATSE data, a bimodal distribution is clearly seen. Two Gaussian components are usually used to fit the distribution in the logarithmic space. The separation line is around 2 seconds in the observer frame (Fig. 2. Kouveliotou et al., 1993). GRBs with $T_{90} > 2$s are defined as long GRBs, and those with $T_{90} < 2$s are called short GRBs. Statistically, if one uses the hardness ratio (the ratio between two different energy bands) to figure out the difference between those two classes, one finds that they are clustered in different regions (Fig. 2). The short GRBs are harder, and the long GRBs are softer. If T_{90} is calculated with different instruments, or studied in a different energy band of the same detector, it is found that T_{90} is both

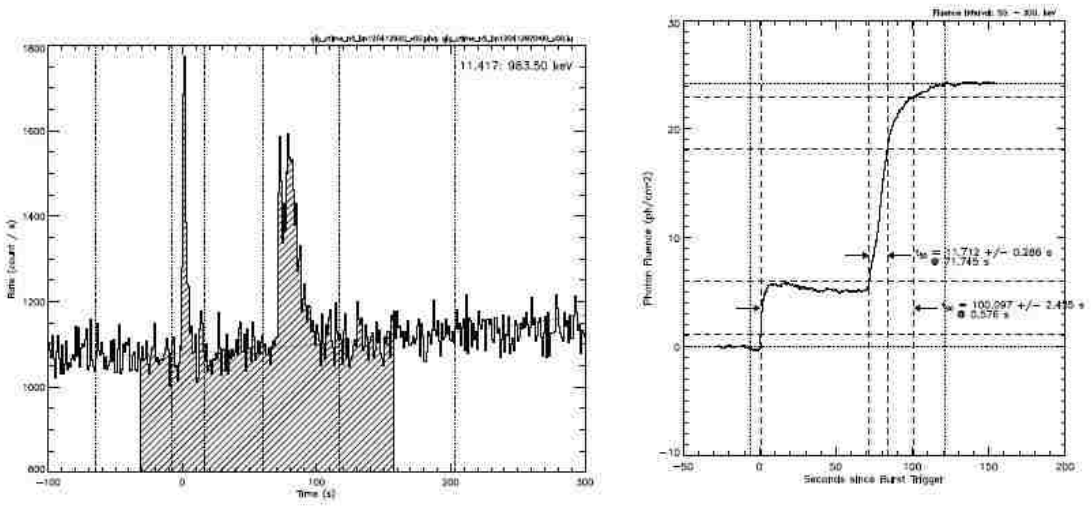

Figure 1 . One example of the definition of T_{90}, taken from Von Kienlin et al., (2014)

energy band and instrument dependent (Fig. 3, Qin et al., 2013).

In the temporal space, the light curves of GRBs are irregular (Fishman & Meegan, 1995), and minimum millisecond (ms) variability can be found if one focus on small time scales. Also, a small fraction of GRBs have precursor emission, which is softer emission before the main burst (Hu et al., 2014). For some short GRBs, more than one hundred second extended emission was found following a hard spike during the first several seconds (Perley et al., 2009). Also, X-ray flares are detected by Swift in a good fraction of GRBs (Burrows et al., 2005). In view of those observations, Zhang et al (2014) proposed $t_{burst} > T_{90}$ to indicate the time scale of the central engine (Fig. 4).

From the theoretical point of view, the prompt emission may be interpreted as collisions between shells (a series of mini-shells), which are unsteady with a distribution of Lorentz factors generated from the GRB central engine (for different velocities). These collisions are supersonic, resulting in internal shocks. The particles are then accelerated by those shocks; this is usually called the internal shock dissipation model (Mészáros & Rees, 1993; Rees & Mészáros, 1994). Alternatively, prompt emission can be proposed by internal collision induced magnetic dissipation (ICMART) Model

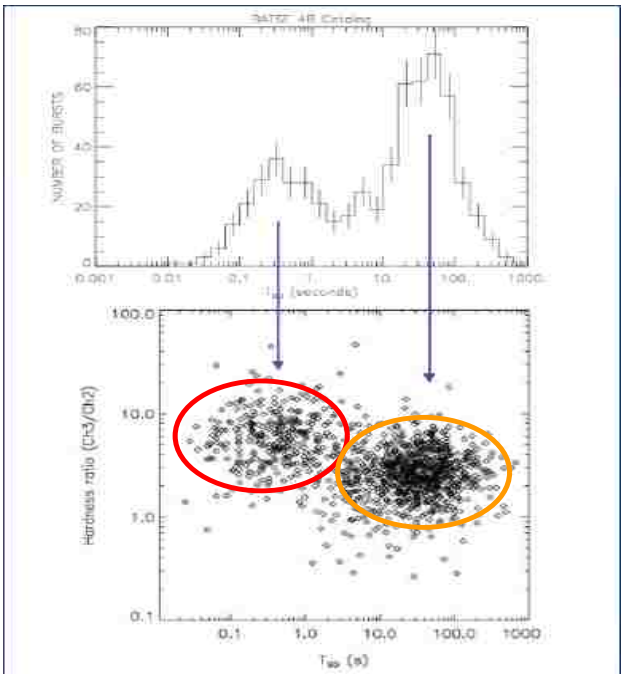

Figure 2 . The duration and hardness distributions of GRBs from BATSE, taken from http://gammaray.msfc.nasa.gov/batse/grb/catalog/

(Zhang & Yan, 2011).

Spectral properties: A thermal spectrum is produced by hot gas in a star in thermal equilibrium. In general, GRB spectra are non-thermal, which means that the higher energy photons do not have an exponentially decreasing distribution, but a power law distribution. It requires a group of accelerated relativistic electrons not in thermal equilibrium. Observationally, the spectra of GRBs can be fit by one empirical function, which was first proposed by Band et al., 1993, called the "Band function". The photon number spectrum can be written as

$$N(E) = \begin{cases} A(\frac{E}{100keV})^{\alpha} exp(-\frac{E}{E_0}), & E < (\alpha-\beta)E_0 \\ A[\frac{(\alpha-\beta)E_0}{100keV}]^{\alpha-\beta} exp(\beta-\alpha)(\frac{E}{100keV})^{\beta}, & E \geq (\alpha-\beta)E_0, \end{cases} \tag{1.1}$$

where A is the normalization of the spectrum, α and β are the photon spectral indices, and E_0 is the break energy in the spectrum. The peak energy (E_p) of spectrum is

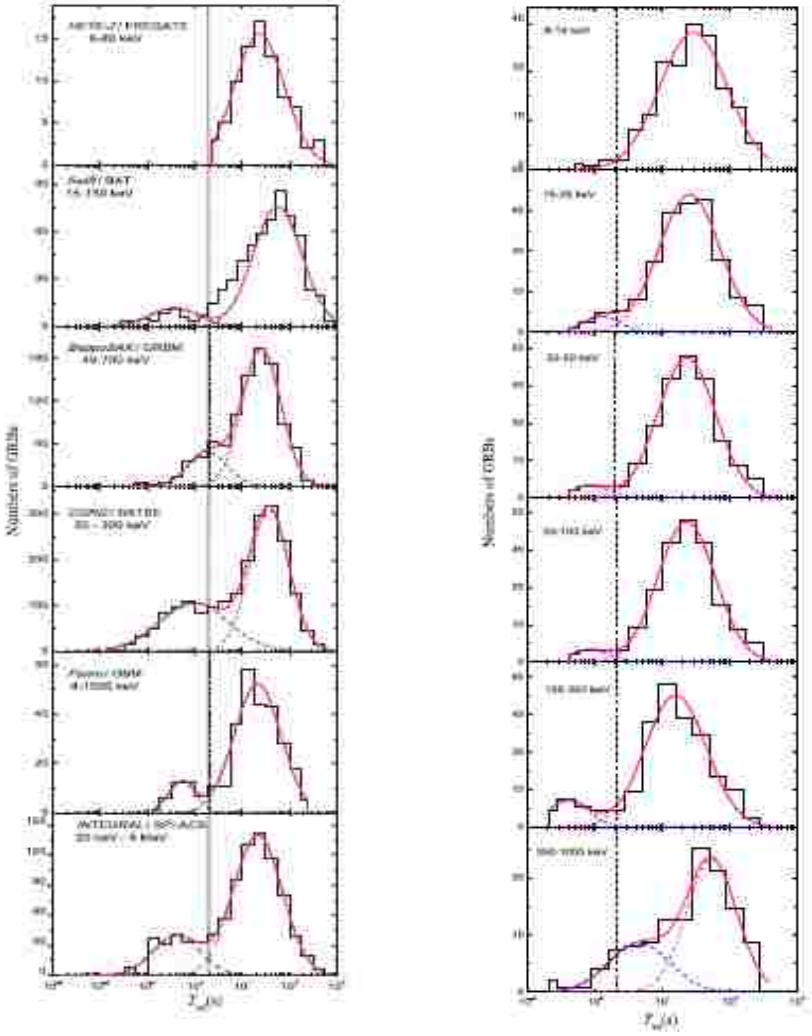

Figure 3 . Left: The T_{90} distribution for different instruments; Right: The T_{90} distribution for different energy bands. Taken from Qin et al., 2013

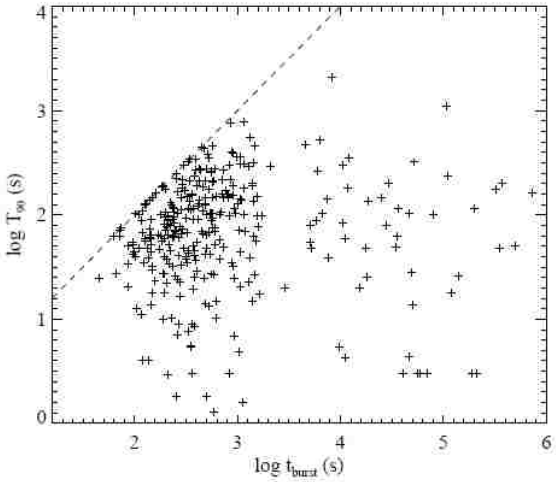

Figure 4 . T_{90} vs t_{burst} for all the bursts in Swift sample. The dashed line marks where $T_{90} = t_{burst}$. Taken from Zhang et al., 2014

related to E_0 by

$$E_p = (2 + \alpha)E_0 \tag{1.2}$$

Fig. 5 shows one example spectrum of GRB 990123 .

If the energy band of the instrument is not broad enough, or GRB is not bright enough, then one can only use a cut-off power law:

$$N(E) = A(\frac{E}{100keV})^{\alpha} exp(-\frac{E}{E_c}) \tag{1.3}$$

or a power law spectrum:

$$N(E) = A(\frac{E}{100keV})^{-\Gamma} \tag{1.4}$$

to fit the spectrum. Here E_c is the cutoff energy, and Γ is the photon index.

If the detector bandpass is wider, richer spectral features are revealed. The spectra of GRB 080916C can be described by a Band function covering 6 orders of magnitude in energy even with the time resolved spectra (Fig. 6, Abdo et al., 2009). GRB 090902B, on the other hand, has a multi-color quasi-thermal spectrum with an added power law component (Fig. 6, Ryde et al., 2010; Zhang et al., 2011). Moreover,

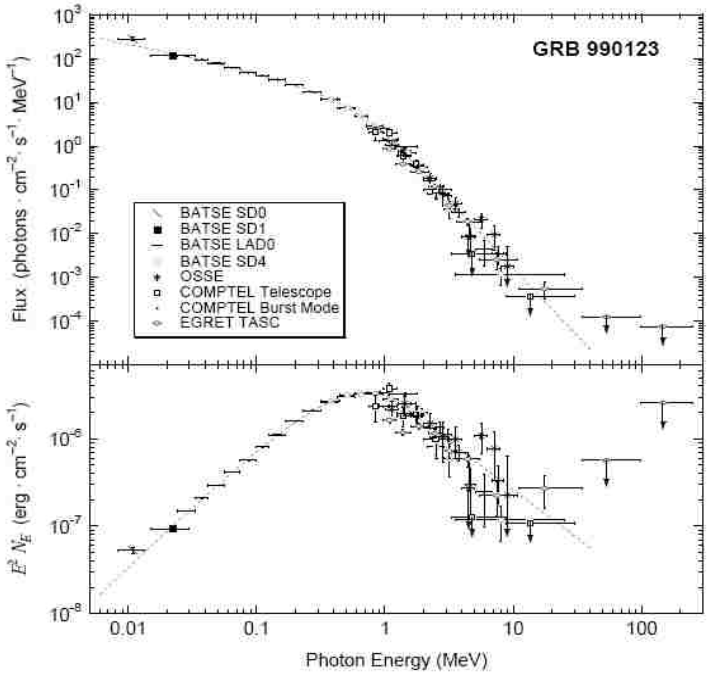

Figure 5 . A typical Band-function spectrum in GRB 990123. From Briggs et al., (1999).

the spectra of some GRBs can be fitted by a Band plus thermal model, or thermal plus power law model (Axelsson et al., 2012). In general, the spectra of GRBs can be composed of three elemental components (Band function, thermal, and power law components) (Fig. 7 Zhang et al., 2011).

Afterglow Emission

Since the discovery of the optical afterglow in 1997, it is now accepted that the Gamma-ray bursts phenomenology is limited not only in the Gamma-ray band, but also extends to long-lived broad band emission (X-ray, optical, infrared, and radio). The longer wavelength emission observed after prompt emission is often called "afterglow emission". From a theoretical view, the afterglow emission is produced in the interaction between the ejecta and the circumburst medium. I will give a brief introduction of broad band afterglow emission from the observational point of view.

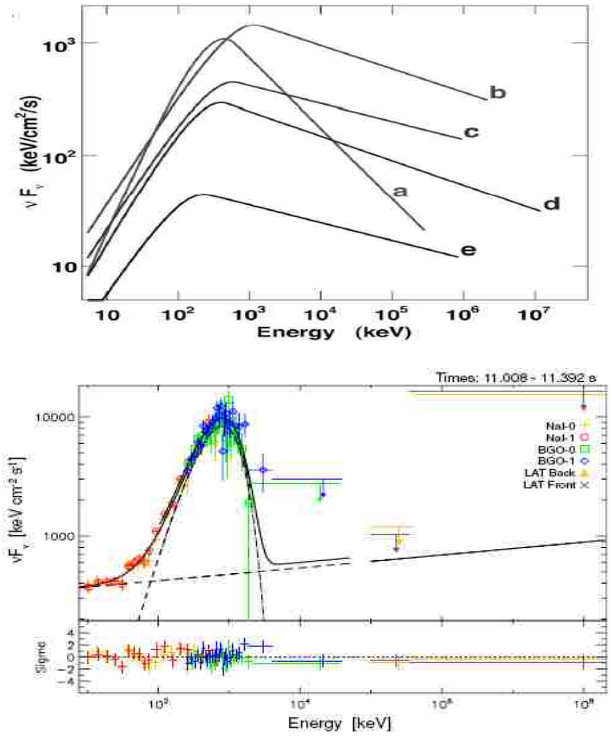

Figure 6 . Top: The best fit spectral Band model for the time-resolved spectra of GRB 080916C, from Abdo et al., 2009. Bottom: A narrow thermal component superposed on a power law for the time-resolved spectra of GRB 090902B, from Ryde et al., 2010.

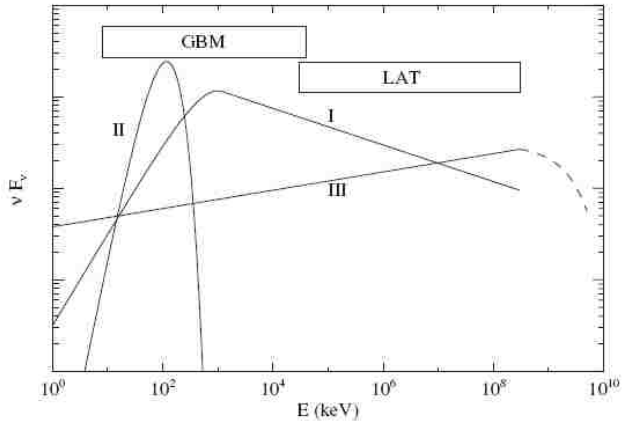

Figure 7 . The three possible elemental spectral components, from Zhang et al., 2011.

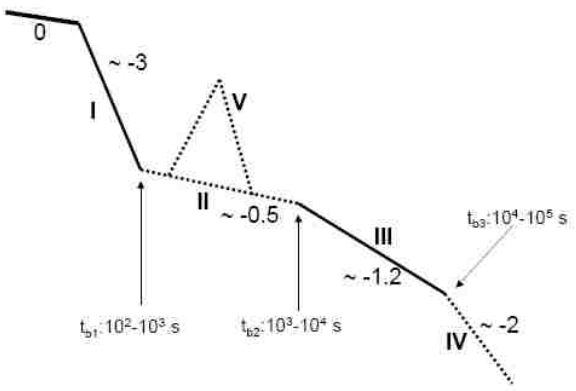

Figure 8 . A canonical X-ray afterglow lightcurve is composed of five segments: I. steep decay; II. shallow decat; III. normal decay; IV. post jet break; V. flares, from Zhang et al., 2006.

X-ray emission: The X-ray band emission is mainly observed by Swift/XRT. The XRT can be slewed to the location within tens of seconds after the BAT trigger, and can help us capture the early X-ray emission. Zhang et al., (2006) summarized a canonical light curve, which is composed of five segments: a steep decay phase, a shallow decay phase, a normal decay phase, a post jet break phase, and superposed erratic flares (Fig. 8).

In the steep decay phase, the temporal decay slope is as steep as t^{-10}, but typically in the range t^{-3} to t^{-8}. The time resolved spectra show that a good fraction of GRBs have a clear hard-to-soft evolution during this phase. In general, the physical origin of this phase is explained as the tail emission of prompt emission, which is high-latitude emission coming later with a time delayed, namely, the "curvature effect" (Fenimore et al., 1996; Kumar & Panaitescu, 2000; Zhang, Liang & Zhang, 2007; Zhang et al., 2006; Qin et al., 2008).

The shallow decay (or plateau) segment has a slope from t^0 to $t^{-0.7}$, and no spectral evolution is seen across the break from this segment to steeper segment afterwards (Liang et al., 2007). The mechanism of this segment is highly debated and still a

mystery. The widely discussed model for this component is energy injection into the external forward shock, either from a long lasting central engine or from an ejecta with a wide distribution of Lorentz factors (Zhang et al., 2006; Nousek et al., 2006; Panaitescu et al., 2006). The internal plateau (a very steep decay following the plateau) was observed by Swift in both long and short GRBs (Troja et al., 2007; Rowlinson et al., 2010). It is very difficult to explain it by an external origin. So Ghisellini et al., (2007) argued that the plateau phase is produced by late internal shocks. It may be a tail of activity of the central engine producing a long time jet with progressively lower power and bulk lorentz factor after the early prompt emission.The internal plateau may be the signature of a magnetar collapse to a black hole (Troja et al., 2007; Rowlinson et al., 2010)

The normal decay and post jet break were observed before Swift. The normal decay phase can be explained very well by the standard external forward shock model, and the post jet break is due to the geometry effect. The X-ray flares are detected in some GRBs (Chincarini et al., 2010; Margutti et al., 2010), showing rapid rises and steep decays. The spectra show a clear hard-to-soft evolution, similar to the prompt emission. These suggest that the X-ray flares have a different origin from the power law decay segment, but a similar origin as prompt emission itself.

Optical emission:

A couple of hours after the BAT trigger, the Swift/UVOT or ground optical telescope can capture optical afterglows. The lightcurve shows a single power law decay with t^{-1}, or a two-segment broken power law (different decay slope). The emission can be explained very well with the standard external shock model. If the GRB is bright enough, or observations are early enough, the lightcurves have found to have more complicated behaviors: First, there is a smooth bump at early times (onset of afterglow, Liang et al., 2010), which can be explained by blastwave deceleration; Second, in GRB such as GRB 990123, a early rising phase with a steep decay is

detected, which is consistent with emission from a reverse shock in the external shock model (Sari & Piran, 1999; Zhang et al., 2003).

High energy emission: By definition high energy photons have energies larger than 100 MeV. The main discovery of high energy emission is from Fermi/LAT. The LAT-band high energy afterglow emission typically shows a power law decay with time (Ghisellini et al., 2010; Zhang et al., 2011). It is explained by the physics of the external forward shock model.

THE PROGENITORS

The progenitors of gamma-ray bursts (GRBs) remain an open question in GRB physics (Zhang, 2011) since the cosmological origin of GRBs was established. The observed fluence and distance can be used to estimate that the isotropic equivalent energies in the gamma-ray band reached $\sim 10^{49} - 10^{55}$ erg. In some GRBs the jet break was observed at late times in the X-ray or optical afterglow. With beaming-correction, the true energy is concentrated around $\sim 10^{49} - 10^{52}$ erg (Zhang & Mészáros, 2004; Meszaros, 2006), which is released in a few seconds. The jet must have a low baryon loading or be Poynting flux dominated in order to be accelerated to relativistic velocities, and the typical Lorentz factors reach more than one hundred. As observational variability timescale can be as short as ms (Fishman & Meagan, 1995), it requires the central engine to be compact. So the basic question is: what are the progenitors that produce these huge explosions? With the observational constraints, the black hole may be the best candidate to power GRBs, which can result from the explosive deaths of massive stars (as in the collapsar model), or remnant of binary compact stars, e.g. neutron star (NS) and black hole (BH) system. For both of them, a spinning black hole is formed and debris from the core collapse of a massive star (or tidally disrupted NS) form a temporary accretion disk or torus. In this situation, the gravitational energy of the in falling material into the black hole is released. The

spin energy of the black hole can be also released by the Blandford-Znajek process (Blandford & Znajek, 1997). Another possible outcome is a "magnetar", which is a rapidly spinning, strongly magnetized neutron star (Usov, 1992).

Massive star core collapses

From observations, it was found that a small fraction of GRBs are associated with SN Type Ic (no hydrogen and helium lines), and broad-band afterglow of long GRBs reveal that their host galaxies are typically irregular galaxies with intense star formation (Fruchter et al., 2006). This strongly suggests that they are likely related to the deaths of massive stars. Theoretically, high angular momentum in the core supports a torus around the black hole resulting from the massive core collapse. The "collapsar" model has been widely accepted to be the standard paradigm for long GRBs (Woosley, 1993; MacFadyen & Woosley, 1999). Collapsars are rotating massive stars (single star or in binary), which within a very short period of time following the collapse (few seconds to minutes), a relativistic jet is powered from a new formed black hole. We can observe the GRB if the jet is directed towards earth. More details on collapsars can be found in Fryer et al., (1999). Here, I only introduce three scenarios of collapsar formation. (1) A single rotating Wolf-Rayet star, with strong wind blown off its hydrogen envelope before its death, leaves a massive helium core, which collapses into a black hole with an accretion disk. It requires the mass of the helium core to be larger than 10 $M_{\odot}$ to make sure the direct formation of black hole without a SN explosion (it is used to interpreted as a failed SN). (2) Binary massive star system with different masses with one star evolving to a white dwarf (WD) or NS, and another blowing off the hydrogen envelope leaving a helium core, which collapses into a black hole. The final outcome may be a binary system consisting of a BH/WD, or BH/NS. (3) Similar to the second case, but just for different initial masses of the stars. Those two stars can evolve to a double helium star system after the common

envelope phase, then two helium stars merge and collapse to produce a GRB.

Compact star mergers

This is the second class of progenitors. From observations, some short GRBs are found to be associated with nearby early-type galaxies with little star formation (Gehrels et al. 2005; Bloom et al., 2006; Barthelmy et al., 2005; Berger et al., 2005), or have a large offset from the host even if they are associated with star forming galaxies. The duration of some short GRBs is as short as one second. There is no evidence of an associated supernova (Kann et al., 2011, Berger, 2014 and references therein).

Theoretically, compact star mergers may have much less residual matter, and be much denser in the core than massive star core collapses. Two compact star mergers can therefore power a short duration explosion. This evidence points towards an origin that does not involve a massive star. The leading scenarios include the mergers of two neutron stars (NS-NS, Paczýnski, 1986; Eichler et al., 1989) or the mergers of a neutron star and a black hole (NS-BH, Paczýnski, 1991).

Mergers of neutron stars: We already know that double NS systems exist in our Galaxy. Given two different masses of stars, one scenario is that both of them blow off their hydrogen envelope, leaving a double helium star binary, then the envelope is ejected and collapses into a double NS system, which later merges to produce the short GRBs (Fryer, Woosley & Hartmann., 1999).

Another scenario is the primary star evolved off main sequence and expanded to a red giant; by the Roche lobe overflow transfer of mass to the secondary star, the envelope is ejected collapse into NS. The secondary also evolved off the main sequence and got the transferred mass from the primary star, evolving to a helium star, whose envelope is ejected and then collapses into a NS. A double NS binary is formed, and later lost the gravitational energy with gravitational wave (GW) radiation, last

merges to produce a short GRB (Gao et al. 2013).

Merger of neutron star and black hole: Paczýnski (1991) suggested the NS-BH merger as one possible source to produce cosmological GRBs. The NS can be tidally disrupted, within this case, the debris forms a disk which releases energy. The evolution of the initial binary system is similar to that of the NS-NS system, only having different initial stellar masses. If one of them forms a BH instead of NS, the system can still produce the gravitational wave and a short GRB at the end.

THE CENTRAL ENGINE

One interesting question is whether different types of progenitors result in different (or common) central engines to power the observed GRBs. Observations of GRB prompt emission and early afterglow can give some constraints on a successful central engine model: (1) Extremely high energy ($\sim 10^{49}-10^{55}$) erg and luminosity of outflow are required (Zhang & Mészáros, 2004); (2) A low baryon loading of ejecta is needed (Lithwick & Sari., 2001); (3) The engine should last for an extended period of time (Burrows et al., 2005; Troja et al., 2007); (4) The outflow needs to be collimated with a jet open angle is about $\sim 1^\circ - 30^\circ$ (Frail et al,. 2001).

Two types of GRB central engine models have been discussed in the literature (e.g. Kumar & Zhang, 2014 for a review). The leading type of model invokes a hyper-accreting stellar-mass black hole (e.g. Popham et al., 1999; Lei et al., 2013). The second type of model invokes a rapidly spinning, strongly magnetized neutron star dubbed a "millisecond magnetar" (Usov, 1992; Dai & Lu, 1998a; Zhang & Mészáros, 2001)

Hyper-accreting black holes

For the black hole-torus central engine, the energy source is the accretion power from the torus. The accretion powered jet luminosity can be estimated as

$$L_{\rm acc} = \zeta \dot{M} c^2 \sim 1.8 \times 10^{52} {\rm erg\ s^{-1}} \eta_{-2} (\frac{\dot{\rm M}}{\rm M_\odot} {\rm s^{-1}}) \tag{1.5}$$

where the η is the efficiency of converting accretion power to radiation power (Kumar & Zhang 2015). Hereafter the convention $Q_s = Q/10^s$ is adopted in cgs units throughout this dissertation. In general, the GRBs can be powered though two mechanisms of a hyper-accreting black hole: (1) Neutrino annihilation model, (2) Blandfod-Znajek mechanism.

Neutrino annihilation Model: To compare with the observed luminosity of GRBs, the typical value of $M_\odot$ is about $(0.01 - 1) M_\odot {\rm s^{-1}}$. This results in an extremely hot plasma, and the photons are trapped in the accretion flow (Katz, 1977; Begelman, 1978; Abramowicz et al., 1988). The higher temperature of the inner disk requires neutrino cooling to be more effective, and cooling can result in the disk temperature going down, and density going up. The geometrical shape is a thin disk. It is called neutrino-dominated accretion flow (NDAF). If the accretion rate ($\dot{M}$) is not high enough, the neutrino cooling becomes not important. The disk will be much thicker, and the thermal energy is advected into the black hole. This situation is called advection-dominated accretion flow (ADAF) (Chen & Beloborodov, 2007). Using the mass conservation equation, energy conservation equation, radial momentum equation, and angular momentum conservation equation, one can derive the structure of GRB accretion disks (see details in Popham et al., 1999 and Narayan et al., 2001). In the NDAF situation, one has enough neutrinos and anti-neutrinos such that neutrino annihilation following the spin axis can drive a hot jet, and the neutrino annihilation

power $\dot{E}_{\nu\bar{\nu}}$ reads (Zalamea & Beloborodov, 2011; Lei et al., 2013)

$$\dot{E}_{\nu\bar{\nu}} \sim 1.1 \times 10^{52} \mathrm{ergs}^{-1} (\frac{M}{M_{\odot}})^{-3/2} (\frac{\dot{M}}{M_{\odot}/s})^{9/4} \tag{1.6}$$

Blandford-Znajek mechanism: The Blandford-Znajek process is a mechanism to extract energy from a rotating black hole (Blandford & Znajek, 1997). The open magnetic field line connect the black hole horizon and a remote load. Because the black hole is rotating, energy and angular momentum can be extracted from the spinning BH. The rotational energy of BH can be written as:

$$E_{rot} = 1.8 \times 10^{54} erg (1 - \sqrt{(1+q)/2}) \frac{M}{M_{\odot}} \tag{1.7}$$

where $q = \sqrt{1 - a_*^2}$, $a_* = \frac{Jc}{GM^2}$ is the BH spin parameter, and J is angular momentum. In general, a_* is less than 1 for rotating BH.

For a BZ process, the jet is Poynting flux dominated. The Poynting flux power can be written as:

$$\dot{E}_{\mathrm{B}} = 1.7 \times 10^{50} a_*^2 (M/M_{\odot})^2 (B_{15}\mathrm{G})^2 F(a_*) \text{ erg s}^{-1}, \tag{1.8}$$

where

$$F(a_*) = [(1+q^2)/q^2][(q + 1/q) \arctan q - 1], \tag{1.9}$$

$q = a_*/(1 + \sqrt{1 - a_*^2})$, and $2/3 \leq F(a_*) \leq \pi - 2$ for $0 \leq a_* \leq 1$. It depends on M, B, and a_*. Estimating the strength of the magnetic field is more difficult; MHD simulations may be the best way to characterize the BZ mechanism of GRBs.

Millisecond magnetars

The second possibility of the GRB central engine invokes a rapidly spinning, highly magnetized neutron star (magnetar). It is required that the initial period $P_0 \sim 1\ ms$ (that is why it is called "millisecond"), and the surface magnetic field $B_p \sim 10^{15}$ G (why it is called "magnetar"). When the magnetar is spinning down, the spin energy is consistent with observed GRB energy (Usov, 1992; Zhang & Mészáros, 2004). The total spin energy can be estimated as

$$E_{\rm rot} = \frac{1}{2} I \Omega_0^2 \simeq 2 \times 10^{52}\ {\rm erg}\ M_{1.4} R_6^2 P_{0,-3}^{-2}, \tag{1.10}$$

where I is the moment of inertia, $\Omega_0 = 2\pi/P_0$ is the initial angular frequency of the neutron star, $M_{1.4} = M/1.4 M_\odot$.

Assuming that the magnetar with initial spin period P_0 is being spun down by a magnetic dipole with surface polar cap magnetic field B_p, the spindown luminosity will evolve with time as Zhang & Mészáros, (2001)

$$\begin{aligned} L(t) &= L_0 \frac{1}{(1+t/\tau)^2} \\ &\simeq \begin{cases} L_0, & t \ll \tau, \\ L_0 (t/\tau)^{-2}, & t \gg \tau. \end{cases} \end{aligned} \tag{1.11}$$

where

$$L_0 = 1.0 \times 10^{49}\ {\rm erg\ s^{-1}} (B_{p,15}^2 P_{0,-3}^{-4} R_6^6) \tag{1.12}$$

is the characteristic spindown luminosity, and

$$\tau = 2.05 \times 10^3\ {\rm s}\ (I_{45} B_{p,15}^{-2} P_{0,-3}^2 R_6^{-6}) \tag{1.13}$$

is the characteristic spindown time scale.

The spin-down behavior of the magnetar can leave characteristic imprints in the observed GRB emission. Dai & Lu, (1998a) first proposed an energy injection model of millisecond pulsars for interpreting a rebrightening feature of the first optical afterglow detected in GRB 970228. Zhang & Mészáros (2001) studied energy injection from a central engine with a general luminosity law $L(t) = L_0(t/t_0)^{-q}$ (the magnetar injection corresponds to $q = 0$ for $t < \tau$ and $q = 2$ for $t > \tau$). They pointed out that besides the rebrightening feature discussed by Dai & Lu, (1998a,b), one can have a shallow decay phase followed by a normal decay phase in the early afterglow of a GRB for typical magnetar parameters. Such a shallow decay phase (or plateau) was later commonly observed in Swift early XRT light curves (Zhang et al., 2006; Nousek et al., 2006; O'Brien et al., 2006; Liang et al., 2007). It can be readily interpreted as energy injection from a millisecond magnetar central engine (Zhang et al., 2006). More details on testing the magnetar central engine model with data are presented in PART (II).

PART II

RESEARCH

CHAPTER 2

THE "AMPLITUDE" PARAMETER OF GAMMA-RAY BURSTS AND ITS IMPLICATIONS FOR CLASSIFICATION

This chapter is part of the following published paper :

Hou-Jun Lü., Zhang B., En-Wei Liang., Bin-Bin Zhang., Takanori Sakamoto., 2014, Monthly Notices of the Royal Astronomical Society 442,1922

Traditionally, gamma-ray bursts (GRBs) are classified based on duration (T_{90}) and hardness ratio (HR) of their prompt gamma-ray emission. In the CGRO/BATSE era, GRBs were classified into two categories in the T_{90}-HR two-dimensional plane (Kouveliotou et al. 1993) with a rough separation in the duration dimension at $T_{90} \sim 2$ s. Long GRBs are typically soft while short GRBs are typically hard, so that the two classes cluster in two regions in the T_{90}-HR plane. Such a distribution is energy-dependent and instrument-dependent (e.g. Qin et al. 2013; Zhang et al. 2012). A third, intermediate class has been suggested by various authors based on the duration criterion alone (e.g. Mukherjee et al. 1998; Horvath 1998; Hakkila et al. 2000; Horvath et al. 2010).

Broad-band afterglow observations of long GRBs reveal that their host galaxies are typically irregular galaxies with intense star formation (Fruchter et al. 2006). Some long GRBs are firmly associated with Type Ib/c supernova (e.g. Hjorth et al. 2003; Stanek et al. 2003; Campana et al. 2006; Pian et al. 2006; Xu et al. 2013). This strongly suggests that they are likely related to the deaths of massive stars, and the "collapsar" model has been widely accepted to be the standard paradigm for long GRBs (Woosley 1993; MacFadyen & Woosley 1999). Detections of afterglows and host galaxies of short GRBs in the Swift (Gehrels et al. 2004) era have advanced our understanding of their physical origin. Some short GRBs are found to be associated with nearby early-type galaxies with little star formation (Gehrels et al. 2005; Bloom et al. 2006; Barthelmy et al. 2005; Berger et al. 2005), or have a large offset from

the host even if they are associated with star forming galaxies (e.g. Fox et al. 2005; Fong et al. 2010). Deep upper limits of their supernova signals are obtained (Kann et al. 2011, Berger 2014 and references therein). This points towards an origin that does not involve a massive star. The leading scenario is mergers of two neutron stars (Paczýnski 1986; Eichler et al. 1989) or mergers of a neutron star and a black hole (Paczýnski 1991b). There is no evidence that the intermediate third class forms a physically distinct population of GRBs.

Further observations revealed a more complicated picture, suggesting that duration is no longer a reliable indicator of the physical origin of a GRB. The detections of two nearby long-duration GRBs without association of a supernova, i.e. GRB 060614 ($T_{90} \sim 100$ s at $z = 0.125$) and GRB 060505 ($T_{90} = 4$ s at $z = 0.089$), cast doubts on that all long GRBs are of a massive star origin (Gehrels et al. 2006; Gal-Yam et al. 2006; Fynbo et al. 2006; Della Valle et al. 2006). On the other hand, some properties of GRB 060614 (e.g. short spectral lag, Gehrels et al. 2006) and the large offset from the star forming region in the host (Gal-Yam et al. 2006) are consistent with being a compact star origin. Zhang et al. (2007b) showed that if GRB 060614 were somewhat less energetic, it would appear as quite similar to GRB 050724, which is the "smoking gun" short GRB (with extended emission) that suggests a compact star origin (Barthelmy et al. 2005; Berger et al. 2005). Later, several high-z GRBs with the rest frame duration $T_{90}/(1+z)$ shorter than 2 s were discovered: GRB 080913 at $z = 6.7$ with $T_{90} = 8$ s (Greiner et al. 2009), GRB 090423 at $z = 8.2$ with $T_{90} = 10.3$ s (Tanvir et al. 2009; Salvaterra et al. 2009), and GRB 090429B at $z = 9.4$ with $T_{90} = 5.5$ s (Cucchiara et al. 2011), but various arguments suggest that they are of a massive star origin (Zhang et al. 2009). Later, more traditional short GRBs are found to be likely of a massive star origin. For example, GRB 090426, at $z = 2.609$, is found to have an observed BAT band duration $T_{90} = 1.2 \pm 0.3$s and a rest frame duration $T_{90}/(1+z) \sim 0.33$ s, but its other properties are fully consistent with being

of a massive star origin (Levesque et al. 2010; Xin et al. 2011; Thöne et al. 2011).

In view of these complications, Zhang (2006) and Zhang et al. (2007b) suggested to classify GRBs physically into Type II (massive star origin) and Type I (compact star origin). Zhang et al. (2009) studied the statistical properties of the Type II and Type I Gold Samples, and found that although the Type II Gold sample tracks the bulk of long GRBs well, the Type I Gold sample is not a good representative of the short GRBs. They suggested a set of multi-wavelength criteria to diagnose the physical origin of GRBs (see also Kann et al. 2011), and suspected that some, maybe most high-redshift high-luminosity short GRBs would be of a Type II origin. This conclusion was later also drawn by several groups independently based on very different arguments (Virgili et al. 2011; Cui et al. 2012; Bromberg et al. 2012).

Even though the multi-wavelength criteria can give more definite clues about the origin of a GRB, they are not available promptly after the trigger of the GRB. Some criteria that carry most weight (e.g. supernova signature, host galaxy information) need late, deep optical observations. It is still useful to apply the prompt gamma-ray data to dig out more information, which may be helpful to infer the physical origin of a GRB. For example, in Lü et al. (2010), we have proposed a new observational parameter ε defined by $E_{\gamma,iso}/E_{p,z}^{5/3}$, where $E_{\gamma,iso}$ is the burst isotropic gamma-ray energy and $E_{p,z}$ is the rest-frame spectral peak energy. This parameter has a cleaner bimodal distribution, and the two types of burst classified with the ε criterion match the physical classification scheme (Type I vs. Type II) better. This method still needs the redshift information.

In this chapter, we propose to add a third dimension "amplitude" into consideration to classify GRBs using the prompt gamma-ray data (see a preliminary discussion in Zhang 2012). The motivation is to study the possibility that a real long GRB may be observed as a "short" one if the majority of emission episode is too faint to be

detected above the background. We call this the "tip-of-iceberg" effect[1]. To quantify this effect, we introduce a new "amplitude parameter" f, and study the distribution of *Swift* GRBs in the three-dimensional (T_{90} − HR − f) space. Then, we introduce an effective amplitude parameter $f_{\rm eff}$ to discuss the range of amplitude if a long GRB is observed as "short" due to the tip-of-iceberg effect. We compare the range of f distribution of short GRBs and the $f_{\rm eff}$ distribution of long GRBs and suggest a confusion regime of f where an observed short GRB may be in fact long. We define a parameter $f_{\rm eff,z}$ by "moving" GRBs with known redshift to higher redshifts through simulations until they become "rest-frame short" GRBs. We take GRB 080319B as an example, and show that long GRBs can become rest-frame short GRBs at high enough redshifts, but with a moderately large f. We show that this is consistent with the three highest-z GRBs: 080913, 090423 and 090429B. We draw conclusions in later section with some discussion.

The amplitude parameter f

In the previous T_{90}-HR two-dimensional diagram, the amplitude information of GRBs is missing. Some GRBs can be very bright, while some others can be faint and barely above the threshold. A bright burst can have more emission episodes emerging above the background, so for a same observed T_{90}, a fainter burst may be intrinsically longer than a brighter burst. So this third dimension, i.e. the "amplitude", carries important information and should be introduced in GRB classification studies. Such a fluence truncation effect has been studied extensively in the past (e.g. Koshut et al. 1996; Bonnell et al. 1997; Hakkila et al. 2000; Schmidt 2001).

[1]In the early BATSE era, some authors had introduced the effective amplitude parameters such as V/V_{max} or C_{max}/C_{min} to perform statistical analyses, but the purpose of their studies was to test for the uniformity of the GRB spatial distribution (e.g. Schmidt et al. 1988; Paczynski 1991a).

Here we quantify such an effect by defining an amplitude parameter

$$f \equiv \frac{F_p}{F_B}, \tag{2.1}$$

where F_p is the 1-second peak flux on the gamma-ray emission lightcurve, and F_B is the average background flux of the burst. Both fluxes are in units of count rate.

We systematically process the *Swift* Burst Alert Telescope (BAT) GRB data to extract lightcurves. We developed an IDL script to automatically download and maintain all the *Swift* BAT data. We use the standard HEAsoft tools (version 6.12) to process the data. By running *bateconvert* from the HEASoft software release, we obtain the energy scale for the BAT events. The lightcurves are extracted by running *batbinevt* (Sakamoto et al. 2007). For each burst, we calculate the cumulative distribution of the source count using the arrival times of a fraction of 5% and 95% of the total counts to define T_{90} (see Fig. 13). The time bin size is fixed to 64 ms for all the bursts. Background is extracted using two time intervals, one before and one after the burst. By fitting the background as a Poisson noise, one can obtain its standard deviation. The error of f is derived from the error of F_B based on error propagation.

Our sample includes the GRBs detected by *Swift* BAT from December 2004 to December 2011. We only selected 437 GRBs with S/N ratio higher than 5, which include 395 long GRBs and 42 short GRBs. Among them, 182 have redshift measurements. For each GRB, we fit the background flux level F_B using the time intervals before and after the burst. This background is burst-dependent, but is around a value of 8000 cts/s. For a small fraction (6.8%) of the bursts, the background before and after the burst is uneven. This is because some bright hard X-ray sources could be entering or exiting the BAT field of view during the slew. For these cases, we fit the background before and after the burst with a straight line with a slope. F_B is defined

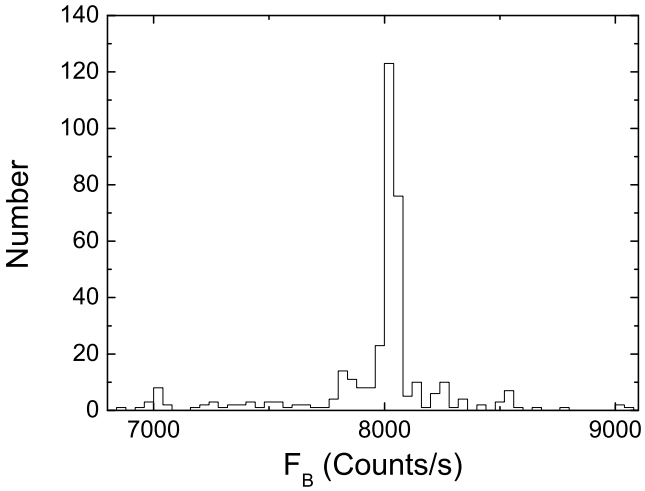

Figure 9 . The histogram of F_B for all the GRBs in our sample.

by fitted background flux at the peak time[2]. Figure 9 shows the histogram of F_B for all the GRBs in our sample.

The f values of the GRBs in our sample are presented the following website (http://grb.physics.unlv.edu/f/data.txt). The $T_{90}-\mathrm{HR}-f$ 3-dimensional distribution diagram of *Swift* GRBs is shown in Figure 10. Long and short GRBs are denoted as black and white symbols. The projections in the $T_{90}-\mathrm{HR}$, $T_{90}-f$ and $\mathrm{HR}-f$ planes are denoted in red, green, and blue colors, respectively, with long and short GRBs denoted by the filled and open symbols, respectively. In Figure 11a, we show 1D distribution (T_{90} and f), and 2D ($T_{90}-f$) diagram with different symbols denoting different types of GRBs: gray for long GRBs, red for short GRBs, blue for short GRBs with extended emission (T_{90} calculated by excluding the extended emission), purple for the three "rest-frame short" ($T_{90}/(1+z) < 2$ s) high-z GRBs, black for other "rest-frame short" GRBs, and two special GRBs, 090426 and 060614, are marked separately.

[2]This flux level is usually slightly higher than the "true" background level due to the source contamination. However, this is not a concern for our analysis, since we are investigating the tip-of-iceberg effect with respect to the background at the detection time.

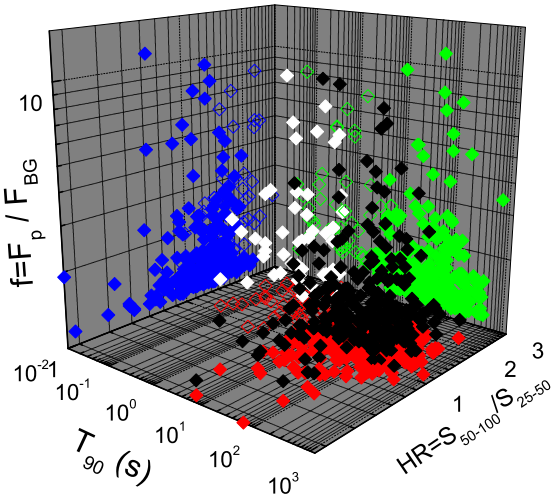

Figure 10 . The $T_{90} - \mathrm{HR} - f$ 3D distribution of the *Swift* GRBs in our sample. Long and short GRBs are denoted as solid black and white diamonds, respectively. Their projections to the $T_{90} - \mathrm{HR}$, $T_{90} - f$, and $\mathrm{HR} - f$ 2D planes are denoted in red, green and blue colors, respectively, with the long and short GRBs denoted with solid and open sympols, respectively.

The distributions of the f-parameter for both long and short GRBs are presented in Figure 12a. As expected, Most bursts are clustered around small f values, and only a small fraction of bursts have $f > 3$. The f distribution can be roughly fit as a power law function, i.e. $N(f) \propto f^{-a}$, with $a \sim 3.54$ for long GRBs and $a \sim 1.66$ for short GRBs. The mean value of f is $\bar{f} = 1.48$ for long GRBs and $\bar{f} = 1.82$ for short GRBs. The largest f values for both long and short GRBs are around 10. The relative paucity of small f for short GRBs may be understood as a selection effect (Sakamoto et al. 2008, 2011): Short GRBs are detected via "rate triggers", which require a relatively large f value to meet the trigger criterion. On the other hand, long GRBs can be caught via "imaging triggers" near the threshold, so that they can be detected with lower f values close to unity.

Although the average value f of long GRBs is smaller than short GRBs, and the $N(f) \propto f^{-a}$ slope of the two populations are considerably different, one cannot

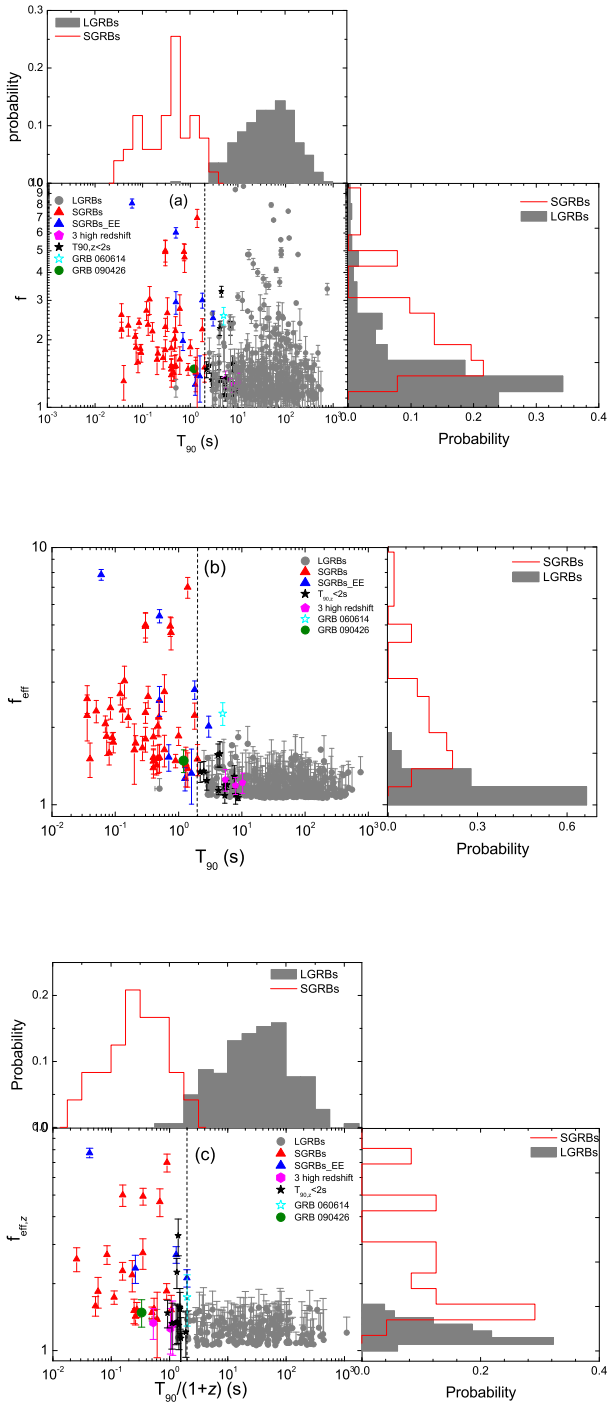

Figure 11 . The 1D and 2D distributions for the bursts in our sample. (a): The $T_{90} - f$ diagram of the GRBs in our sample. (b) The $T_{90} - f_{\rm eff}$ diagram of GRBs in our sample. (c) The $T_{90}/(1+z) - f_{\rm eff,z}$ diagram of GRBs in our sample. The following convention is adopted for all three plots: Gray: long GRBs, red: short GRBs; blue: short GRBs with extended emission; purple: three GRBs with the highest z; black: "rest-frame short" GRBs. GRB 060614 and GRB 090426 are marked with special symbols. The vertical dashed line is the 2 s separation line.

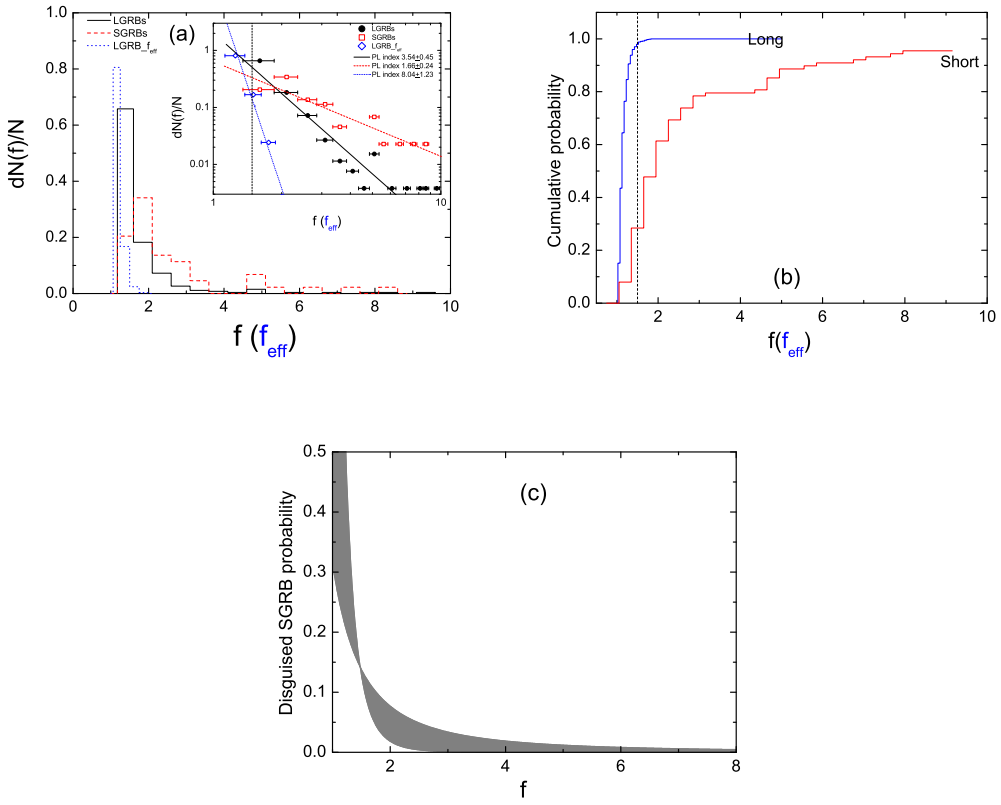

Figure 12 . (a) The distributions of f (for both long and short GRBs) and $f_{\rm eff}$ (for long GRBs only) as well as their power law fits (inset). (b) The cumulative probability of a GRB below a certain f (for short GRBs) or $f_{\rm eff}$ (for long GRBs) value. The vertical line corresponds to $f = 1.5$. (c) Chance probability of a disguised short GRB below a certain f value. The gray region is the error zone for the probability.

significantly improve the duration classification scheme with the introduction of the f value. As shown below, when introducing the next parameter $f_{\rm eff}$, one can gain useful information to judge the true duration category of a GRB, especially for short GRBs.

Effective amplitude $f_{\rm eff}$ of long GRBs, and short-GRB confusion

A long GRB may be confused as a short GRB if only its brightest spikes with duration shorter than 2 s are above the background. To quantify such a tip-of-iceberg

effect, we define an "effective amplitude" of a *long* GRB as

$$f_{\rm eff} \equiv \frac{F'_p}{F_B}. \tag{2.2}$$

Here F'_p is the 1-second peak flux of a pseudo GRB, which is re-scaled down for multiplying by a factor $\epsilon(\epsilon < 1)$ from an original GRB lightcurve until its signal above the background has a duration $T_{90,\rm eff}$ just shorter than 2 s. The physical meaning of the pseudo GRB is an otherwise identical GRB at the same redshift, except that the amplitude is lower by a factor ϵ. Since a short GRB has T_{90} shorter than 2 s, if one defines a $f_{\rm eff}$ parameter for a short GRB, it is identical to f. So we only define $f_{\rm eff}$ for long GRBs.

Technically, the $f_{\rm eff}$ parameter of a long GRB is measured based on the following procedure. (1). We extract the lightcurve of an observed GRB following the standard procedure with a time bin 64 ms; (2). We "re-scale" down the observed lightcurve to reduce the flux at each time bin by multiplying the flux by a factor ϵ ($\epsilon < 1$) for each time bin, and make a "signal" of a pseudo-GRB. (3). We simulate a Poisson background based on the extracted background information (the mean flux and standard deviation), and add this background to the "signal" and derive an "observed" lightcurve of the pseudo GRB; (4). For this simulated "observed" lightcurve, we apply the standard "curve of growth" method by accumulating net fluence above the back ground (e.g. von Kienlin et al. 2014). The duration T_{90} of the pseudo-GRB is obtained through measuring the time interval between 5% and 95% fluence; 5. We progressively multiply by a factor $\epsilon_i(\epsilon_i < 1)$ with the original light curve, each time record T_{90} until the derived T_{90} of the pseudo GRB is below 2 s. Record the f value of this pseudo GRB and define it as $f_{\rm eff}$.

Figure 13 shows the long GRB 050525A as an example. The original burst is shown in Figure 13a, which has an $f = 9.43$. Figure 13b shows a pseudo GRB after

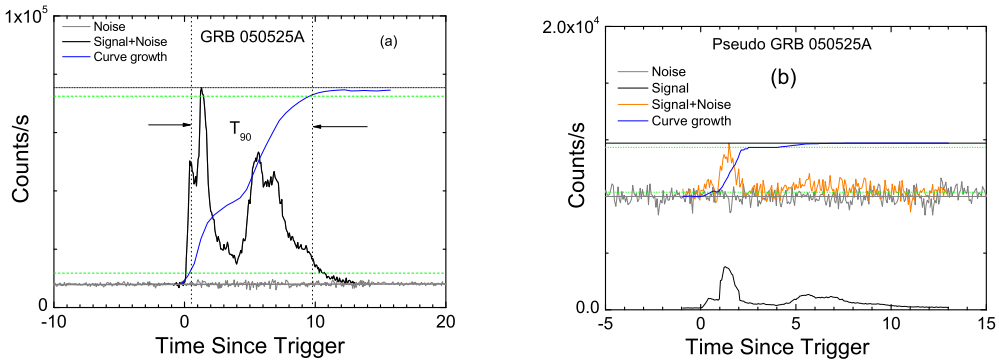

Figure 13 .An example of defining $f_{\rm eff}$ with GRB 050525A. (a) The original lightcurve and the definition of T_{90} using the standard "curve of growth" method. (b) The pseudo GRB generated from GRB 050525A. The original lightcurve is scaled-down by a factor of 0.06 (thin black curve). Adding the background (grey), the total lightcurve (orange curve) is the "observed" lightcurve of the pseudo GRB. Applying the curve of growth method, the T_{90} of the pseudo GRB is just shorter than 2 s. The f parameter of the pseudo GRB, which is $f_{\rm eff}$ of GRB 050525A, is measure as 1.53.

re-scaling it down by a factor of $\epsilon = 0.06$. The signal (thin black curve in Figure 13b) is below the background level F_B (the gray curve). The sum of the signal and background gives a new "observed" lightcurve (the orange curve) of the pseudo GRB, whose T_{90} is measured through the curve of growth method. Only the main peak is within the $5\% - 95\%$ window. The measured T_{90} is just shorter than 2 s. We then measure the f value of this pseudo burst, which is the effective amplitude of the original burst. For this example, one measures $f_{\rm eff} = 1.53$.

Figure 11b gives the 1D distributions of $f_{\rm eff}$, and the $T_{90} - f_{\rm eff}$ distribution of long GRBs together with the $T_{90} - f$ distribution of short GRBs in our sample. The $f_{\rm eff}$ values of long GRBs are systematically smaller than the f values of short GRBs. The $f_{\rm eff}$ distribution histogram of long GRBs is also shown in Fig.4a, which has a mean value $\bar{f}_{\rm eff} = 1.24$, and the steepest slope $a = 8.04 \pm 1.23$ as compared with f distributions of long and short (see inset of 12a).

One immediate conclusion from Figure 11b and Figure 12a is that the distribution of $f_{\rm eff}$ of long GRBs is very different from the f distribution of short GRBs. Most

short GRBs have larger f values than the $f_{\rm eff}$ values of long GRBs. This suggests that the majority of short GRBs are *not* tip-of-iceberg of long GRBs. Instead, they reflect the intrinsically short duration of the central engine. Nonetheless, at smaller f values for short GRBs, confusion would appear since some long GRBs may show up as "disguised" short GRBs due to the tip-of-iceberg effect. In Figure 12b, we present the cumulative probability distribution of f for short GRBs and $f_{\rm eff}$ for long GRBs. It is clearly shown that most long GRBs have small $f_{\rm eff}$ values, e.g. $\sim 95\%$ below 1.5. In contrast, only $\sim 30\%$ short GRBs have $f < 1.5$.

In order to quantify the chance probability of disguised short GRBs, we carry out a Monte Carlo simulation. Since the observed short GRBs may include both intrinsic and disguised short GRBs, we assume an f distribution $N(f) \propto f^{-\alpha}$ for the intrinsic short GRBs, with the slope α taken as a parameter to be constrained by the data. We then simulate 10^4 short GRBs whose f distribution follows this distribution. Next, we simulate a certain amount of disguised short GRBs whose f-distribution satisfies the $f_{\rm eff}$ distribution of long GRBs. The observed short GRBs should be a superposition of the intrinsic and disguised short GRBs. In order to calibrate the two population, we notice that there are 7 observed short GRBs that have $f < 1.5$, and one of them (GRB 090426) is a disguised short GRB (Levesque et al. 2010; Xin et al. 2011; Thöne et al. 2011) with $f = 1.48$. The chance probability for a disguised short GRB at $f \leq 1.5$ is therefore $P(f < 1.5) \sim 1/7 \sim 0.142$. With this calibration, we obtain the "observed" short GRB sample by superposing the simulated intrinsic and disguised short GRB samples. We require that f distribution of this "observed sample" satisfies the observed f distribution, whose slope is ~ 1.66. We find that the α value of the simulated intrinsic short GRBs is only slightly shallower, with $\alpha \sim 1.61$. This is understandable, since essentially all the observed short GRBs at $f > 1.5$ are intrinsic ones, and they define the slope of the f-distribution of the intrinsic short GRB sample. After reaching consistency with the data, we track the

fraction of intrinsic and disguised short GRBs in the total simulated sample to map the chance probability of disguised short GRB below any f value. This probability function reads

$$P(< f) \sim 0.78^{+0.71}_{-0.4} f^{-4.33\pm1.84} \tag{2.3}$$

Since the f and $f_{\rm eff}$ distribution indices have errors, the chance probability in Eq.(2.3) also have errors. The coefficient error and the index error are correlated. All the relations in any case allow $P(f < 1.5) = 0.142$ (see Figure 12c). One can see that the chance probability for contamination can reach 78% near $f = 1$. So for detected short GRBs with a small f value (say $f < 1.5$), one should be cautious to draw conclusion about the duration category of the GRB.

It is interesting to note that GRB 060614 (Gehrels et al. 2006), the peculiar long GRB without supernova association, has $f_{\rm eff} = 1.75$. This means that its tip-of-iceberg still has a large f to be consistent with the short GRB f distribution. Indeed, by scaling it down, it looks like a short GRB with extended emission (Zhang et al. 2007b). Our analysis again supports the Type I (compact star) origin of this GRB.

The $f_{\rm eff,z}$ parameter and "rest-frame short" GRBs

Some long GRBs have a rest-frame duration $T_{90}/(1+z) < 2$ s. The three GRBs with the highest redshifts, i.e. GRB 080913 (Greiner et al. 2009), GRB 090423 (Tanvir et al. 2009; Salvaterra et al. 2009), and GRB 090429B (Cucchiara et al. 2011) are all of this type, but likely have a Type II (massive star) origin based on the multi-wavelength criteria (Zhang et al. 2009). It would be very interesting to investigate whether this is also due to the tip-of-iceberg effect.

In order to check such a possibility, we define a third parameter

$$f_{\rm eff,z} \equiv \frac{F'_{p,z}}{F_B}. \tag{2.4}$$

Here $F'_{p,z}$ is the 1-second peak flux of a pseudo GRB, which is generated by "moving" the original GRB to progressively higher redshifts until the rest-frame duration $T_{90}/(1+z)$ becomes shorter than 2 s. A GRB, when moved to a higher redshift, would usually have a shorter rest frame duration, although the observed duration may not shrink due to time dilation (Kocevski & Petrosian 2013). In principle, it would always reach the "rest-frame-short" phase before completely disappearing beneath the background. It would be interesting to investigate the critical redshift z_c above which a burst appears as rest-frame-short.

Technically, moving a GRB with known redshift to higher redshifts is not straightforward. One needs to reduce the time-resolved spectra of the GRB, derive the correct spectral parameters, and perform a proper k-correction to the spectrum in order to obtain the BAT-band light curve of the pseudo GRB.

To carry out such an exercise, for each GRB with redshift measurement, we first apply *Xspec* to conduct a time-dependent spectral analysis to the raw data. We dissect the lightcurve into multiple time bins, with the bin size self-adjusted to allow a signal-to-noise ratio S/N$>$ 5, so that the spectral parameters can be constrained. A typical GRB spectrum, if the observational band is wide enough, can be described as the Band function (Band et al. 1993; Abdo et al. 2009; Zhang et al. 2011). In order to perform a proper k correction, ideally one should know the Band spectral parameters α, β and E_p. However, since the BAT band is narrow, for most GRBs the spectra can be only fit by a cutoff power law or a single power law (Sakamoto et al. 2008, 2011). We therefore apply the following procedure to estimate the Band spectral parameters: 1. If a burst was also detected by *Fermi* GBM or *Konus* Wind, we adopt the spectral parameters measured by those instruments. 2. For those bursts that were not detected by other instruments but can be fit with a cutoff power law, we adopt the derived α and E_p parameters, and assume a typical value $\beta = -2.3$. 3. For those GRBs that could only be fit with a single power law, we have to a

derive E_p using an empirical correlation between the BAT-band photon index $\Gamma^{\rm BAT}$ and E_p, as derived previously for Swift GRBs (Sakamoto et al. 2009; Zhang et al. 2007a,b; Virgili et al. 2012). The typical parameters $\alpha = -1$, $\beta = -2.3$ are adopted to perform the simulations.

We note that moving a GRB to a higher z is effectively observing the rest-frame spectra in a higher energy band given the same observed BAT band. The spectral parameters β and E_p are therefore essential. These parameters are unfortunately usually not available for *Swift* GRBs. So our pseudo GRBs should be considered only as simulated GRBs rather than the original GRBs being moved to higher redshifts. In any case, such a simulation can serve the purpose of investigating the tip-of-iceberg selection effect. A similar simulation was carried out by Kocevski & Petrosian (2011).

Given the spectral parameters α, β and E_p of a particular GRB with known redshift z, we use the following procedure to simulate the pseudo GRB. First, we calculate the time-dependent bolometric burst luminosity using

$$L(t) = 4\pi D_L^2(z) F(t) k, \tag{2.5}$$

where $F(t)$ is the BAT-band, time-dependent flux, $D_L(z)$ is the luminosity distance to the source at the redshift z, and the k-correction factor corrects the BAT-band ($15 - 150$ keV) flux to a wide band in the burst rest frame ($1 - 10^4$ keV in this analysis), i.e.

$$k = \frac{\int_{1/1+z}^{10^4/1+z} EN(E)dE}{\int_{15}^{150} EN(E)dE}. \tag{2.6}$$

Here $N(E)$ is the time-dependent Band photon spectrum. To calculate $D_L(z)$, the concordance cosmology parameters ($H_0 = 71$ km s^{-1} Mpc^{-1}, $\Omega_M = 0.30$, and $\Omega_\Lambda = 0.70$) are adopted.

Next, we apply the spectral model to calculate the BAT-band flux for a pseudo GRB at redshift z'. We keep the bolometric luminosity as a constant, and derive the

BAT band flux using

$$F'(t') = \frac{L(t)}{4\pi D_L^2(z')k'}, \tag{2.7}$$

where

$$t' = \frac{1+z'}{1+z}t, \tag{2.8}$$

$D_L(z')$ is the luminosity distance to the source at redshift z', and

$$k' = \frac{\int_{1/1+z'}^{10^4/1+z'} E'N(E')dE'}{\int_{15}^{150} E'N(E')dE'}. \tag{2.9}$$

Here $N(E')$ is the observed photon number spectrum of the pseudo GRB. The spectrum is still a Band function with the same α and β values. The only difference is that the peak energy is now shifted to $E'_p = E_p(1+z)/(1+z')$. We then add the background F_B and its fluctuation based on simulation, and re-calculate T_{90} of the pseudo GRB for each z' following the same procedure to derive $f_{\rm eff}$. We then calculate the rest-frame duration using $T_{90}/(1+z)$.

By progressingly increasing z', we identify a critical redshift z_c beyond which $T_{90}/(1+z) < 2$ s is satisfied. The peak flux of the pseudo GRB at z_c is used to define $f_{\rm eff,z}$. We continue to increase the redshift, until the entire GRB disappears below the background. We record this redshift as $z_{\rm max}$. The redshift range $(z_c, z_{\rm max})$ is then where a rest-frame short GRB is observed.

The parameter $f_{\rm eff,z}$ depends on several parameters, such as $F(t)$ (which further depends on spectral parameters α, E_p, β or $\Gamma^{\rm BAT}$), and F_B. We have introduced the error of each measurable, and properly derive the error of $f_{\rm eff,z}$ through error propagation.

As an example, we take the "naked-eye" GRB 080319B (Racusin et al. 2008) as the original burst and perform the simulation. The results are shown in Figure 14. The time-integrated γ-ray spectrum is well fit using a Band function, with $E_p = 675 \pm 22$

keV. The time-resolved of spectra are well obtained, with E_p evolving from $\sim$740 keV to $\sim$540 keV. The rest-frame isotropic energy release is $E_{\rm iso} = (1.14 \pm 0.09) \times 10^{54}$ erg in the source frame $1 - 10^4$ keV band (Racusin et al. 2008, Amati et al. 2008).

We apply the above method to simulate pseudo GRBs with increasing redshifts. The lightcurves of the pseudo GRBs are presented in Figure 14a. Different colors denote different redshifts. From top to bottom, the redshifts are: $z = 0.937$ (original), 1, 2.3, 2.8, 3.6, 4.5, 5.1, and the critical redshift is $z_c = 5.53$. As shown in Figure 14a, the peak flux of the pseudo GRBs become progressively lower as z increases, and the observed durations initially become longer (due to time dilation) but later shrink (due to tip-of-iceberg effect). The rest-frame duration $T_{90}/(1+z)$ is found to decrease with redshift, similar to track with a smooth broken power-law (Figure 14b). At $z = z_c = 5.53$, $T_{90}/(1+z)$ becomes shorter than 2 s. We derive $f_{\rm eff,z} = 1.41$. The burst is no longer detectable at $z = z_{\rm max} = 5.92$.

We carry out the same exercise for all the *Swift* GRBs with known redshifts. The $T_{90}/(1+z) - f_{\rm eff,z}$ diagram is presented in Figure 11c. We can see that $f_{\rm eff.z}$ are all below $\sim$1.7. It is interesting to note that the three highest-z GRBs (080913, 090423 and 090429B) and other rest-frame-short GRBs all have f values within this range. This suggests that they are simply the tip-of-iceberg of long GRBs. This conclusion is consistent with their Type II origin as derived from multi-wavelength arguments (Zhang et al. 2009). In Figure 15, we plot the histograms of z_c and $z_{\rm max}$ of all the GRBs in our analysis, and compare them with the z distribution of the detected rest-frame short GRBs. It is found that they are generally consistent with each other. The discrepancy in the high-z end (the distribution does not fully include the highest z GRB) may be due to the uncertainty of the high-energy spectra used in our simulations.

If the rest-frame short GRBs are the tip-of-iceberg of long GRBs, then the extended emission episodes ("icebergs" themselves) may show up in the softer X-ray

band. To test this possibility, in Figure 16 we simulate the expected XRT band lightcurve of a pseudo naked-eye GRB 080319B at $z = z_c = 5.53$ (black). The same k-correction method has been applied. This is compared against the XRT-band lightcurves of the three highest-z GRBs (green for GRB 080913, blue for GRB 090423, and red for GRB 090429B), as well as the original XRT-band data of GRB 080319B (gray). It is seen that the XRT lightcurve of the pseudo GRB has an extended flaring episode extending to ~ 200 s followed by a steep decay, which is similar to the case of GRB 090423.

Conclusions and discussion

In this paper, we propose to add "amplitude" as the third dimension as a complementary criterion to study GRB classification using the prompt emission data. We introduced three parameters, f (Eq.(2.1)), $f_{\rm eff}$ (Eq.(2.2)), and $f_{\rm eff,z}$ (Eq.(2.4)), to describe the amplitude of the original GRB and some simulated pseudo GRBs. We find the following interesting results:

- The f parameters for both long and short GRBs are distributed between 1 and about 10 as a rough power law. The paucity of low-f short GRBs may be understood as a trigger selection effect.

- The f parameter of many short GRBs is larger than the $f_{\rm eff}$ parameter of long GRBs. This suggests that most short GRBs are likely intrinsically short, and *not* simply the tip-of-iceberg of long GRBs.

- There is a confusion regime as f is small (e.g. < 1.5) for short GRBs, since intrinsically long GRBs may show up as disguised short GRBs due to the tip-of-iceberg effect. GRB 090426 is such an example. Through simulations, we derive the chance probability of disguised short GRBs as a function of f for short GRBs below a certain f value (Eq.[2.3]). The contamination becomes

significant below $f \sim 1.5$, and can reach as large as $\sim 78\%$ at $f \sim 1$. This raises caution to judge the duration category of a short GRB with $f < 1.5$.

- When long GRBs are moved to high redshifts, they are likely observed as rest-frame short GRBs due to the "tip-of-iceberg" effect. These rest-frame short GRBs are supposed to have a low amplitude $f < 1.7$. The observed three highest-z GRBs and other rest-frame short GRBs all have such a low amplitude. So they are consistent with being tip-of-iceberg of long GRBs.

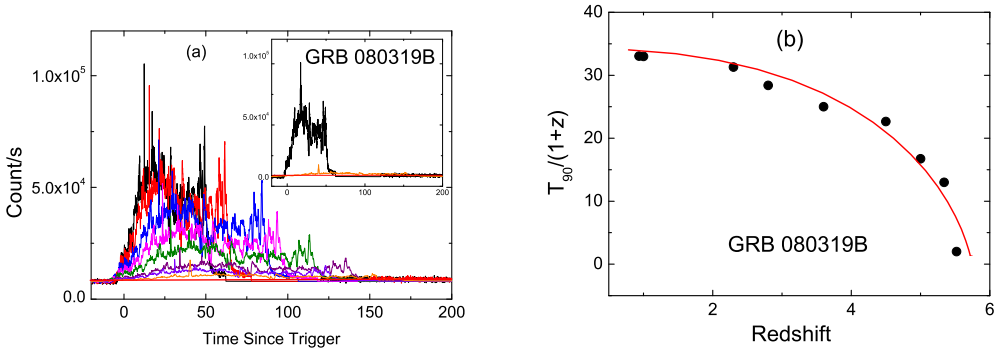

Figure 14 . (a) The simulated BAT-band pseudo GRB lightcurves by moving GRB 080319B to progressively high redshifts. From top to bottom, $z = 0.937$, 1, 2.3, 2.8, 3.6, 4.5, 5.1, 5.53. (b) The measured rest-frame duration $T_{90}/(1+z)$ of the pseudo GRBs in our simulation. The red solid line shows a smooth broken power-law fit.

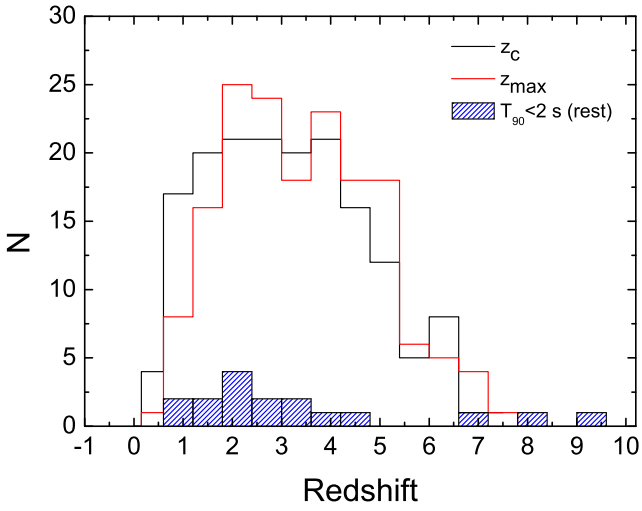

Figure 15 . The distributions of z_c and $z_{\rm max}$ for the simulated pseudo GRBs as compared with the redshift distribution of the observed rest-frame short GRBs.

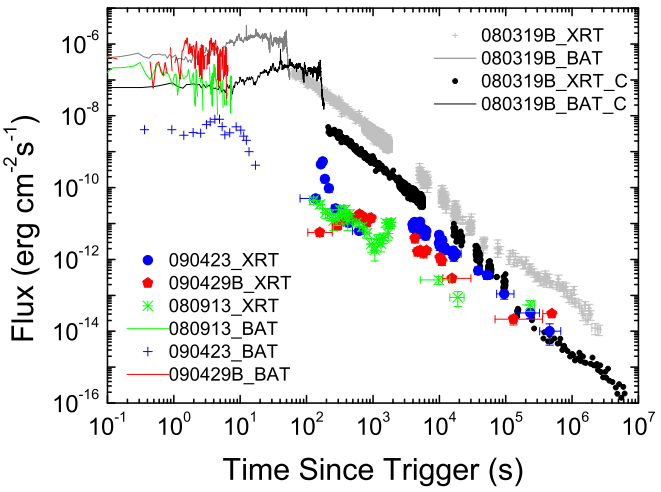

Figure 16 . The simulated XRT-band lightcurve of the pseudo GRB by moving GRB 080319B to $z = z_c = 5.53$ (black), as compared with the original XRT-band lightcurves of GRB 080319B (gray), GRB 080913 (green), GRB 090423 (blue), and GRB 090429B (red).

CHAPTER 3

A TEST OF THE MILLISECOND MAGNETAR CENTRAL ENGINE MODEL OF GRBS WITH SWIFT DATA

This chapter is part of the following published paper :

Hou-Jun Lü., Bing Zhang., 2014, The Astrophysics Journal 785,74

The central engine of gamma-ray bursts (GRBs) remains an open question in GRB physics (Zhang 2011). Observations of GRB prompt emission and early afterglow pose the following constraints on a successful central engine model: (1) The central engine must be able to power an outflow with an extremely high energy and luminosity (e.g. Zhang & Mészáros, 2004; Meszaros 2006); (2) The ejecta must have a low baryon loading, with energy per baryon exceeding 100 (e.g. Lithwick & Sari, 2001; Liang et al. 2010); (3) The central engine should be intermittent in nature to account for the observed light curves with rapid variability (Fishman & Meagan 1995); (4) The engine should last for an extended period of time to power delayed erratic X-ray flares (Burrows et al. 2005; Zhang et al. 2006) or long-lasting X-ray emission followed by a sudden drop (i.e. "internal plateau", Troja et al. 2007; Liang et al. 2007; Lyons et al. 2010); (5) Finally, Fermi observations require that the central engine should be strongly magnetized to launch a magnetically dominated outflow at least for some GRBs (Zhang & Pe'er 2009).

Two types of GRB central engine models have been discussed in the literature (e.g. Kumar & Zhang 2014 for a review). The leading type of models invokes a hyper-accreting stellar-mass black hole (e.g. Popham et al. 1999; Narayan et al. 2001; Lei et al. 2013), from which a relativistic jet is launched via neutrino-anti-neutrino annihilation (Ruffert et al. 1997; Popham et al. 1999; Chen & Beloborodov 2007; Lei et al. 2009), Blandford-Znajek mechanism (Blandford & Znajek 1997; Lee et al. 2000; Li 2000), or episodic magnetic bubble ejection from the disk (Yuan & Zhang 2012).

The second type of models invokes a rapidly spinning, strongly magnetized neutron star dubbed a "millisecond magnetar" (Usov 1992; Thompson 1994; Dai & Lu 1998a; Wheeler et al. 2000; Zhang & Mészáros 2001; Metzger et al. 2008, 2011; Bucciantini et al. 2012). Within this scenario, the energy reservoir is the total rotation energy of the millisecond magnetar, which reads

$$E_{\rm rot} = \frac{1}{2} I \Omega_0^2 \simeq 2 \times 10^{52} \ {\rm erg} \ M_{1.4} R_6^2 P_{0,-3}^{-2}, \tag{3.1}$$

where I is the moment of inertia, $\Omega_0 = 2\pi/P_0$ is the initial angular frequency of the neutron star, $M_{1.4} = M/1.4 M_\odot$, and the convention $Q = 10^x Q_x$ is adopted in cgs units for all other parameters throughout the paper.

Assuming that the magnetar with initial spin period P_0 is being spun down by a magnetic dipole with surface polar cap magnetic field B_p, the spindown luminosity would evolve with time as (Zhang & Mészáros 2001)

$$\begin{aligned} L(t) &= L_0 \frac{1}{(1+t/\tau)^2} \\ &\simeq \begin{cases} L_0, & t \ll \tau, \\ L_0 (t/\tau)^{-2}, & t \gg \tau. \end{cases} \end{aligned} \tag{3.2}$$

where

$$L_0 = 1.0 \times 10^{49} \ {\rm erg \ s^{-1}} (B_{p,15}^2 P_{0,-3}^{-4} R_6^6) \tag{3.3}$$

is the characteristic spindown luminosity, and

$$\tau = 2.05 \times 10^3 \ {\rm s} \ (I_{45} B_{p,15}^{-2} P_{0,-3}^2 R_6^{-6}) \tag{3.4}$$

is the characteristic spindown time scale.

The spin-down behavior of the magnetar can leave characteristic imprints in the observed GRB emission. Dai & Lu (1998a) first proposed an energy injection model

of millisecond pulsars to interpret a rebrightening feature of the first optical afterglow detected in GRB 970228. The required B_p is $\sim 10^{13}$ G, not quite a magnetar strength. The prompt GRB emission has to be attributed to additional physical processes, e.g. magnetic dissipation in a differentially rotating neutron star (Kluzniak & Ruderman 1998) or strange quark star (Dai & Lu 1998b). Zhang & Mészáros (2001) studied energy injection from a central engine with a general luminosity law $L(t) = L_0(t/t_0)^{-q}$ (the magnetar injection corresponds to $q = 0$ for $t < \tau$ and $q = 2$ for $t > \tau$), and pointed out that besides the rebrightening feature discussed by Dai & Lu (1998a,b), for more typical magnetar parameters, one can have a shallow decay phase followed by a normal decay phase in the early afterglow of a GRB. Such a shallow decay phase (or plateau) was later commonly observed in Swift early XRT light curves (Zhang et al. 2006; Nousek et al. 2006; O'Brien et al. 2006; Liang et al. 2007). It can be readily interpreted as energy injection from a millisecond magnetar central engine (Zhang et al. 2006). An alternative energy injection model invokes a short-duration central engine, which ejects materials with a stratified Lorentz factor (Γ) profile. Energy is gradually added to the blastwave as the blastwave is gradually decelerated to progressively lower Γ (Rees & Mészáros 1998; Sari & Mészáros 2000; Uhm et al. 2012). Both models can interpret the shallow decay phase of most X-ray light curves.

A tie-breaker GRB was discovered in early 2007. GRB 070110 (Troja et al. 2007) showed an extended plateau with a near flat light curve extending to over 10^4 seconds before rapidly falling off with a decay index $\alpha \sim 9$ (throughout the paper the convention $F_\nu \propto t^{-\alpha}\nu^{-\beta}$ is adopted). Such a rapid decay cannot be accommodated in any external shock model, so that the entire X-ray plateau emission has to be attributed to internal dissipation of a central engine wind. Such an "internal plateau" was later discovered in several more GRBs (Liang et al. 2007; Lyons et al. 2010). The near steady X-ray emission observed in GRB 070110 may not be easy to interpret within a black hole central engine model, but is a natural prediction of the magnetar cen-

tral engine model (Eq.(3.2) when $t \ll \tau$). The rapid t^{-9} decay near the end is not predicted in the magnetic dipole radiation model. Troja et al. (2007) interpreted it as being due to collapse of the magnetar to a black hole after loosing centrifugal support[1]. Interestingly, internal plateaus are also discovered in a good fraction of short GRBs (Rowlinson et al. 2010, 2013). Modeling various afterglow features for both long and short GRBs within the framework of the millisecond magnetar (or pulsar with weaker magnetic field) central engine model has gained growing attention (Dai et al. 2006; Gao & Fan 2006; Fan & Xu 2006; Metzger et al. 2008, 2011; Dall'Osso et al. 2011; Fan et al. 2011; Bucciantini et al. 2012; Bernardini et al. 2013; Gompertz et al. 2013, 2014). Numerical simulations of binary neutron star mergers indeed show that a stable magnetar can survive if the initial masses of the two neutron stars are small enough, which would power a short gamma-ray burst (Giacomazzo & Perna. 2013).

Even though evidence of a magnetar central engine is mounting, it remains unclear whether the rich GRB data accumulated over the years with the GRB mission Swift indeed statistically requires the existence of (presumably) two types of central engines. If indeed magnetars are operating in some GRBs while hyper-accreting black holes are operating in others, do the data show statistically significant differences between the two samples? Do those GRBs that seem to have a magnetar signature have physical parameters that are consistent with the predictions of the magnetar central engine model?

This chapter is to address these interesting questions through a systematic analysis of the Swift X–Ray Telescope (XRT) data. The XRT data reduction details and criteria for sample selection are presented in first. Then, physical parameters of the

[1]Such an interpretation recently gains indirect support. Zhang (2014) suggested that such an implosion in the GRB early afterglow phase should be accompanied by a fast radio burst (FRB) (see also Falcke & Rezzolla 2013 for a proposal of more general supra-massive neutron star implosions as the sources of FRBs), and tentative detections of these FRBs following two GRBs may have been detected (Bannister et al. 2012), roughly around the time suggested by Zhang (2014).

GRBs and the hypothetical magnetars are derived for all the samples. A statistical comparison of the physical properties between the magnetar samples and the non-magnetar sample are presented, and conclusions are drawn at last section with some discussion.

Data reduction and sample selection criteria

The XRT data are downloaded from the Swift data archive[2]. We developed a script to automatically download and maintain all the XRT data on the local UNLV machine. The HEAsoft packages *version 6.10*, including Xspec, Xselect, Ximage, and the Swift data analysis tools, are used for the data reduction. An IDL code was developed by the former group member B.-B. Zhang to automatically process the XRT data for a given burst in any user-specified time interval (see Zhang et al. 2007c for details). We adopt this code with slight modifications to solve the problem designed for this paper. The same IDL code was used in several previous papers (Zhang et al. 2007c; Liang et al. 2007, 2008, 2009) of our group. More details about the data reduction procedures can be found in Zhang et al. (2007c) and Evans et al. (2009).

Our entire sample includes more than 750 GRBs observed between 2005 January and 2013 August, whose XRT data are all processed with our data reduction tool. Since the magnetar signature typically invokes a shallow decay phase (or plateau) followed by a steeper decay segment (a normal decay for canonical light curves, or a very steep decay for internal plateaus), our attention is on those GRBs that show such a transition in the X-ray light curves. We first identify such bursts by inspecting their light curves. In order to grade their magnetar candidacy, we next perform a temporal fit to the plateau behavior within a time interval (t_1, t_2), where t_1 is the beginning of the plateau, while t_2 is the end of the segment after the plateau break

[2]http://www.swift.ac.uk/archive/obs.php?burst=1

(either last observed data point if there is no further break in the lightcurve, or the break time if a second break appears). Since we are mostly interested in the behavior around the break time t_b, the exact positions of t_1 and t_2 do not matter much, so we pick them through visual inspection of the light curves. We then fit the light curves with a smooth broken power law

$$F = F_0 \left[\left(\frac{t}{t_b} \right)^{\omega\alpha_1} + \left(\frac{t}{t_b} \right)^{\omega\alpha_2} \right]^{-1/\omega}, \tag{3.5}$$

where t_b is the break time, $F_b = F_0 \cdot 2^{-1/\omega}$ is the flux at the break time t_b, α_1 and α_2 are decay indices before and after the break, respectively, and ω describes the sharpness of the break. The larger the ω parameter, the sharper the break.

An IDL routine named "mpfitfun.pro" is employed for our fitting (Moré 1977; Markwardt 2009). This routine performs a Levenberg-Marquardt least-square fit to the data for a given model to optimize the model parameters. After processing all the data, we grade all long GRBs in our sample into four groups ("Gold", "Silver", "Aluminum", and "non-magnetar") according to their likelihood of being powered by a magnetar central engine.

- Gold: This sample is defined by those bursts that display an "internal plateau". These plateaus are followed by a decay slope steeper than 3, which is essentially impossible to interpret within the external shock models (Gao et al. 2013b)[3]. It demands a long-lasting central engine, and a near steady flux is consistent with emission from a spinning down magnetar. The rapid decay at the end of plateau may mark the implosion of the magnetar into a black hole (Troja et al. 2007; Zhang 2014). There are altogether only 9 robust cases identified in this Gold sample, 3 of which have redshift measurements. The light curves of these

[3]The steepest decay slope in an external shock model is $2+\beta$ (Kumar & Panaitescu 2000), which is typically smaller than 3, and is defined by the high-latitude "curvature effect" emission from a conical outflow, even if the emission abruptly ceases.

9 GRBs together with the broken power-law fittings (red curves) are shown in Fig.17, and the fitting parameters are summarized in Table 1 and 2.

- Silver: This sample includes GRBs with a shallow decay phase followed by a normal decay phase, and the pre- and post-break temporal and spectral properties are well consistent with the external forward shock model with energy injection of a magnetar as defined in Eq.(3.2). Specifically, one requires two indepedent criteria to define this sample. First, the temporal and spectral properties of the afterglow after the break (the normal decay phase) should satisfy the "closure relation" of the external shock model (e.g. Zhang & Mészáros 2004; Gao et al. 2013b), i.e.

$$\alpha_2 = \begin{cases} \frac{3\beta}{2} = \frac{3(p-1)}{4}, & \nu_m < \nu < \nu_c \text{ (ISM)} \\ \frac{3\beta+1}{2} = \frac{3p-1}{4}, & \nu_m < \nu < \nu_c \text{(Wind)} \\ \frac{3\beta-1}{2} = \frac{3p-2}{4}, & \nu > \nu_c \text{(ISM or Wind)} \end{cases} \tag{3.6}$$

Here β is the spectral index of the normal decay segment (which is X-ray photon index minus 1), and p is the electron's spectral distribution index. Second, the pre-break slope α_1 should correspond to $q = 0$, while the post-break slope α_2 should correspond to $q = 1$ (for a constant energy fireball, the scaling law is the same as $q = 1$, Zhang & Mészáros 2001), so according to Zhang et al. (2006) and Gao et al. (2013b), one should have

$$\alpha_1 = \begin{cases} \frac{2\alpha_2-3}{3}, & \nu_m < \nu < \nu_c \text{ (ISM)} \\ \frac{2\alpha_2-1}{3}, & \nu_m < \nu < \nu_c \text{(Wind)} \\ \frac{2\alpha_2-2}{3}, & \nu > \nu_c \text{(ISM or Wind)} \end{cases} \tag{3.7}$$

In our entire sample, 69 GRBs can be grouped into this Silver sample, with 33 having measured redshifts. The light curves with fitting curves are presented online at http://grb.physics.unlv.edu/ lhj/Silver/, and the fitting results are reported in Table 1 and 2. Two examples (GRBs 060729, see also Grupe et al.

2007, and 070306) are shown in Figure 18. Fig.19 shows all the GRBs in the $\alpha_1 - \alpha_2$ plane, with three theoretically favored lines of the magnetar models (Eq.(3.7)) plotted. Those GRBs falling onto these lines (within error bars) and also satisfy the closure relations are identified as Silver sample GRBs (colored data points). In Fig.20 we present the distribution of electron spectral index p derived from the Silver sample. It has a Gaussian distribution with a center value $p_c = 2.51 \pm 0.04$. Figure 21 shows the distribution of Silver sample in the (α, β)-plane combined with the closure relations for the models (ISM and wind medium).

- Aluminum: Other GRBs with a shallow decay segment transiting to a steeper decay are included in the Aluminum sample. They either do not satisfy external shock closure relations in the post-break phase, or do not satisfy the $\alpha_1 - \alpha_2$ relations predicted in the magnetar external shock models. These are marked as grey points in Fig.3. Those GRBs that fall onto the three magnetar model lines but are still denoted as Aluminum are the ones that do not satisfy the closure relations in the post-break phase. On the other hand, since early magnetar spindown may not fully follow the simple dipole spindown law (e.g. Metzger et al. 2011), and since the observed X-ray emission may not come from the external forward shock emission (e.g. can be from external reverse shock, Dai 2004; Yu & Dai 2007, or from internal dissipation of the magnetar wind, Yu et al. 2010), these GRBs could be still powered by magnetars. We therefore still assign them as magnetar candidates, but with a lower grade. There are 135 solid cases in the sample, 67 of which have redshift measurements. The light curves with fitting curves are presented online at http://grb.physics.unlv.edu/ lhj/Aluminum/. Two examples (GRBs 070420 and 080430) are presented in Fig.18.

- Non-magnetar: All the other long GRBs we have analyzed are included in the non-magnetar sample. They either have a single power-law decay, or have erratic flares that prevent identifying a clear shallow decay phase, or present a rebrightening behavior, or the data are too poor to reach a robust conclusion. There are more than 400 GRBs in this group, 111 of which have redshift measurements. Strictly speaking, some of these GRBs may still host a magnetar central engine. We define these GRBs as "non-magnetar", simply because they do not present a clear magnetar signature. Two examples (GRBs 061007, see also Schady et al. 2007, Mundell et al. 2007, and 081028) are presented in the Fig.18.

Finally, we also independently processed the X-ray data of short GRBs that may harbor a magnetar central engine (cf. Rowlinson et al 2013). We select the short GRBs that have measured redshifts and high-quality X-ray data. The light curves with fitting curves are presented online at http://grb.physics.unlv.edu/ lhj/SGRB/.

Derivations of the physical parameters

Our purpose is to analyze and compare the physical properties of GRBs with or without a magnetar signature. In this section, we use data to derive relevant physical parameters. Redshift measurements are crucial to derive the intrinsic parameters (energy, luminosity, etc), so in the following we focus on those GRBs with z measurements only.

Energetics, luminosity, and radiation efficiency

The isotropic prompt γ-ray emission energy $E_{\gamma,\rm iso}$ is usually derived from the observed fluence S_γ in the detector's energy band, and extrapolated to the rest-frame $1-10^4$ keV using spectral parameters (the low- and high- energy spectral indices $\hat{\alpha}$, $\hat{\beta}$, and the peak energy E_p for a standard "Band-function" fit, Band et al. 1993) and

through k-correction. However, since the BAT energy band is narrow (15-150 keV), for most GRBs the spectra can be only fit by a cutoff power law or a single power law (Sakamoto et al. 2008, 2011). We therefore apply the following procedure to estimate the Band spectral parameters: (1) If a burst was also detected by *Fermi* GBM or *Konus* Wind, we adopt the spectral parameters measured by those instruments. (2) For those bursts that are not detected by other instruments but can be fit with a cutoff power law model, we adopt the derived $\hat{\alpha}$ and E_p parameters[4], and assume a typical value of $\hat{\beta} = -2.3$. (3) For those GRBs that can be only fit with a single power law, we have to a derive E_p using an empirical correlation between the BAT-band photon index $\Gamma^{\rm BAT}$ and E_p (e.g. Sakamoto et al. 2009; Zhang et al. 2007b; Virgili et al. 2012; Lü et al. 2012). The typical parameters $\hat{\alpha} = -1$, $\hat{\beta} = -2.3$ are adopted to perform the simulations. We can then calculate the $E_{\gamma,\rm iso}$ according to

$$\begin{aligned} E_{\gamma,\rm iso} &= 4\pi k D_L^2 S_\gamma (1+z)^{-1} \\ &= 1.3\times10^{51}\ {\rm erg}\ k D_{28}^2 (1+z)^{-1} S_{\gamma,-6} \end{aligned} \tag{3.8}$$

where z is the redshift, $D = 10^{28}$ cm D_{28} is the luminosity distance, and k is the k-correction factor from the observed band to $1 - 10^4$ keV in the burst rest frame (e.g. Bloom et al. 2001).

Another important parameter is the isotropic kinetic energy $E_{\rm K,iso}$ measured from the afterglow flux. This value is increasing during the shallow decay phase, but becomes constant during the normal decay phase (Zhang et al. 2007a). We follow the method discussed in Zhang et al. (2007a) to calculate $E_{\rm K,iso}$ during the normal decay phase using the X-ray data. Noticing that fast-cooling is disfavored at this late epoch, we derive several relevant cases. For $\nu > \max(\nu_m, \nu_c)$, the afterglow flux

[4]We note that usually the low-energy photon index $\hat{\alpha}$ and E_p are slightly different for the cut-off power law and Band-function models (e.g. Sakamoto et al. 2008, 2011), but the derived $E_{\gamma,\rm iso}$ only shows a slight difference, which is ignored in our analysis.

expression does not depend on the medium density, so the following expression (Zhang et al. 2007a) applies to both ISM and wind models[5]

$$\begin{aligned} E_{\rm K,iso,52} &= \left[\frac{\nu F_\nu(\nu=10^{18}\ {\rm Hz})}{5.2\times10^{-14}\ {\rm ergs\ s^{-1}\ cm^{-2}}}\right]^{4/(p+2)} \\ &\times D_{28}^{8/(p+2)}(1+z)^{-1}t_d^{(3p-2)/(p+2)} \\ &\times (1+Y)^{4/(p+2)}f_p^{-4/(p+2)}\epsilon_{B,-2}^{(2-p)/(p+2)} \\ &\times \epsilon_{e,-1}^{4(1-p)/(p+2)}{\nu_{18}}^{2(p-2)/(p+2)}. \end{aligned} \tag{3.9}$$

For the $\nu_m < \nu < \nu_c$ ISM model, one has (Zhang et al. 2007a)

$$\begin{aligned} E_{\rm K,iso,52} &= \left[\frac{\nu F_\nu(\nu=10^{18}\ {\rm Hz})}{6.5\times10^{-13}\ {\rm ergs\ s^{-1}\ cm^{-2}}}\right]^{4/(p+3)} \\ &\times D_{28}^{8/(p+3)}(1+z)^{-1}t_d^{3(p-1)/(p+3)} \\ &\times f_p^{-4/(p+3)}\epsilon_{B,-2}^{-(p+1)/(p+3)}\epsilon_{e,-1}^{4(1-p)/(p+3)} \\ &\times n^{-2/(p+3)}{\nu_{18}}^{2(p-3)/(p+3)}. \end{aligned} \tag{3.10}$$

For the $\nu_m < \nu < \nu_c$ wind model, one has (Gao et al. 2013b)

$$\nu_m = 5.5\times10^{11}Hz(\frac{p-2}{p-1})^2(1+z)^{1/2}\epsilon_{B,-2}^{1/2}\epsilon_{e,-1}^{2}E_{\rm K,iso,52}^{1/2}t_d^{-3/2}, \tag{3.11}$$

$$\nu_c = 4.7\times10^{18}Hz(1+z)^{-3/2}A_{*,-1}^{-2}\epsilon_{B,-2}^{-3/2}E_{\rm K,iso,52}^{1/2}t_d^{1/2}, \tag{3.12}$$

[5]The coefficients may be slightly different for the two ambient medium models. Since in this regime one cannot differentiate the two circumburst medium models, we universally adopt this equation derived from the ISM model, keeping in mind that there might be a factor of a few correction if the medium is wind-like.

$$F_{\nu,max} = 5.7 \times 10^2 \mu Jy (1+z)^{3/2} A_{*,-1} \epsilon_{B,-2}^{1/2} D_{28}^{-2} E_{\rm K,iso,52}^{1/2} t_d^{-1/2}, \tag{3.13}$$

so that

$$\begin{aligned} \nu F_\nu(\nu = 10^{18} Hz) &= \nu F_{\nu,max} (\frac{\nu}{\nu_m})^{-(p-1)/2} \\ &= F_{\nu,max} \nu^{(3-p)/2} \nu_m^{(p-1)/2} \\ &= 7.4 \times 10^{-14} \text{ erg cm}^{-2} \text{ s}^{-1} \\ &\times D_{28}^{-2} (1+z)^{(p+5)/4} A_{*,-1} f_p \epsilon_{B,-2}^{(p+1)/4} \epsilon_{e,-1}^{p-1} \\ &\times E_{\rm K,iso,52}^{(p+1)/4} t_d^{(1-3p)/4} \nu_{18}^{(3-p)/2}, \end{aligned} \tag{3.14}$$

and

$$\begin{aligned} E_{\rm K,iso,52} &= \left[\frac{\nu F_\nu(\nu = 10^{18} \text{ Hz})}{7.4 \times 10^{-14} \text{ ergs s}^{-1} \text{ cm}^{-2}} \right]^{4/(p+1)} \\ &\times D_{28}^{8/(p+1)} (1+z)^{-(p+5)/(p+1)} t_d^{(3p-1)/(p+1)} \\ &\times f_p^{-4/(p+1)} \epsilon_{B,-2}^{-1} \epsilon_{e,-1}^{4(1-p)/(p+1)} \\ &\times A_{*,-1}^{-4/(p+1)} {\nu_{18}}^{2(p-3)/(p+1)}. \end{aligned} \tag{3.15}$$

Here $\nu f_\nu(\nu = 10^{18}\text{Hz})$ is the energy flux at 10^{18} Hz (in units of ergs s^{-1} cm^{-2}), n is the density of the constant ambient medium, A_* is the stellar wind parameter, t_d is the time in the observer frame in days, and Y is the Compton parameter. The electron spectral index p and the spectral index β are connected through

$$p = \begin{cases} 2\beta + 1, & \nu_m < \nu < \nu_c \\ 2\beta, & \nu > \nu_c, \end{cases} \tag{3.16}$$

and f_p is a function of the power law distribution index p (Zhang et al. 2007a)

$$f_p \sim 6.73 \left(\frac{p-2}{p-1}\right)^{p-1} (3.3\times10^{-6})^{(p-2.3)/2} \tag{3.17}$$

In our calculations, the microphysics parameters of the shock are assigned to standard values dervied from observations (e.g. Panaitescu & Kumar 2002; Yost et al. 2003): ϵ_e=0.1 and $\epsilon_B = 0.01$. The Compton parameter is assigned to a typical value $Y = 1$.

After deriving the break time t_b through light curve fitting, we derive the break time luminosity as

$$L_b = 4\pi D^2 F_b, \tag{3.18}$$

where F_b is the X-ray flux at t_b. Since the XRT band is narrow, no k-correction is possible to calculate L_b.

A jet break was detected in some GRBs in our sample. For these GRBs, we correct all the isotropic values to the beaming-corrected values by multiplying the values by the beaming correction factor (Frail et al. 2001)

$$f_b = 1 - \cos\theta_j \simeq (1/2)\theta_j^2, \tag{3.19}$$

i.e. $E_\gamma = E_{\gamma,\rm iso} f_b$, and $E_{\rm K} = E_{\rm K,iso} f_b$. The jet angle information was searched from the literature (e.g. Liang et al. 2008; Racusin et al. 2009; Lu et al. 2012; Nemmen et al. 2012), which is collected in Table 3 and 3.

The GRB radiation efficiency is defined as (Lloyd-Ronning & Zhang 2004)

$$\eta_\gamma = \frac{E_{\gamma,\rm iso}}{E_{\gamma,\rm iso} + E_{\rm K,iso}} = \frac{E_\gamma}{E_\gamma + E_{\rm K}}. \tag{3.20}$$

Since $E_{\rm K,iso}$ (and $E_{\rm K}$) are increasing functions of time during the shallow decay phase, η_γ is different when $E_{\rm K,iso}$ ($E_{\rm K}$) at different epochs are adopted. Following Zhang et al. (2007a), we take a typical blastwave deceleration t_{dec} and the end of the shallow

decay phase t_b to calculate the radiative efficiencies. Within the framework of the magnetar central engine model, the two efficiencies carry different physical meanings: $\eta_\gamma(t_{dec})$ denotes the efficiency of dissipating the magnetar wind energy during the prompt emission phase, while $\eta_\gamma(t_b)$ denotes the total efficiency of converting the spindown energy of a magnetar to γ-ray radiation.

Magnetar parameters

For a magnetar undergoing dipolar spindown, two important magnetar parameters, i.e. the initial spin period P_0 and the surface polar cap magnetic field B_p, can be solved by the characteristic luminosity L_0 (Eq.(4.6)) and the spindown time scale τ (Eq.(4.5)).

The spindown time scale can be generally identified as the observed break time, i.e.

$$\tau = t_b/(1+z). \tag{3.21}$$

One caution is that τ can be shorter than $t_b/(1+z)$ if the magnetar is supra-massive, and collapses to a black hole before it is significantly spun down. On the other hand, the angular velocity of the magnetar does not change significantly until reaching the characteristic spindown time scale, so that the collapse of the supra-massive magnetar, if indeed happens, would likely happen at or after τ. In our analysis, we will adopt Eq.(3.21) throughout.

The characteristic spindown luminosity should generally include two terms:

$$L_0 = L_{\rm X} + L_{\rm K} = (L_{\rm X,iso} + L_{\rm K,iso}) f_b, \tag{3.22}$$

where $L_{\rm X,iso}$ is the X-ray luminosity due to internal dissipation of the magnetar wind, which is the observed X-ray luminosity of the internal plateau (for external plateaus,

one can only derive an upper limit), and

$$L_{\rm K,iso} = E_{\rm K,iso}(1+z)/t_b \tag{3.23}$$

is the kinetic luminosity that is injected into the blastwave during the energy injection phase. It depends on the isotropic kinetic energy $E_{\rm K,iso}$ after the injection phase is over, which can be derived from afterglow modeling discussed above. For the Gold sample, the $L_{\rm X,iso}$ component dominates, while for Silver and Aluminum samples, the $L_{\rm K,iso}$ component dominates. In any case, both components should exist and contribute to the observed flux (Zhang 2014). One can also define an X-ray efficiency to define the radiative efficiency for a magnetar to convert its spindown energy to radiation, i.e.

$$\eta_{\rm X} = \frac{L_{\rm X}}{L_{\rm X}+L_{\rm K}} = \frac{L_{\rm X,iso}}{L_{\rm X,iso}+L_{\rm K,iso}}. \tag{3.24}$$

In our analysis, we try to calculate both $L_{\rm X,iso}$ and $L_{\rm K,iso}$ from the data. For the Gold sample GRBs that show internal plateaus, $L_{\rm X,iso}$ can be readily measured. For the cases where the internal plateau lands on an external shock component (e.g. Troja et al. 2007), $L_{\rm K,iso}$ can be also derived by modeling the late X-ray afterglow in the normal decay phase. For the Gold sample cases where no late external shock component is available, one can only set up an upper limit on $L_{\rm K,iso}$. For Silver and Aluminum samples, the internal plateau component is not detectable. Through simulations, we find that the external shock component would not be significantly modified if the internal plateau flux is below 50% of the observed external shock flux. Therefore for all the Silver and Aluminum sample GRBs, we place an upper limit of $L_{\rm X,iso}$ as 50% of the observed X-ray flux.

Results

Magnetar parameters and collimation

We derive magnetar parameters (P_0 and B_p) of the Gold, Silver and Aluminum samples using Eqs.(4.6), (4.5), and (3.22)[6]. First, we assume that the magnetar wind is isotropic, so that $f_b = 1$. The derived P_0, B_p are presented in Table 3, 3 and Fig.22a. Most "magnetars" have B_p below 10^{15} G, some even have B_p below 10^{13} G, which are not considered as magnetars. More problematically, most derived P_0's are much shorter than 1 ms. This directly conflicts with the break-up limit of a neutron star, which is about 0.96 ms (Lattimer & Prakash 2004). This suggests that the isotropic assumption for these long GRB magnetar winds is not correct. We then introduce the beaming factor f_b for each GRB. If θ_j is measured, we simply adopt the value. Otherwise, we choose $\theta_j = 5^{\rm o}$, a typical jet opening angle for bright long GRBs (Frail et al. 2001; Liang et al. 2008). Very interestingly, after such a correction, all the data points of Gold and Silver sample GRBs fall into the expected region in the $P_0 - B_p$ plot (Fig.22b). Also the additional conditions imposed by the causality argument (i.e. that the speed of sound on the neutron star cannot exceed the speed of light, Lattimer et al. 1990, and Eqs.(9) and (10) of Rowlinson et al. (2010)) are satisfied for all GRBs in all three (Gold, Silver and Aluminum) magnetar samples, if one assumes $M = 1.4 M_\odot$. All these suggest that the long GRB magnetar winds are likely collimated. Some Aluminum sample GRBs are still to the left of the allowed region (with P_0 shorter than the break-up limit). This may suggest that those Aluminum sample bursts are not powered by magnetars, or are powered by magnetars with even narrower jets.

Very interestingly, the magnetar properties of short GRBs derived under the

[6]Strictly speaking, these magnetar parameters are the ones after prompt emission is over, since only $L_{\rm X}$ and $L_{\rm K}$ are used to derive them. The GRB prompt emission presumably also consumed spin energy and magnetic energy of the magnetar, so the true initial spin period can be somewhat smaller than P_0, and the true initial (effective) dipole magnetic field at the pole can be somewhat larger than B_p).

isotropic assumption actually lie reasonably in the allowed region (Fig.22a, blue dots). After jet correction for long GRB magnetars (but keep short GRB magnetar wind isotropic), the derived magnetar parameters are well mixed in the same region. This suggests that the isotropic assumption for short GRBs is reasonably good. This is understandable within the framework of the progenitor models of GRBs. Short GRBs are believed to be powered by mergers of NS-NS or NS-BH systems (Paczynski 1986; Eichler et al. 1989; Paczynski 1991; Narayan et al. 1992). During the merger process, only a small amount of materials are launched (Freiburghaus et al. 1999; Rezzolla et al. 2010; Hotokezaka et al. 2013). A millisecond magnetar is expected to launch a near isotropic wind. This wind, instead of being collimated by the ejecta (e.g. Bucciantini et al. 2012), would simply push the ejecta behind and accelerate the ejecta and make a bright electromagnetic signal in the equatoral directions (Fan & Xu 2006; Zhang 2013; Gao et al. 2013; Yu et al. 2013; Metzger & Piro 2013). In the jet direction, the magnetar wind emission is not enhanced by the beaming effect, so that one can infer correct magnetar parameters assuming an isotropic wind. For long GRBs, on the other hand, jets are believed to be launched from collapsing massive stars (Woosley 1993; MacFadyen & Woosley 1999). The initially near isotropic magnetar wind is expected to be soon collimated by the stellar envelope to a small solid angle (Bucciantini et al. 2008).

Statistical properties and correlations of other parameters

Figure 23a shows the correlations of $L_b - E_{\gamma,\rm iso}$ and $L_b - t_b$ for the entire sample. As shown in 23a, a higher isotropic γ-ray energy generally has a higher X-ray break luminosity. For the Gold and Silver samples, a Spearman correlation analysis gives a dependence

$$\log L_{b,49} = (1.48 \pm 0.17) \log E_{\gamma,\rm iso,52} + (2.56 \pm 0.75), \tag{3.25}$$

with a correlation coefficient $r = 0.83$, and a chance probability $p < 0.001$. Adding the Aluminum sample only slightly worsens the correlation ($\log L_{b,49} = (1.02 \pm 0.10) \log E_{\gamma,\rm iso,52} + (2.64 \pm 2.04)$, with $r = 0.72$ and $p < 0.001$). Such a correlation is expected, which may be caused by a combination of intrinsic (a more energetic magnetar gives more significant contribution to both prompt emission and afterglow) and geometric effects (a narrower jet would enhance both prompt emission and afterglow).

Figure 23b presents an anti-correlation between L_b and t_b (Dainotti et al. 2010). Our Gold + Silver sample gives

$$\log L_{b,49} = (-1.83 \pm 0.20) \log t_{b,3} + (0.2 \pm 0.18) \tag{3.26}$$

with $r = 0.84$ and $p < 0.001$. Adding the Aluminum sample only slightly worsens the correlation ($\log L_{b,49} = (-1.29 \pm 0.15) \log t_{b,3} - (0.43 \pm 0.14)$ with $r = 0.66$ and $p < 0.001$). Such an anti-correlation is consistent with the prediction of the magnetar model: Given a quasi-universal magnetar total spin energy, a higher magnetic field would power a brighter plateau with a shorter duration, or vice versa (see also Xu & Huang 2012).

In Figure 24, we compare the inferred $E_\gamma + E_{\rm K}$ with the total rotation energy $E_{\rm rot}$ (Eq.(4.4)) of the millisecond magnetar. It is found that the GRBs are generally above and not too far above the $E_{\rm rot} = E_\gamma + E_{\rm K}$ line. This is consistent with the magnetar hypothesis, namely, all the emission energy ultimately comes from the spin energy of the magnetar. Figure 24a includes all the GRBs in the Gold/Silver/Aluminum samples, with $\theta_j = 5^{\rm o}$ assumed if the jet angle is not measured. Figure 24b presents those GRBs with jet measurements only. Essentially the same conclusion is reached.

A very interesting question is whether there are noticeable differences between the magnetar and non-magnetar samples. One potential discriminator would be the total energetics of the GRBs. While the magnetar model predicts a maximum value of the

total energy (Eq.(4.4)), the black hole model is not subject to such a limit. In Figure 25 we make some comparisons. The first three panels compare the histograms of the isotropic energies ($E_{\gamma,\rm iso}$, $E_{\rm K,iso}$, and $E_{\gamma,\rm iso}+E_{\rm K,iso}$) of the magnetar and non-magnetar samples. For the magnetar sample, we in one case includes the most secure (Gold + Silver) sample only (blue hatched), and in another case includes all magnetar candidates (Gold + Silver + Aluminum) (red solid). The non-magnetar sample is marked in grey. The best Gaussian fits to the three samples are presented as blue, red, and black dotted curves, respectively. The center values of all the fits are presented in Table 3. It is found that without jet correction, the isotropic values of the magnetar and non-magnetar samples are not significantly different.

Next, we introduce beaming correction, and replot the histograms of the jet-corrected energies of the magnetar and non-magnetar samples. The results are presented in the later three panels in Figure 25. One can see a clear distinction between the robust magnetar sample (Gold + Silver) and the non-magnetar sample. For the total energy ($E_\gamma + E_{\rm K}$), while the former peaks around 50.62 erg, the latter peaks around 51.81 erg. More interestingly, all the Gold+Silver magnetar sample GRBs have a total energy smaller than the limit set by the spin energy (Eq.(4.4)), while for some non-magnetar sample GRBs, this upper limit is exceeded. The results are generally consistent with the hypothesis that two types of GRB central engines can both power GRBs.

In Figure 26a and Figure 26b, we compare $E_{\gamma,\rm iso}$ and $E_{\rm K,iso}$ for the magnetar and non-magnetar samples. The kinetic energy of the blastwave $E_{\rm K,iso}$ is evaluated at t_b for Figure 26a, and at t_{dec} for Figure 26b (similar to Zhang et al. 2007a). It is interesting to see that at t_{dec}, the magnetar central engine tends to power more efficient GRBs (due to the initial small $E_{\rm K}$ value) than the black hole central engine. It is interesting to see after the energy injection phase (at t_b), the γ-ray efficiencies of magnetar and non-magnetar samples are no longer significantly different. The same

conclusion is also manifested in Figure 27a and 27b, where we plot the histograms of η_γ for different samples.

If one accepts that millisecond magnetars are powering some GRBs, it would be interesting to constrain the internal energy dissipation efficiency $\eta_{\rm X}$ (Eq.(3.24)) from the data. In both Fig.23a and Fig.23b, it is found that the Gold sample GRBs have a relatively large L_b value. This is generally consistent with the expectation that a larger $\eta_{\rm X}$ would give rise to an internal plateau (Zhang 2014). In Fig.26c, we compare $L_{\rm K,iso}$ and $L_{\rm X,iso}$. It indeed shows that the Gold sample GRBs have a much higher $\eta_{\rm X}$ than other GRBs. On the other hand, it is curious to ask why there is a gap in this phase space. It appears that some magnetars are particularly efficient to dissipate the magnetar wind energy, while most magnetars are not. Plotting the histograms of $\eta_{\rm X}$ (Fig.27c), it looks indeed like a bimodal distribution of $\eta_{\rm X}$, even though this second high $\eta_{\rm X}$ component is not significant enough. In Fig.28, we present the scatter plots of $\eta_{\rm X}$ against other parameters, including $\eta_\gamma(t_b)$, $E_{\gamma,\rm iso}$, $E_{\rm K,iso}$, and $E_{\rm rot}$. In all cases, the Gold sample (the ones with very high $\eta_{\rm X}$) tend to stick out and emerge as a separate population.

Conclusions and Discussion

In order to address whether (at least) some GRBs might have a magnetar central engine, we have systematically analysed the X-ray data of all the *Swift* GRBs (~ 750) detected before August 2013. By applying some criteria to judge how likely a GRB might harbor a millisecond magnetar central engine, we characterized long GRBs into several samples: Gold, Silver, and Aluminum magnetar samples, as well as the non-magnetar samples. For comparison, we also independently processed the data of short GRBs that might have a magnetar central engine (Rowlinson et al. 2010, 2013). By deriving the basic magnetar parameters P_0 and B_p from the data, we are able to reach two interesting conclusions.

First, it seems that at least for the Gold and Silver sample GRBs, the derived properties seem to be consistent with the expectations of the magnetar central engine model. The consistency includes the following: 1. After beaming correction, the derived P_0 and B_p seem to fall into the reasonable range expected in the magnetar central engine model; 2. The $L_b - t_b$ anti-correlation seems to be consistent with the hypothesis that there is a quasi-universal energy budget defined by the spin energy of the magnetars (Eq.(4.4)); 3. The sum of E_γ and $E_{\rm K}$ is generally smaller than $E_{\rm rot}$, the total energy budget of a magnetar; 4. Most importantly, it seems that the magnetar and non-magnetar samples are different. The robust magnetar sample (Gold + Silver) GRBs all have a beaming-corrected energy smaller than the maximum energy allowed by a magnetar, i.e. $E_{\rm rot,max} \sim 2 \times 10^{52}$ erg. The non-magnetar sample, on the other hand, can exceed this limit. The two samples have two distinct distributions in E_γ, $E_{\rm K}$, and $(E_\gamma + E_{\rm K})$, suggesting that they may be powered by different central engines.

Second, both long and short GRBs can be powered by a millisecond magnetar central engine. The characteristic magnetar signature, an internal plateau, is found in both long and short GRBs, suggesting that different progenitors (both massive star core collapses and compact star mergers) can produce a millisecond, probably supra-massive magnetar as the central engine. The data is consistent that a long GRB magnetar wind is collimated, while a short GRB magnetar wind is essentially isotropic. All these have profound implications in several related fields in high-energy, transient astronomy. For example, if the recently discovered fast radio bursts (FRBs, Lorimer et al. 2007; Thornton et al. 2013) are indeed produced when a supra-massive neutron star collapses into a black hole (Falcke & Rezzolla 2014; Zhang 2014), our analysis suggests that such supra-massive neutron stars very likely do exist in GRBs, and that the FRB/GRB association suggested by Zhang (2014) should be quite common, probably up to near half of the entire GRB population. This is higher than the rate of plausible detections made by Bannister et al. (2012), but that low detection

rate (2 out of 9 GRBs, Bannister et al. 2012) may be due to the sensitivity limit of the Parkes 12 m telescope they have used. A rapid-slewing larger radio telescope would be able to detect more FRB/GRB associations, which would open a new window to study cosmology (Deng & Zhang 2014) and conduct cosmography (Gao et al. 2014). For another example, the conclusion that short GRBs can be powered by a millisecond magnetar with a near isotropic magnetar wind would give rise to relatively bright, early electromagnetic counterparts of gravitational wave bursts due to NS-NS mergers (Zhang 2013; Gao et al. 2013; Yu et al. 2013; Metzger & Piro 2013; Fan et al. 2013), which gives promising prospects of detecting electromagnetic counterparts of gravitational wave signals in the Advanced LIGO/Virgo era.

Our analysis also poses some curious questions. One is regarding the magnetar dissipation efficiency $\eta_{\rm X}$. The results seem to suggest that some magnetars are efficient in dissipating their magnetar wind energy to X-ray radiation, while most others are not. A straightforward inference would be that there might be a dichotomy within the magnetar central engines. A more plausible scenario would be that some (or probably) most normal plateaus (those followed by normal decays) could be also dominated by internal dissipation emission (e.g. Ghisellini et al. 2007; Kumar et al. 2008a,b). They are not identified as internal plateaus because their post-break decay is not steep enough. Physically they may be stable magnetars or supra-massive magnetars with a much later collapsing time, so that the collapsing signature (very steep decay) is not detected. If so, the $\eta_{\rm X}$ distribution may be more spread out, without a clear bimodal distribution. This possibility is worth exploring in the future.

Another mystery is regarding collimation of magnetar wind in short GRBs. Our analysis suggests that at late times the magnetar wind is essentially isotropic. On the other hand, during the prompt emission phase, at least some short GRBs show evidence of collimation (e.g. Burrows et al. 2006; Soderberg et al. 2006; Berger 2013 for a review). There is no well studied short GRB prompt emission model within the

magnetar central engine scenario. Suggested scenarios invoke an early brief accretion phase (Metzger et al. 2008), an early brief differential rotation phase (Fan et al. 2013), or an early brief phase-transition phase (e.g. Cheng & Dai 1996; Chen & Labun 2013). The short GRB could be collimated by the torus within the accretion scenario (Bucciantini et al. 2012).

(a): The photon index and gamma-ray fluence in the BAT band (15-150keV, in units of 10^{-7} erg cm^{-2}). (b): The spectral index of the absorbed power-law model for the plateau or the normal segments. (c): Time interval (from t_1 to t_2) of our XRT light curve fitting; times in units of kilo seconds

GRB	T_{90}	Γ_γ (a)	$S_{\gamma,-7}$ (a)	$\beta_{\rm x}$ (b)	(t_1, t_2) (c)
Gold					
060202	198.9	1.71±0.13	21.3±1.65	1.11±0.03	(0.28,1.7)
060413	147.7	1.68±0.08	35.6±1.47	1.28±0.13	(1.2,253.52)
060522	71.1	1.56±0.15	11.4±1.11	1.18±0.17	(0.2,0.9)
060607A	102.2	1.47±0.08	25.5±1.12	0.67±0.06	(1.52,39.52)
070110	88.4	1.58±0.12	18±2	1.12±0.07	(4.1,28.72)
070616	402.4	1.61±0.04	192±3.47	0.26±0.01	(0.13,2.01)
090419	450	1.38±0.16	25±2	0.30±0.28	(0.12,1.72)
120213A	49	2.37±0.09	19±1	0.95±0.21	(1.04,12.84)
130102A	77.5	1.39±0.18	7.2±0.9	0.80±0.41	(0.18,10)
Silver					
050401	33.3	1.4±0.07	82.2±3.06	0.82±0.15	(0.13,548)
050505	58.9	1.41±0.12	24.9±1.79	1.23±0.04	(2.88,133)
050803	87.9	1.38±0.11	21.5±1.35	1.23±0.12	(0.32,1330)
060108	14.3	2.03±0.17	3.69±0.37	1.21±0.28	(0.75,368)
060526	298.2	2.01±0.24	12.6±1.65	1.16±0.16	(1.02,314)
060604	95	2.01±0.42	4.02±1.06	1.15±0.17	(1.23,824)
060605	79.1	1.55±0.2	6.97±0.9	1.36±0.12	(0.15,103)
060614	108.7	2.02±0.04	204±3.63	1.18±0.09	(4.54,1795)
060729	115.3	1.75±0.14	26.1±2.11	1.24±0.03	(0.52,8968)
060906	43.5	2.03±0.11	22.1±1.36	1.12±0.17	(0.42,258)
060908	19.3	1.01±0.3	28±1.11	1.40±0.30	(0.08,14.8)
061110A	40.7	1.67±0.12	10.6±0.76	1.10±0.32	(3.08,756)
070306	209.5	1.66±0.1	53.8±2.86	1.19±0.08	(0.48,819)
070529	109.2	1.34±0.16	25.7±2.45	0.76±0.24	(0.17,445)
080605	20	1.11±0.14	133±2	0.74±0.16	(0.09,101)
080607	79	1.31±0.04	240±9	1.13±0.15	(0.62,401)
080721	16.2	1.11±0.08	120±10	0.84±0.06	(0.11,2011)
080905B	128	1.78±0.15	18±2	1.22±0.10	(0.22,988)
081008	185.5	1.69±0.07	43±2	0.98±0.11	(0.71,502)
081203A	294	1.54±0.06	77±3	1.04±0.11	(0.2,506)
081221	34	1.21±0.13	181±3	1.29±0.10	(0.25,498)
090423	10.3	0.8±0.5	5.9±0.4	0.92±0.16	(0.39,501)
090618	113.2	1.42±0.09	1050±10	0.72±0.05	(0.58,1998)
090927	2.2	1.8±0.2	2± 0.3	0.92±0.23	(2.52,1003)
091208B	14.9	1.74±0.11	33±2	1.04±0.16	(0.14,969)
100418A	7	2.16±0.25	3.4±0.5	1.27±0.23	(0.51,2002)
111008A	63.5	1.86±0.09	53±3	1.07±0.23	(0.31,987)
111228A	101.2	2.27±0.06	85±2	1.12±0.08	(0.42,2990)
120422A	5.35	1.19±0.24	2.3±0.4	1.22±0.23	(0.49,2011)
121024A	69	1.41±0.22	11±1	0.94±0.14	(2.01,504)
121027A	62.6	1.82±0.09	20±1	1.45±0.11	(40.1,3019)
121128A	23.3	1.32±0.18	69±4	1.32±0.21	(0.21,98.7)
121229A	100	2.43±0.46	4.6±1.3	1.10±0.30	(2.04,205)
SGRBs					
051221A	1.4	1.39±0.06	11.5±0.35	1.07±0.13	(6.02,655)
060801	0.49	1.27±0.16	0.8±0.1	0.43±0.12	(0.08,0.73)
061201	0.6	0.81±0.15	3.24±0.27	1.2±0.22	(0.11,30.9)
070809	1.3	1.69±0.22	1.0±0.1	0.37±0.21	(0.53,67.4)
090426	1.2	1.93±0.22	1.8±0.3	1.04±0.15	(0.13,17.6)
090510	0.3	0.98±0.21	3.4±0.4	0.75±0.12	(0.11,20.7)
100724A	1.4	1.92±0.21	1.6±0.2	0.94±0.23	(0.38,0.89)
101219A	0.6	0.63±0.09	4.6±0.3	0.53±0.26	(0.05,0.27)
130603B	0.18	1.83±0.12	19.2±1.2	1.18±0.18	(0.07,48.1)

Table 1 The γ-ray and X-ray observations results of the "Gold", "Silver", and the short GRB samples

(d): The break time of the lightcurves from our fitting. (e): α_1 and α_2 are the decay slopes before and after the break time. (f): The References of redshift measurements. (REFERENCES): 1: Evans et al.(2009); 2: Vreeswijk et al.(2008); 3: D'Avanzo et al.(2008); 4: Landsman et al.(2008); 5: Salvaterra et al.(2012); 6: Tanvir et al.(2009); 7: Cenko et al.(2009); 8: Levan et al.(2009); 9: Wiersema et al.(2009); 10: Antonelli et al.(2010); 11: Wiersema et al.(2011); 12: Cucchiara et al.(2011); 13: Schulze et al.(2012); 14: Tanvir et al.(2012); 15: Levan et al.(2012); 16: Tanvir et al.(2012); 17: Fynbo et al.(2012); 18: Rowlinson et al.(2013); 19: Thoene et al.(2010); 20: Fong et al.(2014).

GRB	t_b (d)	α_1 (e)	α_2 (e)	χ^2/dof	z (f)
Gold					
060202	0.75±0.08	0.23±0.03	5.79±0.16	563/521	—
060413	26.43±1.12	0.18±0.03	3.42±0.21	79/71	—
060522	0.53±0.06	0.14±0.36	3.15±0.79	12/11	$5.11^{(1)}$
060607A	12.34±0.19	0±0.01	3.4±0.06	132/139	$3.082^{(1)}$
070110	20.4±0.44	0.11±0.05	8.7±0.8	44/46	$2.352^{(1)}$
070616	0.53±0.04	-0.11±0.02	5.29±0.05	224/241	—
090419	0.49±0.07	0.2±0.2	3.44±0.23	77/72	—
120213A	8.03±0.97	0.35±0.06	4.56±0.24	49/53	—
130102A	0.42±0.26	0.22±0.41	5.92±0.57	12/10	—
Silver					
050401	5.86±0.78	0.57±0.02	1.37±0.06	107/92	$2.9^{(1)}$
050505	7.87±1.57	0.19±0.15	1.3±0.06	27/45	$4.27^{(1)}$
050803	15.98±0.18	0.38±0.02	1.89±0.06	95/75	$0.422^{(1)}$
060108	14.24±7.38	0.12±0.08	1.25±0.06	7/7	$2.03^{(1)}$
060526	10.02±4.55	0.31±0.12	1.5±0.23	34/48	$3.21^{(1)}$
060604	11.37±6.8	0.19±0.48	1.17±0.08	35/41	$2.1357^{(1)}$
060605	7.45±0.52	0.45±0.03	2.01±0.05	16/21	$3.78^{(1)}$
060614	49.84±3.62	0.18±0.06	1.9±0.07	70/54	$0.125^{(1)}$
060729	72.97±3.02	0.21±0.01	1.42±0.02	160/459	$0.54^{(1)}$
060906	12.78±3.29	0.3±0.04	1.81±0.1	5/7	$3.685^{(1)}$
060908	0.71±0.17	0.43±0.09	1.56±0.06	98/59	$1.8836^{(1)}$
061110A	73.17±5.67	0.19±0.15	1.16±0.17	7/5	$0.758^{(1)}$
070306	29.69±1.72	0.12±0.02	1.87±0.03	153/132	$1.497^{(1)}$
070529	1.65±0.84	0.64±0.07	1.36±0.05	23/19	$2.4996^{(1)}$
080605	0.44±0.05	0.5±0.05	1.34±0.02	330/289	$1.6398^{(1)}$
080607	1.38±0.19	0.05±0.33	1.68±0.04	103/98	$3.036^{(1)}$
080721	3.09±0.16	0.8±0.01	1.65±0.02	54/49	$2.602^{(1)}$
080905B	4.03±1.22	0.25±0.03	1.46±0.02	94/98	$2.374^{(2)}$
081008	15.92±6.58	0.81±0.03	1.85±0.08	33/38	$1.9685^{(3)}$
081203A	11.23±8.69	1.12±0.01	2.07±0.07	191/163	$2.1^{(4)}$
081221	0.6±0.08	0.3±0.11	1.32±0.02	285/312	$2.26^{(5)}$
090423	4.28±0.76	-0.16±0.07	1.42±0.04	27/33	$8.2^{(6)}$
090618	7.28±1.43	0.67±0.02	1.48±0.03	128/132	$0.54^{(7)}$
090927	8.29±1.32	0.16±0.11	1.24±0.09	19/15	$1.37^{(8)}$
091208B	1.15±0.21	0.16±0.14	1.17±0.03	79/68	$1.063^{(9)}$
100418A	86.82±22.14	-0.11±0.05	1.53±0.06	44/49	$0.6235^{(10)}$
111008A	7.47±2.28	0.29±0.02	1.34±0.02	143/167	$4.9898^{(11)}$
111228A	6.53±2.11	0.22±0.03	1.23±0.01	202/187	$0.7156^{(12)}$
120422A	166.15±22.33	0.27±0.04	1.27±0.14	4/6	$0.283^{(13)}$
121024A	32.98±8.21	0.8±0.06	1.71±0.09	47/52	$2.298^{(14)}$
121027A	144.71±44.87	0.37±0.07	1.52±0.05	54/46	$1.773^{(15)}$
121128A	1.58±0.24	0.52±0.07	1.68±0.04	81/78	$2.2^{(16)}$
121229A	56.39±8.34	0.21±0.12	1.43±0.27	3/5	$2.707^{(17)}$
SGRBs					
051221A	34.32±6.78	0.19±0.08	1.45±0.05	41/44	$0.55^{(18)}$
060801	0.06±0.04	0.67±0.12	4.81±0.62	22/18	$1.131^{(18)}$
061201	1.21±0.26	0.52±0.06	1.87±0.07	16/18	$0.111^{(18)}$
070809	12.86±6.52	-0.01±0.09	1.14±0.13	33/26	$0.219^{(18)}$
090426	0.31±0.18	-0.18±0.16	1.02±0.04	25/19	$2.6^{(18)}$
090510	0.28±0.04	0.62±0.03	2.17±0.05	76/68	$0.903^{(18)}$
100724A	0.52±0.16	0.21±0.12	1.84±0.51	45/33	$1.288^{(19)}$
101219A	0.23±0.15	0.21±0.24	6.82±0.96	38/29	$0.718^{(18)}$
130603B	3.01±0.67	0.38±0.02	1.64±0.04	111/98	$0.356^{(20)}$

Table 2 The γ-ray and X-ray fitting results of the "Gold", "Silver", and the short GRB samples

(a): The jet opening angle (in units of degree (°)) measured from afterglow observations (Racusin et al. 2009; Lu et al. 2011; Nemmen et al. 2012), or assumed as $\theta_j = 5°$ if no observation is available. SGRBs are assumed to be isotropic. (b): $E_{\gamma,\rm iso}$ is calculated using fluence and redshift extrapolated into 1-10000 keV (rest frame) with a spectral model and a k-correction, in units of 10^{52} erg. (c): Isotropic luminosity of break time (in units of 10^{49} erg s^{-1}), and the spin-down time (in units of 10^3s)

GRB	θ_j (a)	$E_{\gamma,\rm iso,52}$ (b)	$L_{b,49}$ (c)	τ_3 (c)
Gold				
060522	5	0.71±0.71	1.38±0.22	0.06±0.01
060607A	5	9.08±7.11	0.58±0.07	0.13±0.02
070110	5	3.09±2.51	0.07±0.03	3.68±0.06
Silver				
050401	5	32^{+26}_{-7}	0.47±0.01	1.51±0.21
050505	1.67 ± 0.35	16^{+13}_{-3}	0.41±0.01	1.49±0.30
050803	5	$0.24^{+0.24}_{-0.08}$	(8.92±0.31)e-4	11.24±0.13
060108	5	$0.59^{+0.84}_{-0.08}$	(5.96±0.48)e-3	4.70±2.44
060526	3.61 ± 0.57	$5.2^{+5.6}_{-0.4}$	(3.91±0.27)e-2	2.38±1.08
060604	5	$0.5^{+0.12}_{-0.1}$	(1.15±0.05)e-2	3.63±2.17
060605	1.55 ± 0.57	$2.5^{+3.1}_{-0.6}$	0.13±0.01	1.56±0.11
060614	7.57 ± 2.29	$0.24^{+0.04}_{-0.04}$	(2.49±0.08)e-5	44.31±3.22
060729	18 ± 1.61	$0.33^{+0.29}_{-0.06}$	(1.56±0.02)e-3	47.38±1.96
060906	1.15 ± 0.12	13^{+12}_{-1}	(3.08±0.21)e-2	2.73±0.70
060908	0.46 ± 0.29	7^{+4}_{-1}	0.26±0.07	0.25±0.06
061110A	5	$0.28^{+0.28}_{-0.06}$	(3.83±0.81)e-5	41.62±3.23
070306	3.38 ± 1.72	6^{+5}_{-1}	(2.06±0.06)e-2	11.89±0.69
070529	5	9^{+9}_{-3}	0.12±0.01	0.47±0.24
080605	5	21^{+9}_{-4}	1.49±0.16	0.17±0.02
080607	5	280^{+130}_{-90}	1.36±0.27	0.34±0.05
080721	5	110^{+110}_{-50}	2.50±0.13	0.86±0.04
080905B	5	$3.4^{+3.1}_{-0.6}$	0.31±0.01	1.20±0.36
081008	5	6^{+3}_{-1}	(1.19±0.06)e-2	5.36±2.22
081203A	5	17^{+13}_{-4}	(3.23±0.11)e-2	3.62±2.80
081221	5	282.29±4.68	1.72±0.20	0.18±0.02
090423	> 12	8^{+1}_{-1}	0.82±0.04	0.47±0.08
090618	6.7 ∓ 1.08	15^{+1}_{-1}	(1.62±0.02)e-2	4.73±0.93
090927	5	0.43±0.06	(5.16±0.27)e-3	55.36±32.68
091208B	7.3 ± 1.42	4.88±0.30	0.05±0.01	0.56±0.10
100418A	5	0.14±0.02	(1.16±0.11)e-4	53.48±13.64
111008A	5	85.23±4.82	0.72±0.02	1.25±0.38
111228A	5	5.45±0.13	(8.48±0.24)e-3	3.81±1.23
120422A	5	0.13±0.02	(2.31±0.26)e-6	129.5±17.4
121024A	5	10.78±0.98	(6.30±0.45)e-3	10.01±2.49
121027A	5	6.61±0.33	(3.38±0.16)e-3	52.19±16.18
121128A	5	78.91±4.57	0.38±0.06	0.50±0.08
121229A	5	6.64±1.88	(1.81±0.25)e-3	15.21±2.25
SGRBs				
051221A	-	$0.28^{+0.21}_{-0.11}$	24.71±4.97	(8.8±0.23)e-3
060801	-	$0.17^{+0.02}_{-0.02}$	0.03±0.02	8.7±4.1
061201	-	$0.018^{+0.002}_{-0.001}$	1.08±0.23	0.08±0.01
070809	-	$0.001^{+0.001}_{-0.001}$	12.14±5.33	(4.5±2.5)e-3
090426	-	$0.42^{+0.5}_{-0.04}$	0.09±0.05	1.9±1.2
090510	-	$0.3^{+0.5}_{-0.2}$	0.15±0.02	2.1±0.2
100724A	-	$0.07^{+0.01}_{-0.01}$	0.23±0.07	0.23±0.03
101219A	-	$0.48^{+0.03}_{-0.03}$	0.13±0.06	9.7±3.8
130603B	-	$0.22^{+0.02}_{-0.02}$	2.22±0.49	0.11±0.01

Table 3 The properties of GRBs with known redshifts in our "Gold", "Silver", and short GRB samples

(d): Dipolar magnetic field strength at the polar cap in units of $10^{15}G$, and the initial spin period of the magnetar in units of milliseconds, with an assumption of an isotropic wind. (e): The same as d, but with beaming correction made. (f): The rotational energy (in units of 10^{50} erg) of the magnetar assuming $R_6 = 1$ and $M = 1.4M_\odot$.

GRB	$B_{p,15}$	$P_{0,-3}$ (d)	$B_{p,\theta,15}$ (d)	$P_{0,\theta,-3}$ (e)	$E_{\rm rot,50}$ (e)	(f)
Gold						
060522		2.34±0.71	1.19±0.59	37.93±11.42	19.28±9.51	0.54±0.29
060607A		0.18±0.04	0.44±0.10	2.91±0.67	7.15±1.58	3.91±1.29
070110		0.23±0.11	0.74±0.36	3.79±1.78	11.97±5.84	1.39±0.76
Silver						
050401		0.09±0.02	0.15±0.02	1.44±0.32	2.43±0.34	34.20±8.11
050505		0.07±0.02	0.13±0.03	3.21±1.20	6.28±1.45	5.12±1.78
050803		0.07±0.01	0.21±0.01	1.22±0.04	3.39±0.08	17.37±7.88
060108		0.21±0.36	0.53±0.50	3.28±0.58	8.65±2.43	2.68±1.79
060526		0.10±0.09	0.21±0.18	2.14±1.59	4.74±1.98	8.93±2.69
060604		0.21±0.08	0.49±0.36	3.39±1.87	7.98±3.88	3.16±2.45
060605		0.03±0.01	0.06±0.01	1.68±0.23	3.19±0.31	19.57±3.35
060614		0.06±0.01	0.32±0.03	0.69±0.10	3.42±0.34	17.06±2.92
060729		0.06±0.01	0.33±0.02	0.25±0.02	1.48±0.07	91.23±7.84
060906		0.04±0.02	0.09±0.04	2.55±1.70	6.36±2.78	4.94±2.55
060908		0.57±0.41	0.33±0.17	100.6±73.24	59.08±30.06	0.06±0.03
061110A		0.39±0.09	2.32±0.41	6.31±1.43	37.68±6.71	0.14±0.04
070306		0.02±0.01	0.06±0.01	0.36±0.04	1.39±0.11	104.2±14.5
070529		0.44±0.17	0.39±0.33	7.06±1.58	6.33±3.63	5.02±3.55
080605		0.47±0.11	0.22±0.03	7.63±1.75	3.52±0.56	16.26±4.22
080607		0.13±0.05	0.11±0.03	2.10±0.77	1.72±0.47	67.85±26.14
080721		0.07±0.01	0.09±0.01	1.18±0.12	1.45±0.10	96.86±13.41
080905B		0.11±0.08	0.16±0.07	1.84±1.30	2.58±1.10	30.32±15.55
081008		0.08±0.10	0.22±0.16	1.29±0.63	3.60±1.63	15.45±10.29
081203A		0.06±0.01	0.13±0.07	0.93±0.39	2.17±0.73	42.65±4.11
081221		0.38±0.11	0.21±0.04	6.19±1.79	3.35±0.67	18.01±5.61
090423		0.19±0.07	0.28±0.07	1.30±0.47	1.88±0.44	59.46±22.42
090618		0.25±0.09	0.48±0.13	3.08±1.09	5.79±1.23	5.98±1.94
090927		0.05±0.02	0.36±0.25	0.73±0.21	5.82±0.86	6.01±1.04
091208B		0.96±0.60	0.72±0.34	10.71±6.65	8.02±3.77	3.11±1.67
100418A		0.05±0.03	0.32±0.13	0.80±0.51	5.23±2.16	7.31±3.65
111008A		0.05±0.04	0.11±0.04	0.88±0.59	1.67±0.67	72.35±35.86
111228A		0.36±0.25	0.64±0.26	5.78±1.19	10.32±4.22	1.89±0.94
120422A		0.42±0.12	3.80±0.75	6.85±1.96	61.66±12.09	0.05±0.02
121024A		0.06±0.02	0.26±0.09	1.05±0.58	4.19±1.48	11.38±5.16
121027A		0.02±0.01	0.15±0.07	0.29±0.15	2.41±1.09	34.58±18.26
121128A		0.21±0.08	0.18±0.05	3.39±1.29	2.98±0.82	22.61±8.72
121229A		0.07±0.02	0.34±0.08	1.06±0.36	5.55±1.32	6.52±2.27
SGRBs						
051221A		0.57±0.01	2.47±0.16	-	-	22.88±4.41
060801		11.21±4.21	1.95±0.34	-	-	52.62±24.26
061201		6.01±0.12	4.59±0.05	-	-	9.48±1.88
070809		2.06±1.03	5.55±1.25	-	-	6.49±4.31
090426		4.79±3.11	1.87±0.53	-	-	57.46±5.44
090510		5.05±0.26	1.87±0.05	-	-	57.36±3.02
100724A		8.22±0.59	4.14±0.15	-	-	11.67±1.87
101219A		2.86±0.81	0.96±0.13	-	-	217.7±71.5
130603B		2.16±0.12	2.61±0.07	-	-	29.32±1.63

Table 4 The magnetar parameters of GRBs with known redshifts in our "Gold", "Silver", and short GRB samples

	Gold+Silver	Gold+Silver+Aluminum	Non-magnetar
$E_{\gamma,\mathrm{iso}}$	(52.87 ± 0.33) erg	(52.89 ± 0.09) erg	(53.20 ± 0.04) erg
$E_{\mathrm{K,iso}}$	(53.11 ± 0.09) erg	(53.99 ± 0.06) erg	(53.94 ± 0.02) erg
$E_{\mathrm{total,iso}}$	(53.31 ± 0.05) erg	(54.05 ± 0.05) erg	(54.01 ± 0.05) erg
	Silver	Silver+Aluminum	Non-magnetar
E_{γ}	(48.55 ± 0.11) erg	(49.06 ± 0.13) erg	(50.11 ± 0.12) erg
E_{K}	(50.55 ± 0.17) erg	(51.13 ± 0.12) erg	(51.54 ± 0.18) erg
E_{total}	(50.62 ± 0.07) erg	(51.06 ± 0.09) erg	(51.81 ± 0.11) erg

Table 5 The center value of Gaussian fitting of the distributions

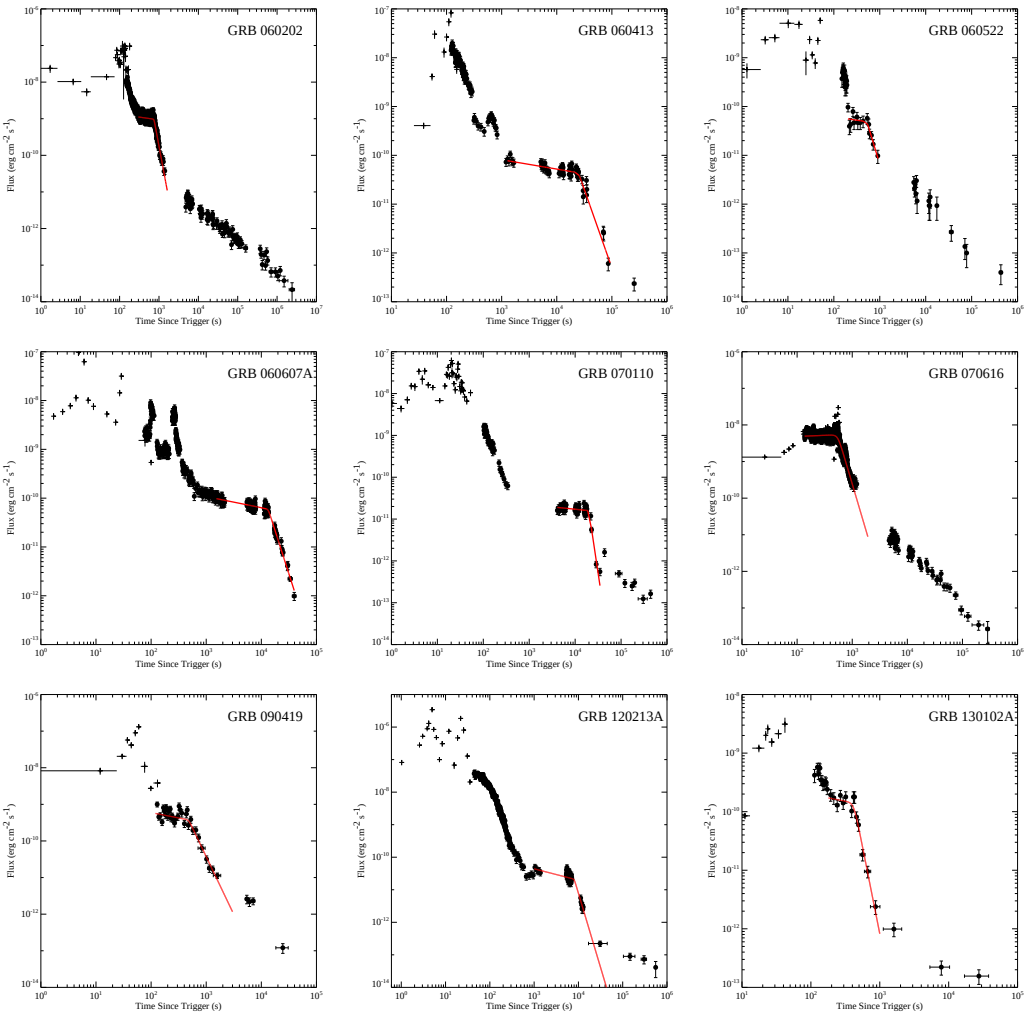

Figure 17 . The X-ray light curves of the GRBs in our Gold sample. Plus signs are BAT data extrapolated to the XRT band, and points (with error bars) are the XRT data. The red solid curves are the best fits of the smooth broken power law model to the data.

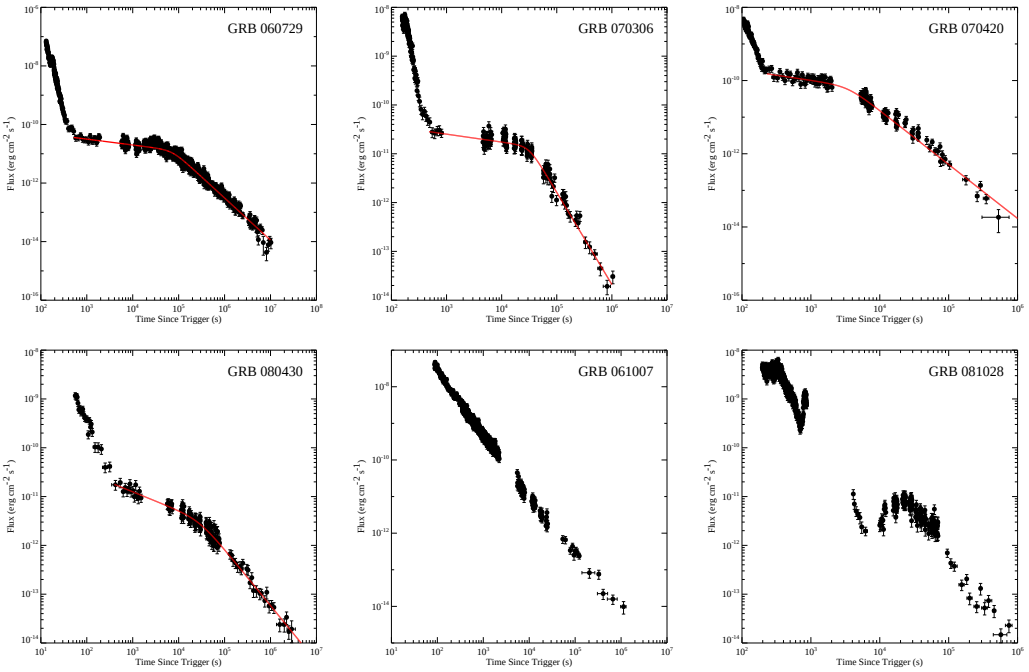

Figure 18 . Two cases of the X-ray light curves in our Silver (GRB 060729 and 070306), Aluminum (GRB 070420 and 080430), and Non-magnetar (GRB 061007 and 081028) sample. The red solid curves are the best fits of the smooth broken power law model to the data.

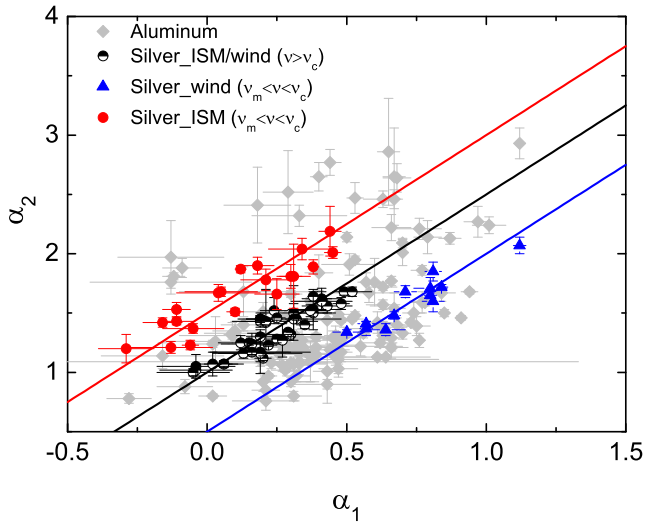

Figure 19 . The temporal decay indices α_1 vs. α_2 for the "Silver" and "Aluminum" samples. The three solid lines indicate the closure relations of three specific external shock models invoking energy injection with the parameter $q = 0$, as is expected in the millisecond magnetar central engine model. The colored data points belong to the Silver sample, while grey data points belong to the Aluminum sample.

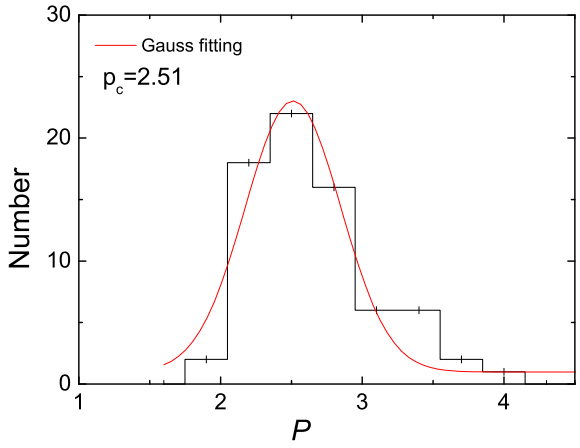

Figure 20 . The distribution of electron spectral index p derived from the Silver sample. The solid line is the best Gaussian fit with a center value $p_c = 2.51$..

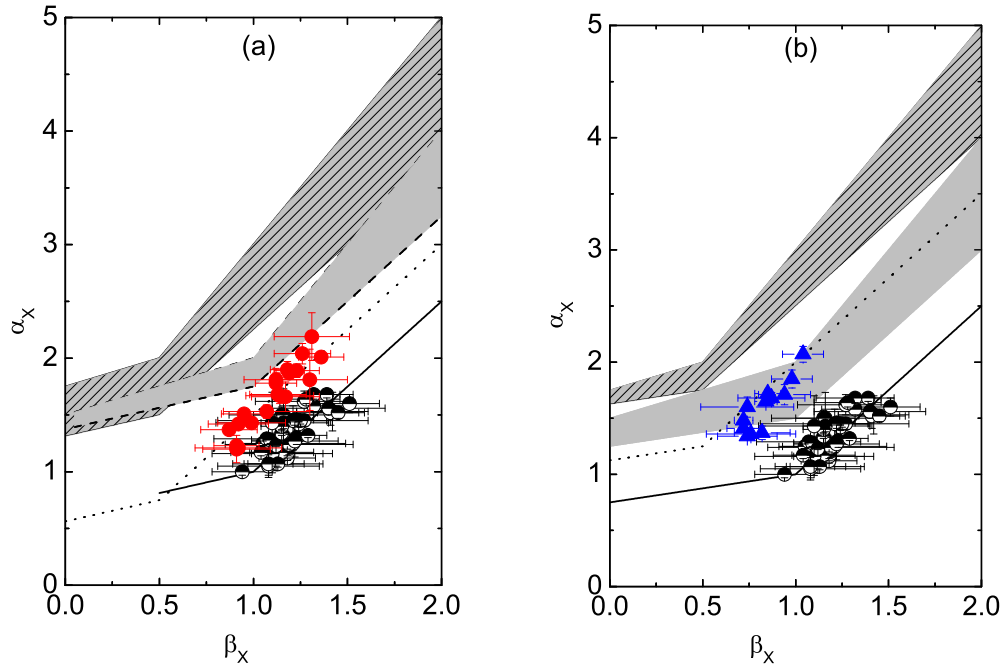

Figure 21 . The temporal decay index α against spectral index β along with the closure relations of the external shock models for the "Silver" sample. (a) The case of the ISM model: the solid line (pre- jet break) and the shaded region (post jet break) are for the spectral regime I ($\nu_x > \max(\nu_{\rm m}, \nu_{\rm c})$), while the dashed line (pre- jet break) and hatched region (post jet break) are for the spectral regime II ($\nu_m < \nu_x < \nu_c$). Half-solid (black) dots and solid (red) dots are for regime I and II, respectively. (b) The case of the wind medium case. Same conventions, except that triangles (blue) denote the spectral regime II.

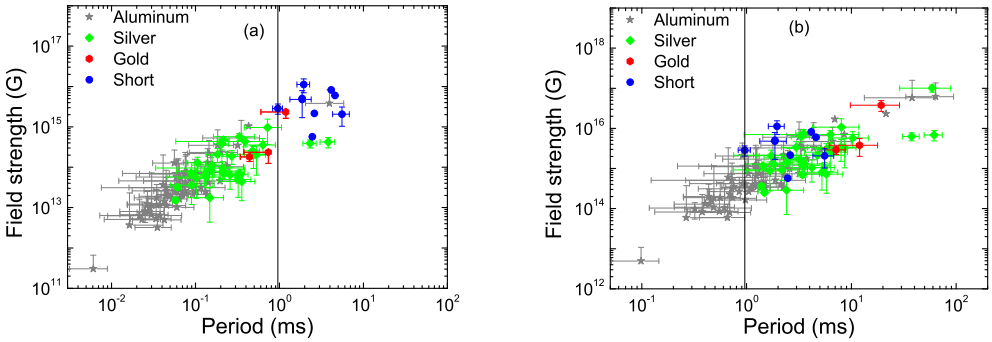

Figure 22 . The inferred magnetar parameters, initial spin period P_0 vs. surface polar cap magnetic field strength B_p derived for different magnetar samples: Gold (red hexagons), Silver (green diamonds), Aluminum (grey), and short GRBs (blue). (a) The case of isotropic winds; (b) The case with beaming corrections. The vertical solid line is the breakup spin-period for a neutron star (Lattimer & Prakash 2004).

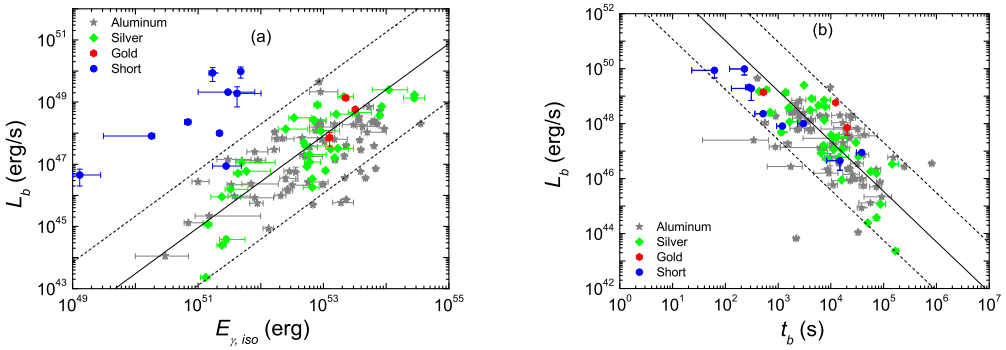

Figure 23 . The $L_b - E_{\gamma,iso}$ and $L_b - t_b$ correlations for the GRBs in various magnetar samples. The color convention is the same as Fig.5. The solid line is a power-law fitting to the Gold and Silver sample GRBs, and the two dashed lines denote the 2σ region of the fits.

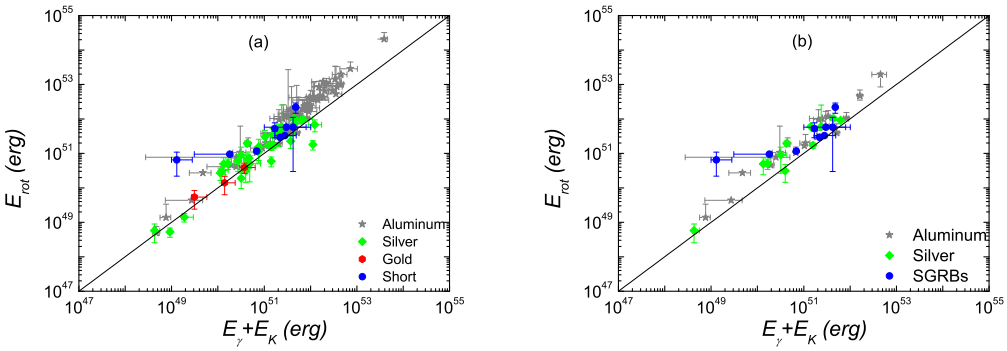

Figure 24 . A comparison between $(E_\gamma + E_{\rm K})$ and $E_{\rm rot}$. The color convention is the same as Fig.23.

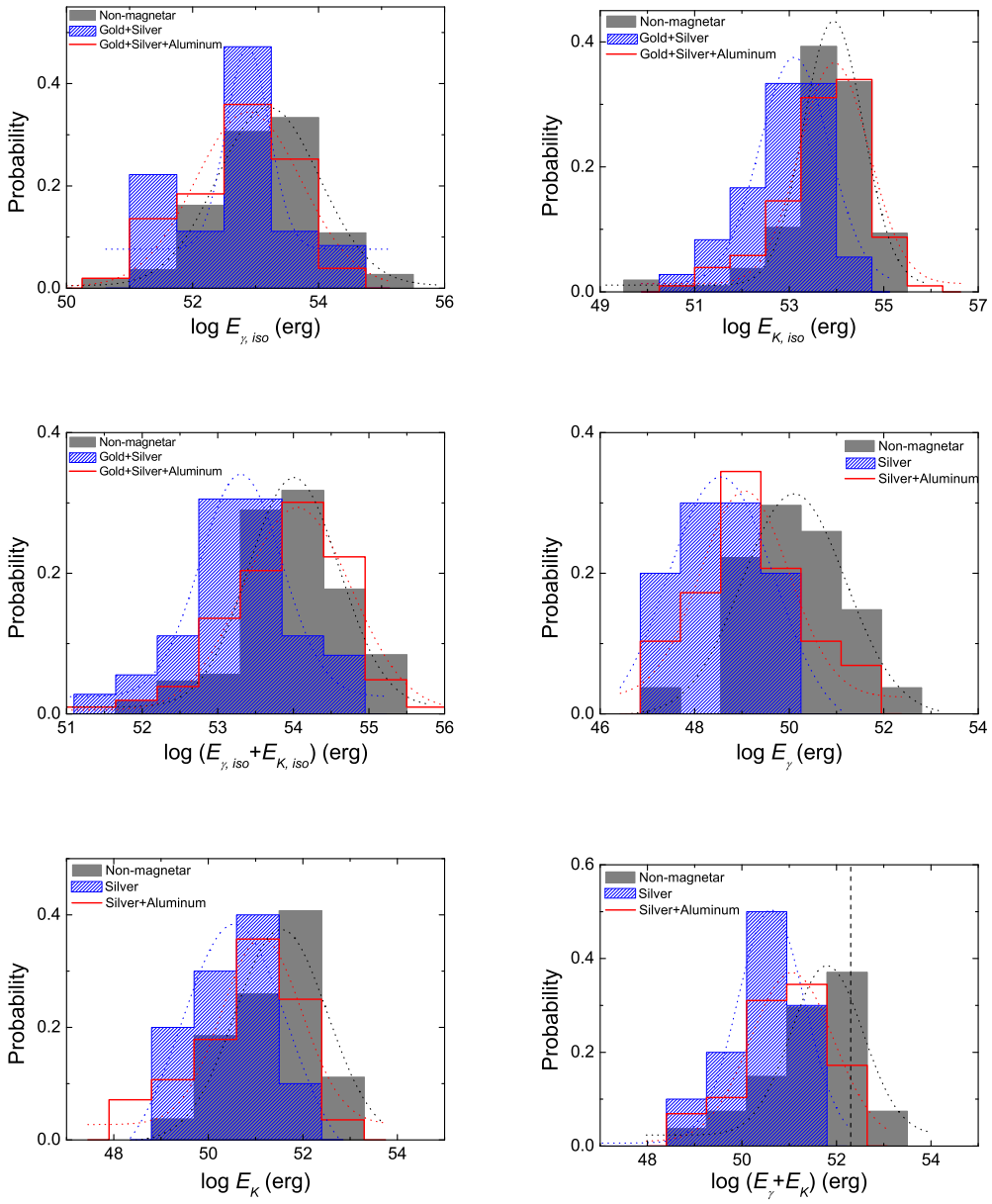

Figure 25 . Comparisons between the energy histograms of the non-magnetar sample and the magnetar samples. The non-magnetar, Gold+Silver, and Gold+Silver+Aluminum sample histograms are denoted as grey filled, blue hatched, and red open histograms, respectively. Best-fit Gaussian profiles are denoted in black, blue, and red dotted lines, respectively. The six panels denote histograms of $E_{\gamma,\rm iso}$, $E_{\rm K,iso}$, $(E_{\gamma,\rm iso} + E_{\rm K,iso})$, $(E_\gamma$, $E_{\rm K}$, and $(E_\gamma + E_{\rm K})$, respectively.

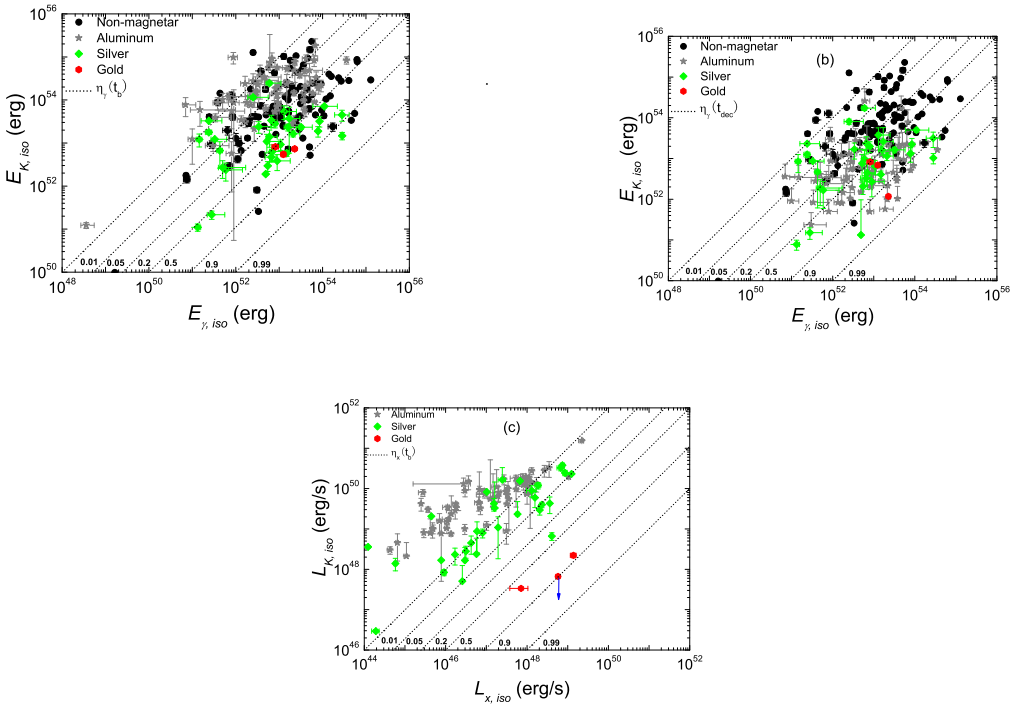

Figure 26 . (a) The $E_{\gamma,\rm iso} - E_{\rm K,iso}$ scattered plot for all the GRBs with redshift measurements in our samples: Gold (red), Silver (green), Aluminum (grey), and non-magnetar (black). slanted dashed lines mark the constant γ-ray efficiency (η_γ) lines. $E_{\rm K,iso}$ is calculated at t_b; (b) Same as (a), but with $E_{\rm K,iso}$ calculated at t_{dec}; (c) The $L_{\rm X,iso} - L_{\rm K,iso}$ scattered plot for the magnetar samples. Gold (red), Silver (green), and Aluminum (grey). The constant X-ray efficiency $\eta_{\rm X}$ lines are over plotted. The $L_{\rm X,iso}$ value of silver and aluminum sample GRBs are all upper limits. For one Gold sample GRB, $L_{\rm K,iso}$ is an upper limit (denoted in the figure).

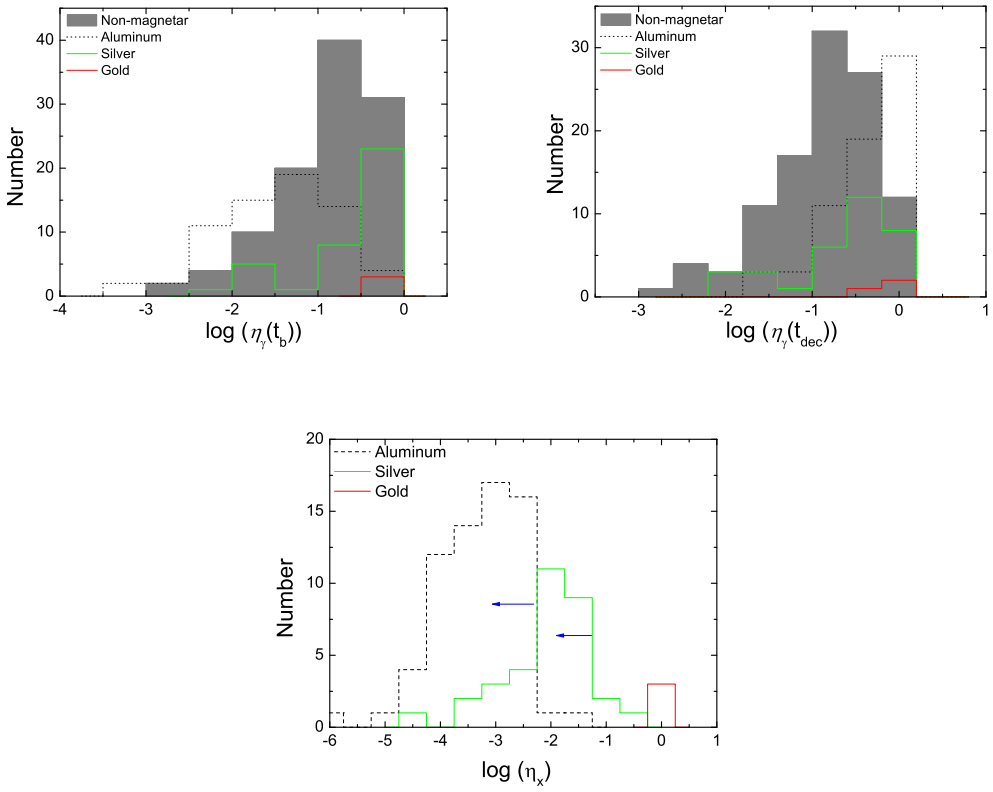

Figure 27 . Histograms of $\eta_\gamma(t_b)$, $\eta_\gamma(t_{dec})$ and $\eta_{\rm X}$ of our samples. For $\eta_{\rm X}$, the silver and aluminum samples only give upper limits.

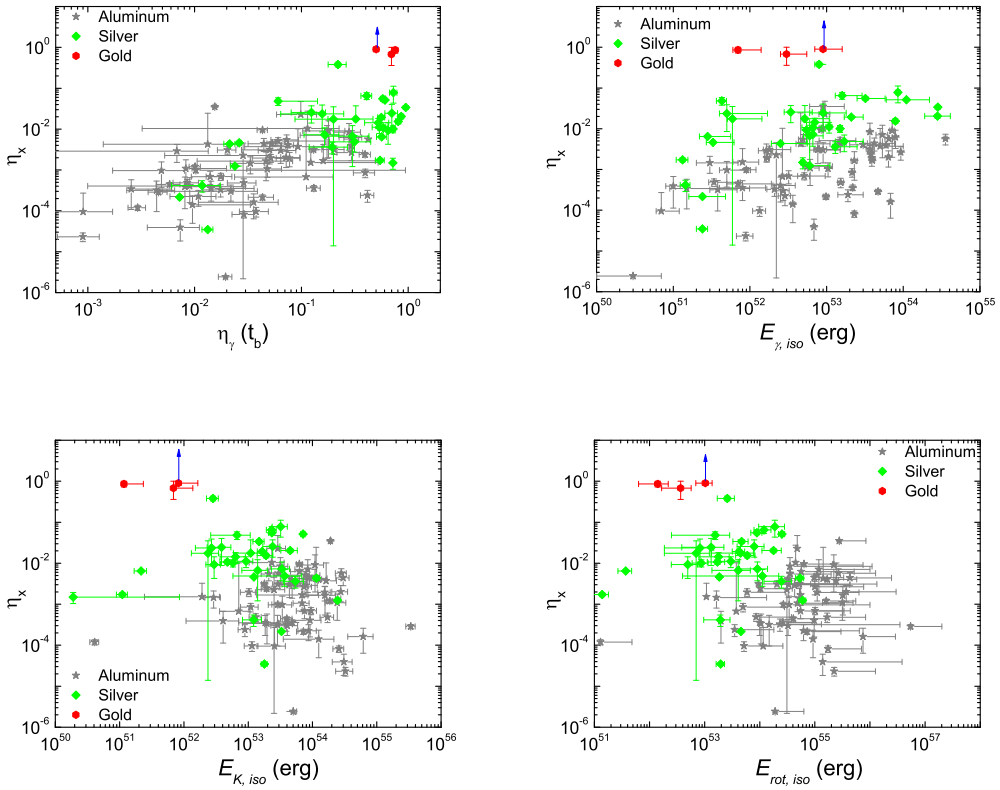

Figure 28 . The scatter plots of the X-ray efficiency $\eta_{\rm X}$ vs. several parameters: $\eta_\gamma(t_b)$, $E_{\gamma,\rm iso}$, $E_{\rm K,iso}$, and $E_{\rm rot}$. Color conventions are the same as Fig.5. The $\eta_{\rm X}$ values of all Silver and Aluminum sample GRBs are all upper limits. The blue arrow shows the lower limit of one GRB in the Gold sample.

CHAPTER 4

THE MILLISECOND MAGNETAR CENTRAL ENGINE IN SHORT GRBS

This chapter is part of the following published paper :

Hou-Jun Lü., Zhang B., Wei-Hua Lei., Ye Li., Paul D Lasky., 2015, The Astrophysics Journal, (Accepted, arXiv 1510.02589)

Gamma-ray bursts (GRBs) are classified into "long soft" (LGRB) and "short hard" (SGRB) categories based on the observed duration (T_{90}) and hardness ratio (HR) of their prompt gamma-ray emission (Kouveliotou et al. 1993). Long GRBs are found to be associated with core-collapse supernovae (SNe; e.g. Galama et al. 1998; Hjorth et al. 2003; Stanek et al. 2003; Campana et al. 2006; Xu et al. 2013), and occur typically in irregular galaxies with intense star formation (Fruchter et al. 2006). They are likely related to deaths of massive stars, and the "collapsar" model has been widely accepted to be the standard paradigm for long GRBs (Woosley 1993; MacFadyen & Woosley 1999). The leading central engine model is a hyper-accreting black hole (e.g. Popham et al. 1999; Lei et al. 2013). Alternatively, a rapidly spinning, strongly magnetized neutron star (millisecond magnetar) may be formed during the core collapse. In this scenario, magnetic fields extract the rotation energy of the magnetar to power the GRB outflow (Usov 1992; Thompson 1994; Dai & Lu 1998; Wheeler et al. 2000; Zhang & Mészáros 2001; Metzger et al. 2008, 2011; Lyons et al. 2010; Bucciantini et al. 2012; Lü & Zhang 2014).

In contrast, short GRBs are found to be associated with nearby early-type galaxies with little star formation (Gehrels et al. 2005; Bloom et al. 2006; Barthelmy et al. 2005; Berger et al. 2005), to have a large offset from the center of the host galaxy (e.g. Fox et al. 2005; Fong et al. 2010), and to have no evidence of an associated supernova (Kann et al. 2011, Berger 2014 and references therein). The evidence points towards an origin that does not involve a massive star. The leading scenarios include the merger of two neutron stars (NS-NS, Paczýnski 1986; Eichler et al. 1989)

or the merger of a neutron star and a black hole (NS-BH, Paczýnski 1991). For NS-NS mergers, the traditional view is that a BH is formed promptly or with a short delay up to hundreds of milliseconds (e.g. Liu et al. 2012; Rosswog et al. 2003; Rezzolla et al. 2011). Observations of short GRBs with *Swift*, on the other hand, indicated the existence of extended central engine activities following at least some short GRBs, in the form of extended emission (Norris & Bonnel 2006), X-ray flares (Barthelmy et al. 2005; Campana et al. 2006), and more importantly, "internal plateaus" with rapid decay at the end of the plateaus (Rowlinson et al. 2010, 2013). These observations are difficult to interpret within the framework of a black hole central engine, but are consistent with having a rapidly spinning millisecond magnetar as the central engine (e.g. Dai et al. 2006; Gao & Fan 2006; Metzger et al. 2008; Rowlinson et al. 2010, 2013; Gompertz et al. 2013, 2014).

About 20% of short GRBs detected with *Swift* have extended emission (EE) (Sakamoto et al. 2011) following the initial short, hard spike. Such EE typically has a lower flux than the initial spike, but can last for tens of seconds (e.g. Perley et al. 2009). The first short GRB with EE detected with *Swift* was GRB 050724, which had a hard spike $T_{90} \sim 3$s followed by a soft tail with a duration about ∼150 s in the *Swift* Burst Alert Telescope (BAT; Barthelmy et al. 2005) band. The afterglow of this GRB lies at the outskirt of an early-type galaxy at a redshift of z=0.258. It is therefore a "smoking-gun" burst of the compact star merger population (Barthelmy et al. 2005; Berger et al. 2005). A special case is GRB 060614, whose light curve was characterized by a short/hard spike (with a duration $\sim$ 5s) followed by a series of soft gamma-ray pulses lasting ∼100 s. Observationally it belongs to a long GRB without an associated supernova (with very deep upper limits of the SN light, e.g. Gal-Yam et al. 2006; Fynbo et al. 2006; Della Valle et al. 2006). Some of its prompt emission properties, on the other hand, are very similar to a short GRB (e.g. Gehrels et al. 2006). Through simulations, Zhang et al. (2007b) showed that if this burst were a

factor of 8 less luminous, it would resemble GRB 050724 and appear as a short GRB with EE. Norris & Bonnell (2006) found a small fraction of short GRBs in the BATSE catalog qualitatively similar to GRB060614. It is interesting to ask the following two questions: are short GRBs with EE different from those without EE? What is the physical origin of the EE?

Swift observations of the X-ray afterglow of short GRBs, on the other hand, give some interesting clues. A good fraction of *Swift* short GRBs exhibit an X-ray plateau followed by a very sharp drop with a temporal decay slope more than 3. The first case was GRB 090515 (Rowlinson et al. 2010). It showed a nearly flat plateau extending to over 180 s before rapidly falling off with a decay slope $\alpha \sim 13$. Such a rapid decay cannot be accommodated in any external shock model, so that the entire X-ray plateau emission has to be attributed to the internal dissipation of a central engine wind. Such an "internal plateau" was observed in some long GRBs before (e.g. Troja et al. 2007; Lyons et al. 2010), but are also commonly observed in short GRBs (Rowlinson et al. 2013). These plateaus can be interpreted as internal emission of a spinning-down magnetar which collapses into a black hole at the end of the plateau (Troja et al. 2007; Rowlinson et al. 2010; Zhang 2014).

If magnetars are indeed operating in some short GRBs, several questions emerge: What fraction of short GRBs have a millisecond magnetar central engine? What are the differences between short GRBs with EE and those without EE but having an internal plateau? Is the total energy of the magnetar candidates consistent with the maximum rotation energy of the magnetars according to the theory? What are the physical parameters of the magnetar candidates derived from observational data? How can one use the data to constrain the equation of state (EoS) of neutron stars?

This chapter aims to address these interesting questions through a systematic analysis of both *Swift*/BAT and X-Ray Telescope (XRT) data. The data reduction details and the criteria for sample selection are presented in first section. Then, the

observational properties of short GRBs and their afterglows are presented. The physical parameters of the putative magnetars are derived and their statistical properties are presented. The implications on the NS EoS are discussed. The conclusions are drawn at last with some discussion.

Data reduction and sample selection criteria

The *Swift* BAT and XRT data are downloaded from the *Swift* data archive[1]. We systematically process the BAT and XRT GRB data to extract lightcurves and time resolved spectra. We developed an IDL script to automatically download and maintain all the *Swift* BAT data. The HEAsoft package *version 6.10*, including *bateconvert*, *batbinevt Xspec*, *Xselect*, *Ximage*, and the *Swift* data analysis tools are used for the data reduction. The details of the data analysis method can be found in several previous papers (Zhang et al. 2007c; Liang et al. 2007; Lü et al. 2014) in our group, and Sakamoto et al. (2008).

We analyze 84 short GRBs observed with *Swift* between 2005 January and 2014 August. Among them, 44 short GRBs are either too faint to be detected in the X-ray band, or do not have enough photons to extract a reasonable X-ray lightcurve. Our sample therefore only comprises 40 short GRBs, including 8 with EE.

We extrapolate the BAT (15-150 keV) data to the XRT band (0.3-10 KeV) by assuming a single power law spectrum (see also O'Brien et al. 2006; Willingale et al. 2007; Evans et al. 2009). We then perform a temporal fit to the lightcurve with a

[1]http://www.swift.ac.uk/archive/obs.php?burst=1

smooth broken power law in the rest frame[2]

$$F = F_0 \left[\left(\frac{t}{t_b} \right)^{\omega\alpha_1} + \left(\frac{t}{t_b} \right)^{\omega\alpha_2} \right]^{-1/\omega} \tag{4.1}$$

to identify a possible plateau in the lightcurve. Here t_b is the break time, $F_b = F_0 \cdot 2^{-1/\omega}$ is the flux at the break time t_b, α_1 and α_2 are decay indices before and after the break, respectively, and ω describes the sharpness of the break. The larger the ω parameter, the sharper the break. An IDL routine named "mpfitfun.pro" is employed for our fitting (Markwardt 2009). This routine performs a Levenberg-Marquardt least-square fit to the data for a given model to optimize the model parameters.

Since the magnetar signature typically invokes a plateau phase followed by a steeper decay (Zhang & Mészáros 2001), we search for such a signature to decide how likely a GRB is powered by a magnetar. Similar to our earlier work (Lü & Zhang 2014), we introduce three grades to define the likelihood of a magnetar engine:

- **The internal plateau (Internal) sample**: This sample is defined by those bursts that exhibit a plateau followed by a decay with t^{-2} or steeper than 3. The t^{-2} decay is expected by the magnetar dipole spindown model (Zhang & Mészáros 2001), while a slope steeper than 3 is an indication that the emission is powered by internal dissipation of the magnetar wind, since essentially no external shock model can account for such a steep decay. This sample is similar to the "Gold" sample defined by Lü & Zhang (2014)[3], but with the inclusion

[2]Another empirical model to fit GRB X-ray afterglow lightcurves was the one introduced by Willingale et al. (2007, 2010). The function was found to be a good fit of the external plateaus of long GRBs (e.g. Dainotti et al. 2010), but cannot fit the internal plateaus that are likely due to a magnetar origin (e.g. Lyons et al. 2010). We have tried to use the Willingale function to fit the data in our sample, but the fits are not good. This is because our short GRB sample includes a large fraction of internal plateaus. We therefore do not use the Willingale function to fit the lightcurves in this paper.

[3]Lü & Zhang (2014) studied the magnetar engine candidates for long GRBs. The grades defined in that paper were based on the following criteria: Gold sample: those GRBs that dispaly an "internal plateau"; Silver sample: those GRBs that display an "external plateau", whose energy injection parameter q is consistent with being 0, as predicted by the dipole spindown model of GRBs; Aluminum sample: those GRBs that display an external plateau, but the derived q parameter is not

of two GRBs with a t^{-2} decay following the plateau. These two GRBs (GRB 061201 and GRB 070714B) also have a plateau index close to 0 as demanded by the magnetar spindown model, and therefore are strong candidates of magnetar internal emission. For those cases with a post-plateau decay index steeper than 3, the rapid decay at the end of plateau may mark the implosion of the magnetar into a black hole (Troja et al. 2007; Zhang 2014). There are altogether 20 short GRBs identified to have such a behavior, 13 of which have redshift measurements, and 7 of which are short GRBs with EE. For these latter GRBs, the extrapolated X-ray lightcurves from the BAT band in the EE phase resemble the internal plateaus directly detected in the XRT band in other GRBs. The light curves of these 22 GRBs are presented in Fig.29, along with the smooth broken-power-law fits. The fitting parameters are summarized in Table 4.

- **The external plateau (External) sample**: This sample includes the GRBs with a plateau phase followed by a normal decay segment, with the post-decay index close to -1. The pre- and post-break temporal and spectral properties are consistent with the external forward shock model, with the plateau phase being due to continuous energy injection into the blastwave. This sample is similar to the Silver and Aluminum samples in Lü & Zhang (2014). We identified 10 GRBs in this group[4]. The XRT lightcurves are presented in Figure 30 along with the smooth broken-power-law fits. The fitting results are presented in Table 4.

- **No plateau (Non) sample**: We identify 8 GRBs that do not have a significant plateau behavior. They either have a single power-law decay, or have erratic flares that do not present a clear magnetar signature.

Figure 31 collects all the lightcurves of the GRBs in our samples. The Internal

consistent with 0; Non-magnetar sample: those GRBs that do not show a clear plateau feature.

[4]The SN-less long GRB 060614 is included in this category. It has EE and an additional external plateau at late times.

sample with or without EE are collected in Fig.31(a,b); the External sample (without EE) are collected in Fig.31(c); and the Non sample are collected in Fig.31(d).

Derived physical parameters and statistics

In this section, we derive physical parameters of the short GRBs in various samples, and perform some statistics to compare among different samples.

Extended emission and internal plateau

Our first task is to investigate whether short GRBs with EE are fundamentally different from those without EE. The EE has been interpreted within the magnetar model as the epoch of tapping spin energy of the magnetar (Metzger et al. 2008; Bucciantini et al. 2012). On the other hand, a good fraction of short GRBs without EE have an internal plateau lasting for hundreds of seconds, which can be also interpreted as internal emission of a magnetar during the spindown phase (Troja et al. 2007; Yu et al. 2010; Rowlinson et al. 2013; Zhang 2014). It would be interesting to investigate whether there is a connection between the two groups of bursts.

Analyzing the whole sample, we find that the short GRBs with EE do not show a plateau in the XRT band (except GRB 060614, which shows an external plateau at a later epoch). Extrapolating the BAT data to the XRT band, the EE appears as an internal plateau (Fig.29). Fitting the joint lightcurve with a broken power-law model, one finds that there is no significant difference in the distribution and cumulative distribution of the plateau durations for the samples with and without EE (Fig.32a). The probability (p) that the two samples are consistent with one another, as calculated using a student's t-test, is 0.65.[5] Figure 32b shows the redshift distributions of those short GRBs in our sample that have redshift measurements. Separating the sample into EE and non-EE sub-samples does not reveal a noticeable

[5]The hypothesis that the two distributions are from a same parent sample is statistically rejected if $p < 0.05$. The two samples are believed to have no significant difference if $p > 0.05$.

difference. In Fig. 32c we show the flux distribution of the plateau at the break time. It is shown that the distribution for the EE sub-sample (mean flux $\log F_b = -8.74 \pm 0.12$ ergs s^{-1} cm^{-2}) is systematically higher than that for the non-EE syb-sample (mean flux $\log F_b = -9.84 \pm 0.07$ ergs s^{-1} cm^{-2}). However, the combined sample (Fig.32d) shows a single-component log-normal distribution with a mean flux $\log F_b = -9.34 \pm 0.07$ ergs s^{-1} cm^{-2}, with a student's t-test probability $p = 0.76$ of belonging to the same parent sample. This suggests that the EE GRBs are simply the ones with brighter plateaus, and the detection of EE is an instrumental selection effect. We also calculate the luminosity of the internal plateau at the break time for both the GRBs with and without EE. If no redshift is measured, we adopt z =0.58, the center value for the measured redshift distribution (Fig.32b). We find that the plateau luminosity of the EE ($\log L_0 = 49.41 \pm 0.07$ ergs s^{-1}) is systematically higher than the no-EE sample ($\log L_0 = 48.68 \pm 0.04$ ergs s^{-1}), see Figure 32e. However, the joint sample is again consistent with a single component ($\log L_0 = 48.91 \pm 0.07$ ergs s^{-1}, Fig.32f), with a student's t-test probability $p = 0.74$. For the samples with the measured redshifts only, our results (shown in the inset of Fig.32(e) and 32(f)), the results are similar.

The distributions of the plateau duration, flux and luminosity suggest that the EE and X-ray internal plateaus are intrinsically the same phenomenon. The different plateau luminosity distribution along with the similar plateau duration distribution suggest that the fraction of short GRBs with EE should increase with softer, more sensitive detectors. *The so-called "extended emission" detected in the BAT band is simply the internal plateau emission when the emission is bright and hard enough.*

The host offset and local environment of Internal and External samples

One curious question is why most (22) short GRBs have an internal plateau, whereas some others (10) show an external plateau. One naive expectation is that

the External sample may have a higher circumburst density than the Internal sample, so that the external shock emission is greatly enhanced. It has been found that short GRBs typically have a large offset from their host galaxies (Fong et al. 2010; Fong & Berger 2013; Berger 2014), so that the local interstellar medium (ISM) density may be much lower than that of long GRBs (e.g. Fan et al. 2005; Zhang et al. 2009; Kann et al. 2011). This is likely due to the asymmetric kicks during the supernova explosions of the binary systems when the two compact objects (NS or BH) were born (e.g. Bloom et al. 1999, 2002). If the circumburst density is the key factor to make a difference between the Internal and External samples, one would expect that the offset from the host galaxy is systematically smaller for the External sample than the Internal sample.

With the data collected from the literature (Fong et al 2010, Leibler & Berger 2010, Fong & Berger 2013, Berger 2014), we examine the environmental effect of short GRBs within the Internal and the External samples. The masses, ages and specific star formation rates of the host galaxies do not show statistical differences between the two samples. The physical offsets and the normalized offsets[6] of these two samples are shown in the left and right panels of Figure 33. It appears that the objects in the External sample tends to have smaller offsets than the Internal sample, both for the physical and normalized offsets. This is consistent with above theoretical expectation. Nonetheless, the two samples are not well separated in the offset distributions. Some GRBs in the External sample still have a large offset. This may suggest a large local density in the ISM or intergalactic medium (IGM) far away from the galactic center, or that some internal emission of the nascent magnetars may have observational signatures similar to the external shock emission.

[6]The normalized offsets are defined as the physical offsets normalized to r_e, the characteristic size of a galaxy defined by Eq.(1) of Fong et al. (2010).

Energetics and luminosity

Similar to Lü & Zhang (2014), we derive the isotropic γ-ray energy ($E_{\gamma,\rm iso}$) and isotropic afterglow kinetic energy ($E_{\rm K,iso}$) of all the short GRBs in our sample. To calculate $E_{\gamma,\rm iso}$, we use the observed fluence in the detector's energy band, and extrapolate it to the rest-frame $1-10^4$ keV using spectral parameters with $k-$correction (for details, see Lü & Zhang, 2014). If no redshift is measured, we use z =0.58 (see Table 4).

To calculate $E_{\rm K,iso}$, we apply the method described in Zhang et al. (2007a). Since no stellar wind environment is expected for short GRBs, we apply a constant density model. One important step is to identify the external shock component. If an external plateau is identified, it is straightforward to use the afterglow flux to derive $E_{\rm K,iso}$. The derived $E_{\rm K,iso}$ is a constant during the normal decay phase, but depends on time during the shallow decay phase (Zhang et al. 2007a). We therefore use the flux in the normal decay phase to calculate $E_{\rm K,iso}$. For the Non sample, no plateau is derived, and we use any epoch during the normal decay phase to derive $E_{\rm K,iso}$. For GRBs in the Internal sample, there are two possibilities: (1) In some cases, a normal decay phase is detected after the internal plateau, e.g. GRBs 050724, 062006, 070724A, 071227, 101219A, and 111121A in Fig.29. For these bursts, we use the flux at the first data point during the normal decay phase to derive $E_{\rm K,iso}$. (2) For those bursts whose normal decay segment is not observed after the rapid decay of the internal plateau at later times (the rest of GRBs in Fig.29), we use the last data point to place an upper limit to the underlying afterglow flux. An upper limit $E_{\rm K,iso}$ is then derived.

We adopt two typical values of the circumburst density to calculate the afterglow flux, $n = 1$ cm^{-3} (a typical density of the ISM inside a galaxy) and $n = 10^{-3}$ cm^{-3} (a typical density in the ISM/IGM with a large offset from the galaxy center). For the late epochs we are discussing, fast cooling is theoretically disfavored, and we stick to

the slow cooling ($\nu_m < \nu_c$) regime. Using the spectral and temporal information of the X-ray data, we can diagnose the spectral regime of the afterglow based on the closure relations (e.g. Zhang & Mészáros 2004; see Gao et al. 2013a for a complete review). Most GRBs belong to the $\nu > \max(\nu_m, \nu_c)$ regime, and we use Eqs.(11) and (10) of Zhang et al. (2007a) to derive $E_{\rm K,iso}$. In some cases, the spectral regime $\nu_m < \nu < \nu_c$ is inferred, and Eq.(13) of Zhang et al. (2007a) is adopted to derive $E_{\rm K,iso}$.

In order to place an upper limit of $E_{\rm K,iso}$ for the Internal sample GRBs without a detected external shock component, one needs to assume the spectral regime and decay slope of the normal decay. To do so, we perform a statistical analysis of the decay slope and spectral index in the normal decay phase using the External and Non samples (Figure 34). Fitting the distributions with a Gaussian distribution, we get the center values of $\alpha_{0,c} = 1.21 \pm 0.04$, $\beta_{X,c} = 0.88 \pm 0.05$. We adopt these values to do the calculations. Since $2\alpha_0 \approx 3\beta_X$ is roughly satisfied, the spectral regime belongs to $\nu_m < \nu < \nu_c$, and again Eq.(13) of Zhang et al. (2007a) is used to derive the upper limit of $E_{\rm K,iso}$.

In our calculations, the microphysics parameters of the shocks are assigned to standard values derived from the observations (e.g. Panaitescu & Kumar 2002; Yost et al. 2003): ϵ_e=0.1 and $\epsilon_B = 0.01$. The Compton parameter is assigned to a typical value $Y = 1$. The calculation results are shown in Table 4.

After obtaining the break time t_b through light curve fitting, we derive the bolometric luminosity at the break time t_b:

$$L_b = 4\pi D_L^2 F_b \cdot k, \tag{4.2}$$

where F_b is the X-ray flux at t_b, and k is the k-correction factor. For the Internal sample, we derive the isotropic internal plateau energy, $E_{X,iso}$, using the break time

and break luminosity (Lü & Zhang 2014), i.e.

$$E_{X,iso} \simeq L_b \cdot \frac{t_b}{1+z} \tag{4.3}$$

This energy is also the isotropic emission energy due to internal energy dissipation.

Comparisons of the statistical properties of various derived parameters for the Internal and External samples are presented in Fig.35. Figure 35(a) and (b) show the distributions of the internal plateau luminosity and duration. For the External sample, no internal plateau is detected, we place an upper limit on the internal plateau luminosity using the observed luminosity of the external plateau. The internal plateau luminosity of the Internal sample is $L_b \sim 10^{49}$ ergs s^{-1}. The distribution of the upper limits of L_b of the External sample peaks at a smaller value of $L_b \sim 10^{47.5}$ ergs s^{-1}. This suggests that the distribution of internal plateau luminosity L_b has an intrinsically very broad distribution (Fig.35a). The distribution of the duration of the plateaus for the Internal sample peaks around 100 s, which is systematically smaller than the duration of the plateaus in the External sample, which peaks around $10^{3.3}$ s. In Fig.35(a) and (b), we also compare the plateau luminosity and duration distributions of our sample with those of long GRBs (Dainotti et al. 2015), and find that the Internal sample is quite different with long GRBs, whereas the External sample resembles the distributions of the long GRBs well. According to our interpretation, the duration of the internal plateaus is defined by the collapse time of a supra-massive neutron star (Troja et al. 2007; Zhang 2014). For the external plateaus, the duration of the plateau is related to the minimum of the spin-down time and the collapse time of the magnetar. So by definition, the External sample should have a higher central value of plateau duration than the Internal sample. The observations are consistent with this hypothesis.

Figure 35(c) and (d) show the distribution of $\gamma-$ray energy ($E_{\gamma,iso}$) and the in-

ternal dissipation energy ($E_{X,iso}$). The $E_{\gamma,iso}$ of the Internal sample is a little bit less than that of the External sample, but $E_{X,iso}$ is much larger (for the External sample, only an upper limit of $E_{X,iso}$ can be derived). This means that internal dissipation is a dominated energy release channel for the Internal sample. Figure 35(e) and (f) show the distributions of the blastwave kinetic energy ($E_{K,iso}$) for different values of the number density, $n = 1$ cm^{-3} and $n = 10^{-3}$ cm^{-3}. In both cases, $E_{K,iso}$ of the Internal sample is systematically smaller than the External sample. The results are presented in Tables 4 and 4.

In Fig.35(g) and (h) (for $n = 1, 10^{-3}$ cm^{-3}, respectively), we compare the inferred total energy of GRBs ($E_{\rm total} = E_\gamma + E_{\rm X} + E_{\rm K}$) with the total rotation energy $E_{\rm rot}$ of the millisecond magnetar

$$E_{\rm rot} = \frac{1}{2} I \Omega_0^2 \simeq 3.5 \times 10^{52} \ {\rm erg} \ M_{2.46} R_6^2 P_{0,-3}^{-2}, \tag{4.4}$$

where I is the moment of inertia, R, P_0, and Ω_0 are the radius, initial period, and initial angular frequency of the neutron star, and M is normalized to the sum of the masses of the two NSs ($2.46 M_\odot$) in the observed NS-NS binaries in our Galaxy[7]. Hereafter the convention $Q = 10^x Q_x$ is adopted in cgs units for all the parameters except the mass. It is found that the total energy of the GRBs are below the $E_{\rm rot}$ line if the medium density is high ($n = 1$ cm^{-3}). This energy budget is consistent with the magnetar hypothesis, namely, all the emission energy ultimately comes from the spin energy of the magnetar. For a low-density medium ($n = 10^{-3}$ cm^{-3}), however, a fraction of GRBs in the External sample exceed the total energy budget. The main reason is that a larger $E_{\rm K,iso}$ is needed to compensate a small n in order to achieve a same afterglow flux. If these GRBs are powered by a magnetar, then the data demand a relatively high n. This is consistent with the argument that the External

[7]Strictly speaking, M is normalized to the mean of the sum of masses of binary NS systems, taking into account conservation of rest mass (Lasky et al. 2014), and ignoring the negligible mass lost during the merger process (e.g., Hotokezaka et al. 2013).

sample have a large n so that the external shock component is more dominant.

Figure 36(a) shows the observed X-ray luminosity at $t = 10^3$ s ($L_{t=10^3\mathrm{s}}$) as a function of the decay slope α_2. Figures 36(b) and 36(c) show the respective distributions of $L_{t=10^3 s}$ and α_2. The Internal and External samples are marked in red and black, respectively. On average, the Internal sample have relatively smaller $L_{t=10^3 s}$ than the External sample (Fig.36b). The fitting results of the distributions of various parameters are collected in Table 4.

The millisecond magnetar central engine model and implications

In this section, we place the short GRB data within the framework of the millisecond magnetar central engine model and derive relevant model parameters of the magnetar, and discuss the physical implications of these results.

The millisecond magnetar central engine model

We first briefly review the millisecond magnetar central engine model of short GRBs. After the coalescence of the binary NSs, the evolutionary path of the central post-merger product depends on the unknown equation of state of the neutron stars and the mass of the proto-magnetar, M_{p}. If M_{p} is smaller than the non-rotating Tolman-Oppenheimer-Volkoff maximum mass M_{TOV}, the magnetar will be stable in equilibrium state (Cook et al. 1994; Giacomazzo & Perna 2013, Ravi & Lasky 2014). If M_{p} is only slightly larger than M_{TOV}, it may survive to form a supra-massive neutron star (e.g. Duez et al. 2006), which would be supported by centrifugal force for an extended period of time, until the star is spun down enough so that centrifugal force can no longer support the star. At this epoch, the neutron star would collapse into a black hole.

Before the supra-massive neutron star collapses, it would spin down due to various torques, the most dominant one may be the magnetic dipole spin down (Zhang

& Mészáros 2001)[8]. The characteristic spindown time scale τ and characteristic spindown luminosity L_0 depend on $\Omega_0 = 2\pi/P_0$ and the surface magnetic field at the pole B_p, which read (Zhang & Mészáros 2001)

$$\begin{aligned} \tau &= \frac{3c^3 I}{B_p^2 R^6 \Omega_0^2} = \frac{3c^3 I P_0^2}{4\pi^2 B_p^2 R^6} \\ &= 2.05 \times 10^3 \text{ s } (I_{45} B_{p,15}^{-2} P_{0,-3}^2 R_6^{-6}), \end{aligned} \tag{4.5}$$

$$L_0 = \frac{I\Omega_0^2}{2\tau} = 1.0 \times 10^{49} \text{ erg s}^{-1} (B_{p,15}^2 P_{0,-3}^{-4} R_6^6). \tag{4.6}$$

For a millisecond magnetar, the open field line region opens a very wide solid angle, so that the magnetar wind can be approximated as roughly isotropic.

Another relevant time scale is the collapse time of a supra-massive magnetar, t_{col}. For the Internal sample, the observed break time t_b either corresponds to t_{col} or τ, depending on the post-break decay slope α_2. If $\alpha_2 \simeq 2$, the post-break decay is consistent with a dipole spindown model, so that t_b is defined by τ, and one has $t_{col} > \tau$. On the other hand, if the post-decay slope is steeper than 3, i.e. $\alpha_2 > 3$, one needs to invoke an abrupt cessation of the GRB central engine to interpret the data (Troja et al. 2007; Rowlinson et al. 2010, 2013; Zhang 2014). The break time is then defined by the collapse time t_{col}, and one has $t_{col} \leq \tau$. Overall, one can write

$$\tau \begin{cases} = t_{\rm b}/(1+z), & \alpha_2 = 2, \\ \geq t_{\rm b}/(1+z), & \alpha_2 > 3. \end{cases} \tag{4.7}$$

[8]Deviations from the simple dipole spindown formula may be expected (e.g. Metzger et al. 2011; Siegel et al. 2014), but the dipole formula may give a reasonable first-order approximation of the spindown law of the nascent magnetar.

and

$$t_{col} \begin{cases} > t_{\rm b}/(1+z), & \alpha_2 = 2, \\ = t_{\rm b}/(1+z), & \alpha_2 > 3. \end{cases} \tag{4.8}$$

In both cases, the characteristic spin-down luminosity is essentially the plateau luminosity, which may be estimated as

$$L_0 \simeq L_{\rm b} \tag{4.9}$$

Magnetar parameters and correlations

With the above model, one can derive magnetar parameters and perform their statistics. Two important magnetar parameters to define magnetar spindown, i.e. the initial spin period P_0 and the surface polar cap magnetic field $B_{\rm p}$, can be solved from the characteristic plateau luminosity L_0 (Eq.(4.6)) and the spin-down time scale τ (Eq.(4.5)) (Zhang & Mészáros 2001), i.e.

$$B_{\rm p,15} = 2.05 \text{ G} (I_{45} R_6^{-3} L_{0,49}^{-1/2} \tau_3^{-1}), \tag{4.10}$$

$$P_{0,-3} = 1.42 \text{ s } (I_{45}^{1/2} L_{0,49}^{-1/2} \tau_3^{-1/2}). \tag{4.11}$$

Since the magnetar wind is likely isotropic for short GRBs (in contrast to long GRBs, Lü & Zhang 2014), measured L_0 and τ can be directly used to derive these two parameters. For the Internal sample, both P_0 and $B_{\rm p}$ can be derived if $\alpha_2 = 2$. If $\alpha_2 > 3$, we can derive the upper limit for P_0 and $B_{\rm p}$. The results are presented in Table 4 and Figure 37a[9].

[9]The derived magnetar parameters of most GRBs are slightly different from those derived by Rowlinson et al. (2013). One main discrepancy is that they used $M_p = 1.4 M_\odot$ to calculate the protomagnetar's moment of inertia I, wheareas we used $M_p = 2.46 M_\odot$, which is more relevant for

Figure 37b show the distribution of the collapse times for our Internal sample. For GRB 061201 and GRB 070714B, the decay slope following the plateau is $\alpha_2 \sim 2$, which means that we never see the collapsing feature. A lower limit of the collapse time can be set by the last observational time, so that the stars should be stable long-lived magnetars. For the collapsing sample, the center value of the t_{col} distribution is ~ 100 s, but the half width spans for about one order of magnitude.

Figure 38a presents an anti-correlation between L_0 and $t_{\rm col}$, i.e.

$$\log L_{0,49} = (-2.79 \pm 0.39) \log t_{col,2} - (0.45 \pm 0.28) \tag{4.12}$$

with $r = 0.87$ and $p < 0.0001$. This suggests that a longer collapse times tends to have a lower plateau luminosity. It is consistent with the expectation of the magnetar central engine model: The total spin energy of the millisecond magnetars may be roughly standard. A stronger dipole magnetic field tends to power a brighter plateau, making the magnetar spin down more quickly, and therefore giving rise to a shorter collapse time (see also Rowlinson et al. 2014).

Figure 38b presents an anti-correlation between $E_{\rm total,iso}$ and t_{col}.

$$\log E_{\rm total,iso,52} = (-1.08 \pm 0.27) \log t_{\rm col,2} + (0.11 \pm 0.18) \tag{4.13}$$

with $r = 0.71$ and $p = 0.0009$. This may be understood as the following: A higher plateau luminosity corresponds to a shorter spin-down time scale. It is possible that in this case the collapse time is closer to the spin-down time scale, so that, most energy is already released before the magnetar collapses to form a black hole. A lower plateau

post-merger products. The different data selection criteria and fitting methods also contribute to the discrepancies between the two pieces of work.

luminosity corresponds to a longer spin-down time scale, and it is possible that the collapse time can be much shorter than the spin-down time scale, so that only a fraction of the total energy is released before the collapse.

Empirically, Dainotti et al. (2008, 2010, 2013) discovered an anti-correlation between L_b and t_b for long GRBs. In Figure 38c we plot our short GRB Internal + External sample and derive an empirical correlation

$$\log L_{b,49} = (-1.41 \pm 0.14) \log t_{b,3} - (0.46 \pm 0.37), \tag{4.14}$$

with $r = 0.88$ and $p < 0.001$. The slope of the correlation is slightly steeper than that of the "Dainotti relation" (e.g. Dainotti et al. 2008, data see grey dots in Fig.38(c). This is probably related to different progenitor systems for long and short GRBs, in particular, the dominance of Internal plateaus in our sample. Rowlinson et al. (2014) performed a joint analysis of both long and short GRBs taking into account for the intrinsic slope of the luminosity - time correlation (Dainotti et al. 2013). We focus on short GRBs only but studied the Internal and External sub-samples separately[10].

Constrain the neutron star EoS

The inferred collapsing time can be used to constrain neutron star equation of state (Lasky et al. 2014; Ravi & Lasky 2014). The basic formalism is as follows.

The standard dipole spin-down formula gives (Shapiro & Teukolsky 1983)

$$\begin{aligned} P(t) &= P_0(1 + \frac{4\pi^2}{3c^3}\frac{B_p^2 R^6}{I P_0^2} t)^{1/2} \\ &= P_0(1 + \frac{t}{\tau})^{1/2}. \end{aligned} \tag{4.15}$$

[10]We here do not take into account of the luminosity and time evolutions related to our observable, since the paucity of the sample in short GRBs would prevent us from a reliable statistical analysis. We are also aware that future analysis of the selection effects in the correlation presented here may change the current interpretation of the models, only if these changes in the intrinsic correlation are greater than 5 sigma, for reference to this issue see Dainotti et al. (2013b).

For a given EoS, a maximum NS mass for a non-rotating NS, i.e. $M_{\rm TOV}$, can be derived. When a NS is supra-massive but rapidly rotating, a higher mass can be sustained. The maximun gravitational mass ($M_{\rm max}$) depends on spin period, which can be approximated as (Lyford et al. 2003)

$$M_{\rm max} = M_{\rm TOV}(1 + \hat{\alpha}P^{\hat{\beta}}) \tag{4.16}$$

where $\hat{\alpha}$ and $\hat{\beta}$ depend on the EoS. The numerical values of $\hat{\alpha}$ and $\hat{\beta}$ for various EoSs have been worked out by Lasky et al. (2014), which are presented in Table 4 along with $M_{\rm TOV}$, R, and I.

As the neutron star spins down, the maximum mass $M_{\rm max}$ gradually decreases. When $M_{\rm max}$ becomes equal to the total gravitational mass of the proto-magnetar, M_p, the centrifugal force can no longer sustain the star, so that the NS will collapse into a black hole. Using equation Eq.(4.15) and Eq.(4.16), one can derive the collapse time

$$\begin{aligned} t_{\rm col} &= \frac{3c^3 I}{4\pi^2 B_{\rm p}^2 R^6}[(\frac{M_{\rm p} - M_{\rm TOV}}{\hat{\alpha} M_{\rm TOV}})^{2/\hat{\beta}} - P_0^2] \\ &= \frac{\tau}{P_0^2}[(\frac{M_{\rm p} - M_{\rm TOV}}{\hat{\alpha} M_{\rm TOV}})^{2/\hat{\beta}} - P_0^2]. \end{aligned} \tag{4.17}$$

As noted, one can infer B_p, P_0 and t_{col} from the observations. Moreover, as the Galactic binary NS population has a tight mass distribution (e.g., Valentim et al. 2011; Kiziltan et al. 2013), one can infer the expected distribution of protomagnetar masses, which is found to be $M_p = 2.46^{0.13}_{-0.15} M_\odot$ (for details see Lasky et al. 2014). The only remaining variables in equation (16) are related to the EoS, implying that the observations can be used to derive constraints on the EoS of nuclear matter. For most GRBs in our Internal sample, only the lower limit of τ is derived from t_b (Eq.(4.7)). One can also infer the maximum τ by limiting P_0 to the break-up limit.

Considering the uncertainties related to gravitational wave radiation, we take a rough limit of 1 millisecond. By doing so, one can then derive a range of τ, and hence, a range of M_p based on the data and a given EoS.

Figure 39 presents the collapse time ($t_{\rm col}$) as a function of protomagnetar mass (M_p) for each short GRB in the Internal sample that have redshift measurements. Five NS equations of state, i.e. SLy (black, Douchin & Haensel. 2001), APR (red, Akmal et al. 1998), GM1 (green, Glendenning & Moszkowski. 1991), AB-N and AB-L (blue and cyan, Arnett & Bowers. 1997) are shown in different vertical color bands. The gray shaded region is the protomagnetar mass distribution, M_p, discussed above. The horizontal dashed line is the observed collapse time for each short GRB. Our results show that the GM1 model gives a M_p band fall in the 2σ region of the protomagnetar mass distribution, so that the correct EoS should be close to this model. The maximum mass for non-rotating NS in this model is $M_{\rm TOV} = 2.37 M_\odot$.

Lasky et al. (2014) applied the observational collapse time of short GRBs to constrain NS EoS (see also a rough treatment by Fan et al. 2013a). Our results are consistent with Lasky et al. (2014) using a larger sample. Another improvement is that we introduce a range of τ rather than one single τ to derive the range of plausible M_p, since the observed collapse time only gives the lower limit of τ. This gives a range of the allowed M_p (rather than a fine-tuned value for the single τ scenario) for each GRB for a given observed t_b.

Conclusions and Discussion

In this paper, by systematically analyzing the BAT-XRT light curves of short GRBs detected by *Swift* before 2014 August, we systematically examine the millisecond magnetar central engine model of short GRBs. About 40 GRBs have bright X-ray afterglows detected with *Swift*/XRT, among which 8 have the extended emission detected with *Swift*/BAT. Based to the existence of plateaus, their observation

properties, and how likely a GRB is powered by a millisecond magnetar central engine, we characterized short GRBs into three samples: Internal (plateau), External (plateau), and Non (plateau). We compared the statistical properties of our samples, and derived or placed limits on the magnetar parameters P_0 and B_p from the data. Using the collapse time t_{col} of the protomagnetar inferred from the plateau break time t_b in the Internal sample, we went on to constrain the NS EoS. Following interesting results are obtained:

- At least for the Internal sample, the data seem to be consistent with the expectations of the magnetar central engine model. Assuming isotropic emission, the derived magnetar parameters B_p and P_0 fall into the reasonable range. The total energy (sum of E_γ, $E_{\rm X}$ and $E_{\rm K}$) is within the budget provided by the spin energy of the millisecond magnetar ($E_{\rm rot} \sim 3.5 \times 10^{52}$ erg). The $L_0 - t_{col}$ anti-correlation is generally consistent with the hypothesis that the total spin energy of the magnetar may be standard, and a higher dipolar magnetic field powers a brighter but shorter plateau.

- The so-called extended emission following some short GRBs is essentially the brightest internal plateau commonly observed in short GRBs. A more sensitive and softer detector would detect more extended emission from short GRBs.

- The External sample may be also consistent with having a magnetar central engine, even though the evidence is not as strong. If both the Internal and External samples are powered by a millisecond magnetar central engine, the difference between the two samples may be related to the circumburst medium density. The physical and host-normalized offsets of the afterglow locations for the Internal sample is somewhat larger than those of the External sample, even though the separation between the two samples is not clear cut. In any case, it is consistent with this expectation. The total energy budget of the GRB is

within the magnetar energy budget for the External sample, only if the ambient density is relatively large, and hence, powers a strong external shock emission component. There is no significant difference between those two groups for the star formation rate, metallicity and age of the host galaxy.

- Using the collapse time of supra-massive protomagnetar to form a black hole and the distribution of the total mass of NS-NS binaries in the Galaxy, one can constrain the NS EoS. The data point towards a EoS model close to GM1, which has a non-spinning maximum NS mass $M_{\rm TOV} \sim 2.37 M_{\odot}$.

The short GRB data are consistent with the hypothesis that the post-merger product of NS-NS mergers is a supra-massive neutron star. The existence of such a long-lived post-merger product opens some interesting prospects in the multi-messenger era. In particular, the dipole spindown power of the supra-massive NS can power bright electromagnetic radiation even if the short GRB jet does not beam towards earth, so that some interesting observational signatures are expected to be associated with gravitational wave signals in the Advanced LIGO/Virgo era (Zhang 2013; Gao et al. 2013; Yu et al. 2013; Fan et al. 2013b; Metzger & Piro 2014). Another interesting possibility is that a fast radio burst (e.g. Lorimer et al. 2007; Thornton et al. 2013) may be released when the supra-massive magnetar collapses into a black hole (Zhang 2014; Falcke & Rezzolla 2014). A discovery of an FRB following a GRB at the end of the internal plateau (cf. Bannister et al. 2012) would nail down the origin of FRBs, although such observations require fast telescope response times given the expected distribution of collapse times following SGRBs (see figure 37b and Ravi & Lasky 2014). The GRB-FRB associations, if proven true, would be invaluable for cosmology studies (Deng & Zhang 2014; Gao et al. 2014; Zhou et al. 2014; Zheng et al. 2014).

Recently, Rezzolla & Kumar (2014) and Ciolfi & Siegel (2014) proposed a different model to interpret the short GRB phenomenology. In their model, the post-merger

product is also a supra-massive NS, but the collapse time is allocated as the epoch of the short GRB itself, rather than the end of the Internal plateau. Our conclusions drawn in this paper do not apply to that model. A crucial observational test to differentiate between our model and theirs is whether or not there exists strong X-ray emission before the short GRB itself. This may be tested in the future with a sensitive wide-field X-ray telescope.

(a): The measured redshift are from the published papers and GNCs. When the redshift is not known, 0.58 is used. (b): The duration (s) of the GRB without and with extended emission (if EE exists). "N" denotes no EE. (c): The photon index in the BAT band (15-150keV) fitted using a power-law. (d): The spectral index of the absorbed power-law model for the normal segments. (e): Physical and host-normalized offsets for the short GRBs with *Hubble Space Telescope (HST)* observations. (REFERENCES):1: Zhang et al. (2009); 2: Fong, Berger & Fox.(2010); 3: Hullinger et al.(2005); 4: Butler et al.(2007); 5: Gompertz, O'Brien & Wynn.(2014); 6: Fong & Berger (2013); 7: Rowlinson et al.(2013); 8: Fong et al.(2011); 9: Fong et al.(2013); 10: Lü & Zhang.(2014); 11: Thoene et al.(2010); 12: Markwardt et al.(2010); 13: Cucchiara et al.(2013); 14: Barthelmy et al.(2013); 15: Krimm et al.(2013).

GRB name	z (a)	T_{90}/EE (b)	Γ_γ (c)	β_X (d)	Host offset (e)	Host offset (e)	Reference
Internal							
050724	0.2576	3/154	1.89±0.22	0.58±0.19	2.76±0.024	—	(1,2)
051210	(0.58)	1.27/40	1.06±0.28	1.1±0.18	24.9±24.6	4.65±4.6	(1,2)
051227	(0.58)	3.5/110	1.45±0.24	1.1±0.4	—	—	(3,4,5)
060801	1.13	0.49/N	1.27±0.16	0.43±0.12	—	—	(1)
061006	0.4377	0.5/120	1.72±0.17	0.76±0.28	1.3±0.24	0.35±0.07	(1,2)
061201	0.111	0.76/N	0.81±0.15	1.2±0.22	32.47±0.06	14.91±0.03	(1,6)
070714B	0.9224	3/100	1.36±0.19	1.01±0.16	12.21±0.53	5.55±0.24	(1,6)
070724A	0.46	0.4/N	1.81±0.33	0.5±0.3	5.46±0.14	1.5±0.04	(1,6)
071227	0.381	1.8/100	0.99±0.22	0.8±0.3	15.5±0.24	3.28±0.05	(1,6)
080702A	(0.58)	0.5/N	1.34±0.42	1.03±0.35	—	—	(7)
080905A	0.122	1/N	0.85±0.24	0.45±0.14	17.96±0.19	10.36±0.1	(6,7)
080919	(0.58)	0.6/N	1.11±0.26	1.09±0.36	—	—	(7)
081024A	(0.58)	1.8/N	1.23±0.21	0.85±0.3	—	—	(7)
090510	0.903	0.3/N	0.98±0.21	0.75±0.12	10.37±2.89	1.99±0.39	(6,7)
090515	(0.58)	0.036/N	1.61±0.22	0.75±0.12	75.03±0.15	15.53±0.03	(6,7)
100117A	0.92	0.3/N	0.88±0.22	1.1±0.26	1.32±0.33	0.57±0.13	(6,7,8)
100625A	0.425	0.33/N	0.91±0.11	1.3±0.3	—	—	(7,9)
100702A	(0.58)	0.16/N	1.54±0.15	0.88±0.11	—	—	(7)
101219A	0.718	0.6/N	0.63±0.09	0.53±0.26	—	—	(7)
111121A	(0.58)	0.47/119	1.66±0.12	0.75±0.2	—	—	(7)
120305A	(0.58)	0.1/N	1.05±0.09	1.4±0.3	—	—	(7)
120521A	(0.58)	0.45/N	0.98±0.22	0.73±0.19	—	—	(7)
External							
051221A	0.55	1.4/N	1.39±0.06	1.07±0.13	1.92±0.18	0.88±0.08	(1,2,7)
060313	(0.58)	0.71/N	0.71±0.07	1.06±0.15	2.28±0.5	1.23±0.23	(1,2,7)
060614	0.1254	5/106	2.02±0.04	1.18±0.09	—	—	(1,10)
070714A	(0.58)	2/N	2.6±0.2	1.1±0.3	—	—	(7)
070809	0.219	1.3/N	1.69±0.22	0.37±0.21	33.22±2.71	9.25±0.75	(6,7)
080426	(0.58)	1.7/N	1.98±0.13	0.92±0.24	—	—	(7)
090426	2.6	1.2/N	1.93±0.22	1.04±0.15	0.45±0.25	0.29±0.14	(6,7)
100724A	1.288	1.4/N	1.92±0.21	0.94±0.23	—	—	(11,12)
130603B	0.356	0.18/N	1.83±0.12	1.18±0.18	5.21±0.17	1.05±0.04	(6,13,14)
130912A	(0.58)	0.28/N	1.21±0.2	0.56±0.11	—	—	(15)

Table 6 Observed properties of short GRBs in our samples

(f): The break time (s) of the lightcurves from our fitting, α_1 and α_2 are the decay slopes before and after the break time.

GRB name	t_b (f)	α_1 (f)	α_2 (f)	χ^2/dof
Internal				
050724	139±9	0.20±0.1	4.16±0.05	980/835
051210	67±4	0.15±0.04	2.96±0.09	118/132
051227	89±5	0.10±0.05	3.19±0.13	681/522
060801	212±11	0.10±0.11	4.35±0.26	81/75
061006	99±7	0.17±0.03	9.45±1.14	111/138
061201	2223±43	0.54±0.06	1.84±0.08	20/24
070714B	82±2	0.10±0.07	1.91±0.03	672/581
070724A	77±6	0.01±0.1	6.45±0.46	256/222
071227	69±8	0.27±0.08	2.92±0.06	244/212
080702A	586±14	0.51±0.22	3.56±0.31	3/5
080905A	13±3	0.19±0.09	2.37±0.07	43/52
080919	340±26	0.40±0.14	5.20±0.55	7/5
081024A	102±5	0.27±0.02	5.89±0.3	50/42
090510	1494±87	0.69±0.04	2.33±0.11	112/132
090515	178±3	0.10±0.08	12.62±0.5	42/38
100117A	252±9	0.55±0.03	4.59±0.13	84/92
100625A	200±41	0.26±0.44	2.47±0.18	3/6
100702A	201±6	0.62±0.13	5.28±0.23	82/69
101219A	197±10	0.13±0.19	20.52±8.01	3/5
111121A	56±9	0.10±0.13	2.26±0.04	274/289
120305A	188±14	0.73±0.14	6.49±0.63	14/18
120521A 270±55	0.30±0.27	10.74±4.76	3/7	
External				
051221A	25166±870	0.12±0.13	1.43±0.04	52/63
060313	2294±65	0.3±0.15	1.52±0.04	54/45
060614	49840±3620	0.18±0.06	1.9±0.07	70/54
070714A	892±34	0.11±0.09	0.95±0.06	15/18
070809	8272±221	0.18±0.06	1.31±0.17	17/22
080426	566±97	0.11±0.16	1.29±0.05	28/21
090426	208±53	0.12±0.07	1.04±0.04	15/11
100724A	5377±331	0.72±0.08	1.61±0.12	16/19
130603B	3108±356	0.4±0.02	1.69±0.04	126/109
130912A	231±54	0.04±0.39	1.34±0.04	28/21

Table 7 Fitting results of short GRBs in our samples

(a): $E_{\gamma,\rm iso}$ is calculated using fluence and redshift extrapolated into 1-10000 keV (rest frame) with a spectral model and a k-correction, in units of 10^{51} erg. (b): Isotropic luminosity at the break time (in units of 10^{49} erg s^{-1}), and the spin-down time (in units of 10^3s). (c): The dipolar magnetic field strength at the polar cap in units of $10^{15}G$, and the initial spin period of the magnetar in units of milliseconds, with an assumption of an isotropic wind.

GRB name	$E_{\gamma,\rm iso,51}$ (a)	$L_{b,49}$ (b)	τ_3 (b)	$B_{p,15}$ (c)	$P_{0,-3}$ (c)
Internal					
050724	$0.09^{+0.11}_{-0.02}$	1.1±0.16	0.11↑	17.15↓	4.04↓
051210	$0.22^{+0.036}_{-0.036}$	2.23±0.26	0.04↑	32.69↓	4.68↓
051227	$1.20^{+1.6}_{-0.5}$	1.89±0.02	0.05↑	28.68↓	4.57↓
060801	$1.70^{+0.2}_{-0.2}$	0.73±0.07	0.14↑	17.81↓	4.57↓
061006	$2.20^{+1.2}_{-1.2}$	3.37±0.32	0.04↑	18.31↓	3.16↓
061201	$0.18^{+0.02}_{-0.01}$	(1±0.11)E-3	2±0.043	31.17±2.36	30.80±1.97
070714B	$11.60^{+4.1}_{-2.2}$	6.22±0.09	0.04±0.002	19.12±1.08	2.77±0.09
070724A	$0.03^{+0.01}_{-0.01}$	13.1±7.2	0.05↑	10.89↓	1.73↓
071227	$2.20^{+0.8}_{-0.8}$	0.77±0.01	0.05↑	44.93↓	7.16↓
080702A	$0.13^{+0.208}_{-0.0556}$	(7±0.25)E-3	0.37↑	64.41↓	27.40↓
080905A	7^{+11}_{-4}	2.76±0.9	0.01↑	102.83↓	7.87↓
080919	$0.42^{+0.41}_{-0.278}$	0.05±0.01	0.22↑	41.98↓	13.63↓
081024A	$0.56^{+0.69}_{-0.278}$	0.78±0.14	0.06↑	36.34↓	6.42↓
090510	3^{+5}_{-2}	0.18±0.03	0.75↑	6.36↓	3.85↓
090515	$0.08^{+0.16}_{-0.042}$	1.24±0.05	0.11↑	16.29↓	3.82↓
100117A	$2.50^{+0.3}_{-0.3}$	0.45±0.04	0.16↑	19.06↓	5.32↓
100625A	$0.64^{+0.031}_{-0.031}$	0.042±0.03	0.13↑	79.67↓	19.75↓
100702A	$0.47^{+0.045}_{-0.045}$	0.97±0.14	0.13↑	16.36↓	4.07↓
101219A	$4.80^{+0.3}_{-0.3}$	0.56±0.05	0.12↑	23.84↓	5.65↓
111121A	$2.80^{+0.25}_{-0.25}$	14±0.8	0.04↑	15.22↓	2.02↓
120305A	$0.29^{+0.0112}_{-0.0112}$	0.48±0.09	0.13↑	23.30↓	5.80↓
120521A	$0.23^{+0.0115}_{-0.0356}$	0.07±0.003	0.17↑	44.68↓	12.90↓
External					
051221A	$2.80^{+2.1}_{-1.1}$	(1.78±0.09)E-5	—	—	—
060313	$12.90^{+0.889}_{-7.56}$	(2.74±0.21)E-2	—	—	—
060614	$2.40^{+0.4}_{-0.4}$	(2.55±0.12)E-4	—	—	—
070714A	$0.42^{+1.25}_{-0.069}$	(1.3±0.15)E-2	—	—	—
070809	$0.01^{+0.01}_{-0.01}$	(3.2±0.31)E-5	—	—	—
080426	$0.82^{+1.25}_{-0.0556}$	(3.53±1.01)E-2	—	—	—
090426	$4.20^{+5}_{-0.4}$	2.46±0.48	—	—	—
100724A	$0.7^{+0.1}_{-0.1}$	(2.85±0.32)E-2	—	—	—
130603B	$2.20^{+0.2}_{-0.2}$	(1.2±0.05)E-2	—	—	—
130912A	$0.73^{+0.08}_{-0.08}$	0.21±0.09	—	—	—

Table 8 The derived properties of the short GRBs in our samples

(d): The luminosity of the afterglow at $t = 1000$ s. The arrow sign indicates the upper limit. (e): The isotropic kinetic energy measured from the afterglow flux during the normal decay phase with $n = 1cm^{-3}$ and $n = 10^{-3}cm^{-3}$, in units of 10^{51} erg. (e): The isotropic internal dissipation energy in the X-ray band (also internal plateau), in units of 10^{51} erg. (f): The isotropic internal dissipation energy in the X-ray band (also internal plateau), in units of 10^{51} erg.

GRB name	$L_{47}(10^3 s)$ (d)	$E_{K,iso,51}$ (e)	$E_{K,iso,51}$ (e)	$E_{X,iso,51}$ (f)
Internal				
050724	0.05±0.006	0.97±0.13	2.37±0.26	1.25±0.14
051210	0.32↓	0.34↓	1.89↓	0.94±0.10
051227	0.66±0.086	2.69±0.35	5.65±0.26	0.98±0.11
060801	0.46↓	3.84↓	2.03↓	0.98±0.16
061006	0.17±0.022	6.37±0.83	6.37±0.83	2.06±0.23
061201	0.15±0.019	0.74±0.10	1.84±0.21	0.02±0.01
070714B	1.40±0.182	4.40±0.57	9.47±0.41	2.67±0.29
070724A	0.05±0.007	7.99±1.04	7.99±1.04	6.81±4.56
071227	0.05±0.007	0.91±0.12	2.07±0.23	0.40±0.04
080702A	0.02±0.002	0.26↓	0.84↓	0.03±0.01
080905A	0.01↓	0.37↓	0.72↓	0.33±0.18
080919	0.11±0.014	0.20↓	1.01↓	0.11±0.04
081024A	0.41↓	0.50↓	0.95↓	0.50±0.12
090510	7.90±1.027	3.71±0.48	7.79±0.85	1.38±0.37
090515	0.28↓	0.83↓	0.93↓	1.40±0.10
100117A	0.02↓	0.12↓	0.92↓	0.72±0.09
100625A	0.02±0.003	0.07↓	0.11↓	0.05±0.05
100702A	1.20↓	1.82↓	4.04↓	1.24±0.22
101219A	0.23↓	4.14±0.54	10.03±1.11	0.64±0.10
111121A	1.57±0.204	9.80±1.27	22.64±1.49	5.04±0.55
120305A	0.11±0.014	0.45±0.06	0.89±0.10	0.61±0.17
120521A	1.01↓	2.46↓	4.42↓	0.12±0.03
External				
051221A	0.63±0.08	16.29±2.12	35.56±3.91	0.31±0.032
060313	3.00±0.39	8.11±1.05	17.21±1.89	0.45±0.054
060614	0.04±0.01	7.06±0.92	14.56±1.61	0.11±0.012
070714A	0.70±0.09	13.94±1.81	13.94±1.81	0.07±0.013
070809	0.05±0.01	2.25±0.29	5.61±0.62	0.02±0.003
080426	0.83±0.11	4.71±0.61	10.35±1.14	0.13±0.064
090426	12.50±1.63	52.84±6.87	128.09±14.09	1.43±0.690
100724A	5.20±0.68	13.83±1.80	30.42±3.34	0.67±0.180
130603B	1.60±0.21	6.12±0.80	13.46±1.26	0.27±0.055
130912A	1.50±0.20	20.15±2.62	49.53±5.45	0.30±0.237

Table 9 The calculations properties of the short GRBs in our samples

Name	Internal	External
$\log(L_b)$ erg s^{-1}	(49.06 ± 0.15) erg s^{-1}	(47.55 ± 0.16) erg s^{-1}
$log(t_{\rm b})$ s	(2.01 ± 0.06) s	(3.41 ± 0.04) s
$log(E_{\gamma,{\rm iso}})$ erg	(50.78 ± 0.16) erg	(51.25 ± 0.08) erg
$log(E_{\rm X,iso}, n = 1$ cm$^{-3})$ erg	(50.86 ± 0.11) erg	(51.35 ± 0.04) erg
$log(E_{\rm X,iso}, n = 10^{-3}$ cm$^{-3})$ erg	(51.74 ± 0.18) erg	(52.32 ± 0.06) erg
$log(E_{\rm total,iso}, n = 1$ cm$^{-3})$ erg	(51.36 ± 0.06) erg	(51.82 ± 0.04) erg
$log(E_{\rm total,iso}, n = 10^{-3}$ cm$^{-3})$ erg	(51.61 ± 0.07) erg	(52.39 ± 0.03) erg
$log(t_{\rm col})$ s	(1.96 ± 0.02) s	—
$log(L_{\rm t=10^3 s})$ erg s^{-1}	(46.09 ± 0.07) erg s^{-1}	(47.08 ± 0.09) erg s^{-1}

Table 10 The center values and standard deviations of the Gaussian fits of various distributions

	SLy	APR	GM1	AB-N	AB-L
$M_{TOV}(M_\odot)$	2.05	2.20	2.37	2.67	2.71
R(km)	9.99	10.0	12.05	12.9	13.7
$I(10^{45}$ g cm$^2)$	1.91	2.13	3.33	4.30	4.70
$\hat{\alpha}(10^{-10}\ s^{-\hat{\beta}})$	1.60	0.303	1.58	0.112	2.92
$\hat{\beta}$ height					

Table 11 The parameters of various NS EoS models

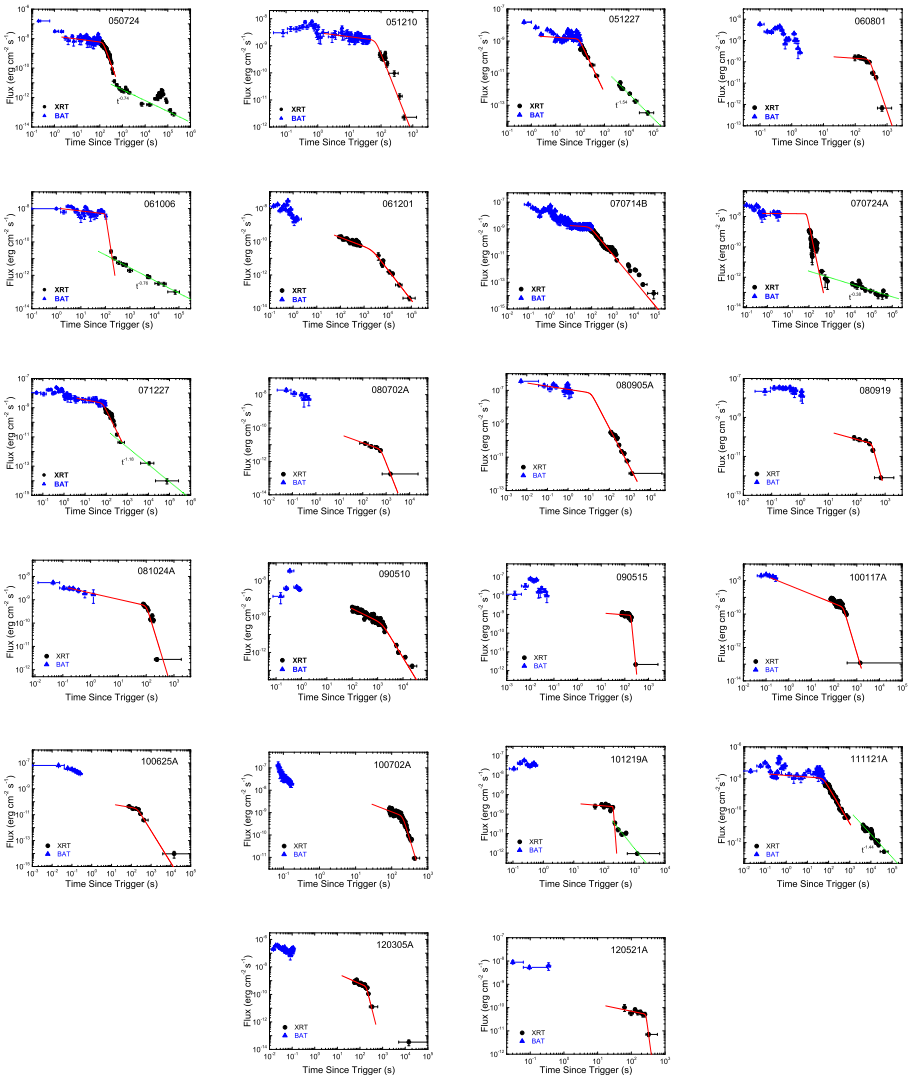

Figure 29 The BAT-XRT rest-frame light curves of the GRBs in our Internal sample. Blue triangle signs are BAT data extrapolated to the XRT band, and black points (with error bars) are the XRT data. The red solid curves are the best fits with a smooth broken power law model to the data. The green dot lines are the best fits with power law model after the steeper decay.

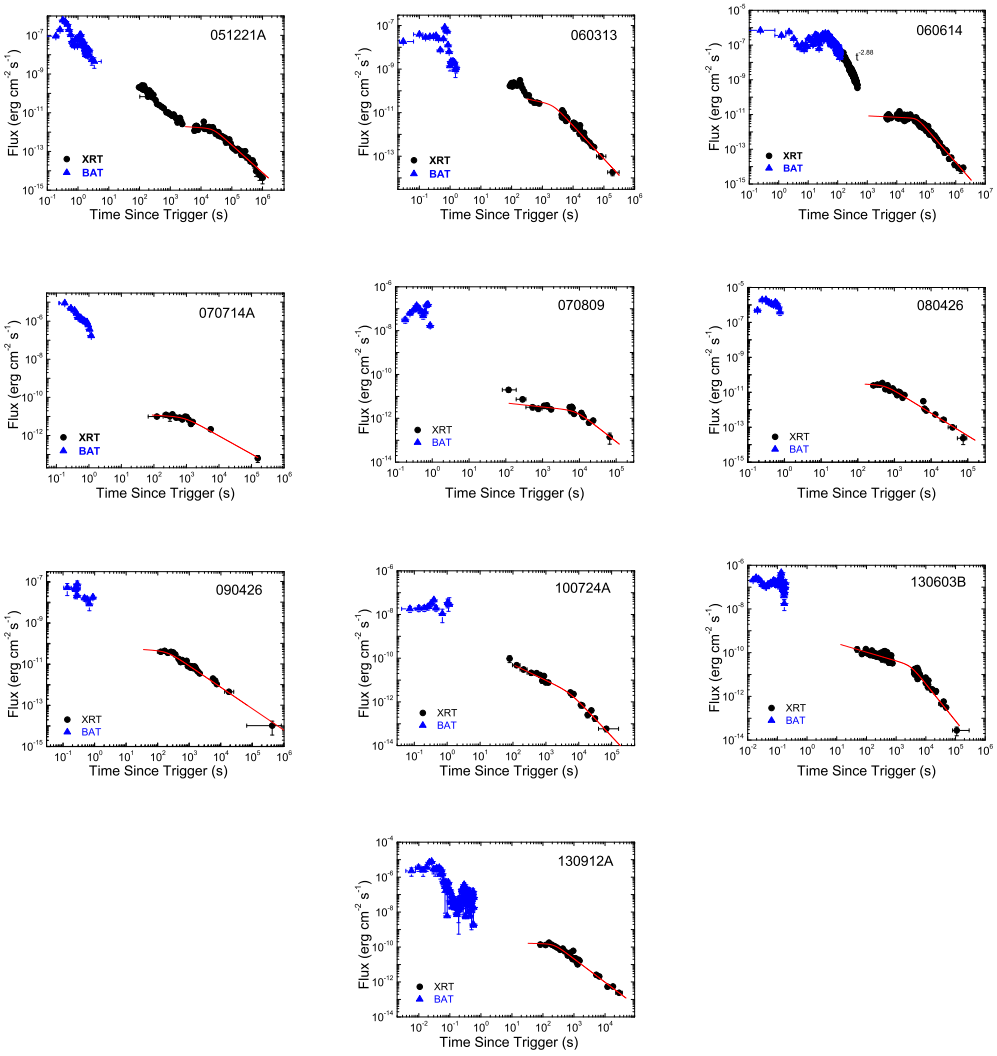

Figure 30 Similar to Fig. 29, but for the External sample.

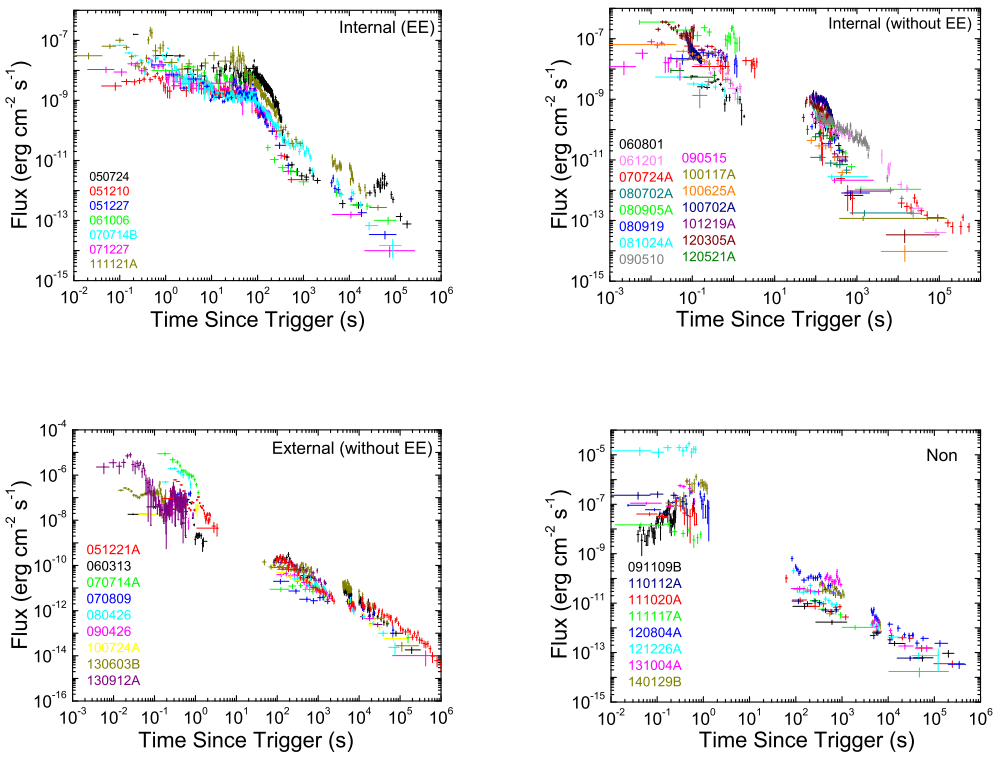

Figure 31 The ensemble of X-ray light curves (0.3-10 keV) of the GRBs in our Internal sample with EE, Internal sample without EE, External sample, and Non sample.

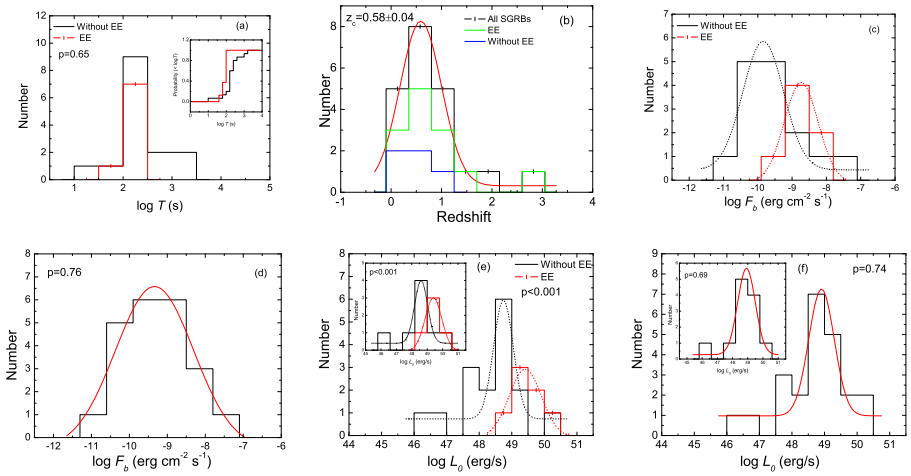

Figure 32 (a): The duration distributions of the extended emission for EE sample, and the internal plateau emission for the no-EE sample. Inset: the cumulative duration distributions for the EE and no-EE sub-samples. (b): The redshift distribution of all short GRBs with z measurements. The red solid line is the best Gaussian fit with a center value $z_c = 0.58$. The green and blue histograms are the redshift distributions for the EE and no-EE sub-samples, respectively. (c): The plateau flux distributions of both EE (red, solid line + bar) and no-EE (black, solid line) GRBs in our Internal sample. The dotted lines are the best Gaussian fits to the distributions. (d): A joint fit to the flux distribution of all the GRBs in the Internal plateau (both EE and no-EE included). (e): The plateau luminosity distributions of both EE (red, solid line + bar) and no-EE (black, solid line) GRBs in our Internal sample. The dotted lines are the best Gaussian fits to the distributions. (f): A joint fit to the luminosity distribution of all the GRBs in the Internal plateau (both EE and no-EE included). The insets in (e) and (f) are for the GRBs with measured redshifts only.

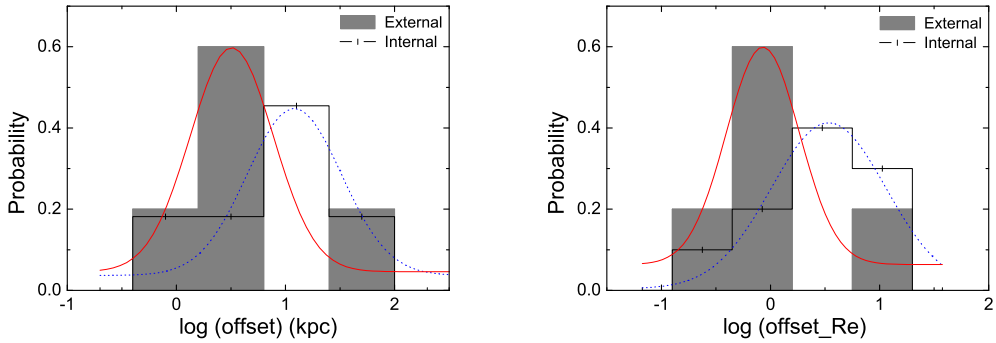

Figure 33 The distributions of the physical offsets and host-normalized offsets of the Internal and External samples. The solid and dash lines are the best Gaussian fitting for Internal and External, respectively.

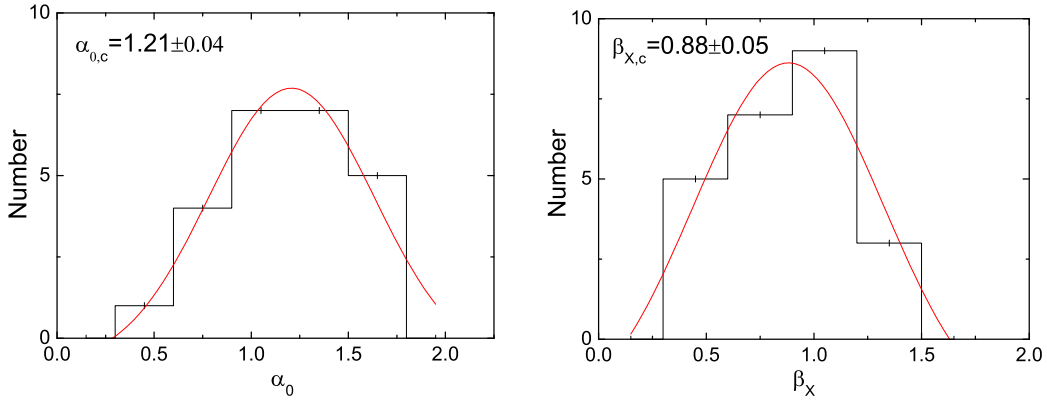

Figure 34 The distributions of decay slope α_0 and spectral index β_X in the normal decay phase in our External and Non samples. The solid lines are the best Gaussian fits to the distributions.

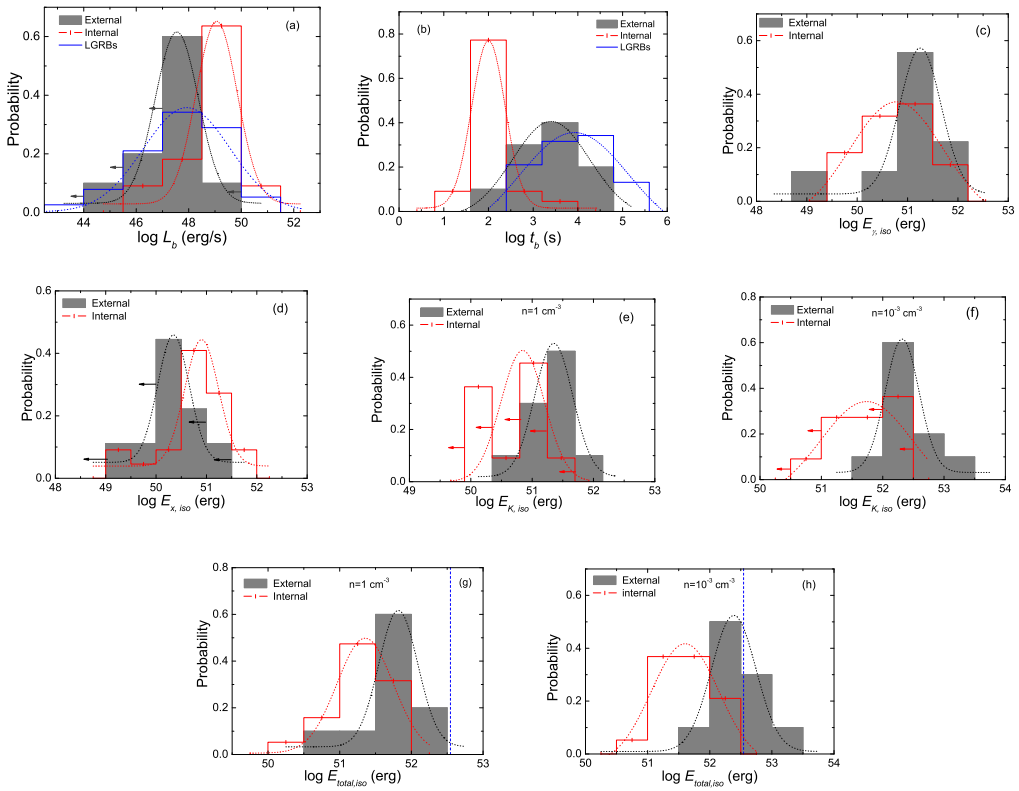

Figure 35 Comparisons of various properties between the Internal (red, open histogram) sample and the External (black, grey histogram) samples. The best-fit Gaussian profiles are over-plotted with the respective colors. The eight panels denote histograms of L_b, t_b, $E_{\gamma,\rm iso}$, $E_{\rm X,iso}$, $E_{\rm K,iso}$ and $E_{\rm total,iso}$, respetively, with the last two parameters plotted twice for two different medium densities, $n = 1, 10^{-3}$ cm^{-3}. The vertical dot line in panels (g) and (h) denotes the total rotation energy budget of a millisecond magnetar. If no redshift is measured, $z = 0.58$ is adopted in the calculations.

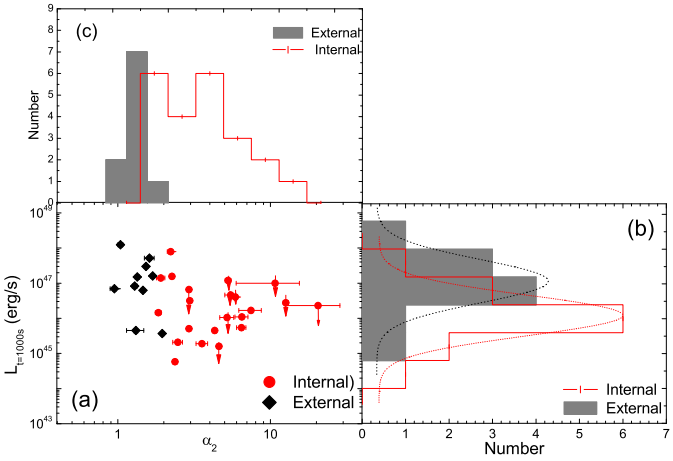

Figure 36 The 1D (panels (b) and (c)) and 2D (panel (a)) $L(t = 1000\ \mathrm{s}) - \alpha_2$ distributions of the GRBs in our samples. The red diamonds and black dots denote the Internal and External samples, respectively, and the arrows indicate the upper limits.

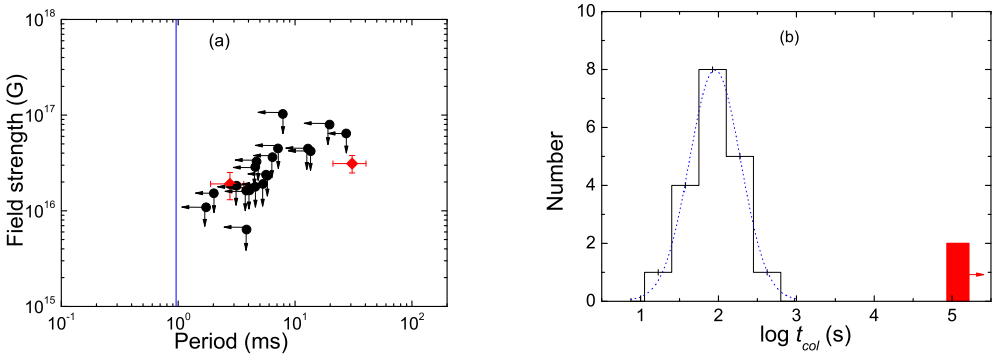

Figure 37 (a): The inferred magnetar parameters, initial spin period P_0 vs. surface polar cap magnetic field strength B_p derived for our Internal sample. The red diamonds indicate GRB 061201 and GRB 070714B, which have τ measured from t_b. All the other GRBs only have the lower limit of τ. The arrows denote upper limits. The vertical solid line is the breakup spin-period limit for a neutron star (Lattimer & Prakash 2004). (b): The distribution of the collapse time for our Internal sample. The dotted line is the best Gaussian profile fit.

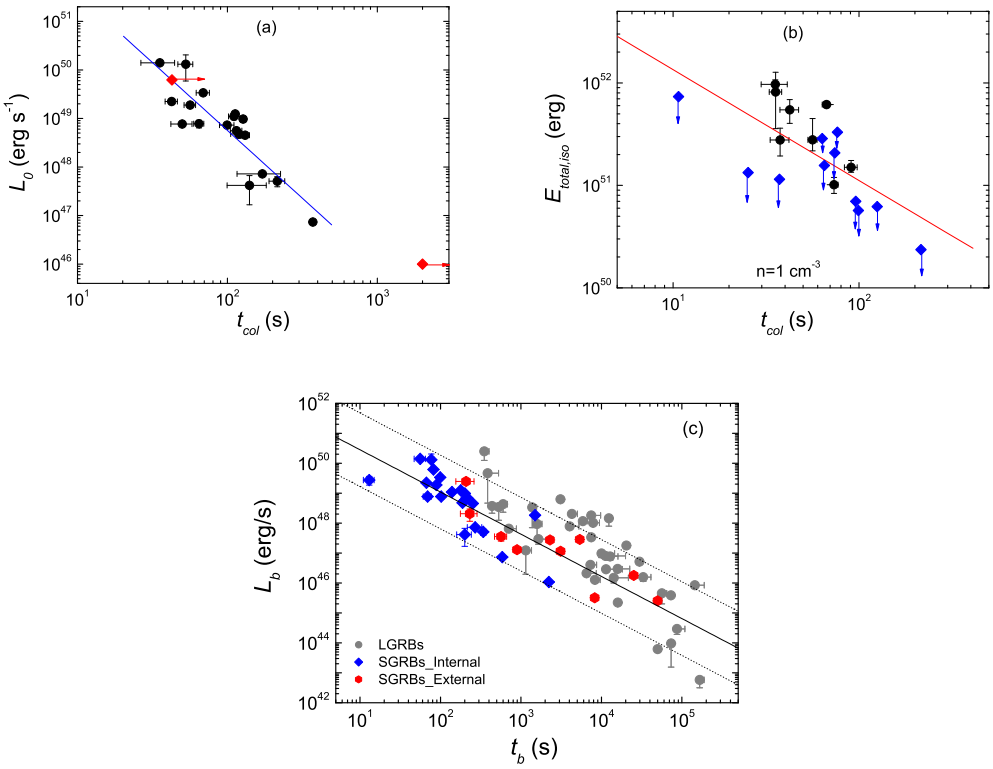

Figure 38 (a): The $L_0 - t_{col}$ anti-correlation for our Internal samples. The red diamonds are GRB 061201 and GRB 070714B, and the arrows denote the lower limits of the collapse time. (b): The $E_{\rm total,iso} - t_{col}$ anti-correlation for our Internal sample using $n = 1$ cm^{-3} to calculate $E_{\rm K,iso}$. The blue diamonds indicate the upper limits to calculate $E_{\rm K,iso}$, and the red solid line is the best fitting line. (c): The empirical $L_b - t_b$ correlation derived from the short GRBs in our sample (red for External and blue for Internal samples) compared with the Dainotti relation for long GRBs (grey). The solid line is the best power-law fit to the SGRBs sample, and the two dotted lines denote the 2σ region of the fit.

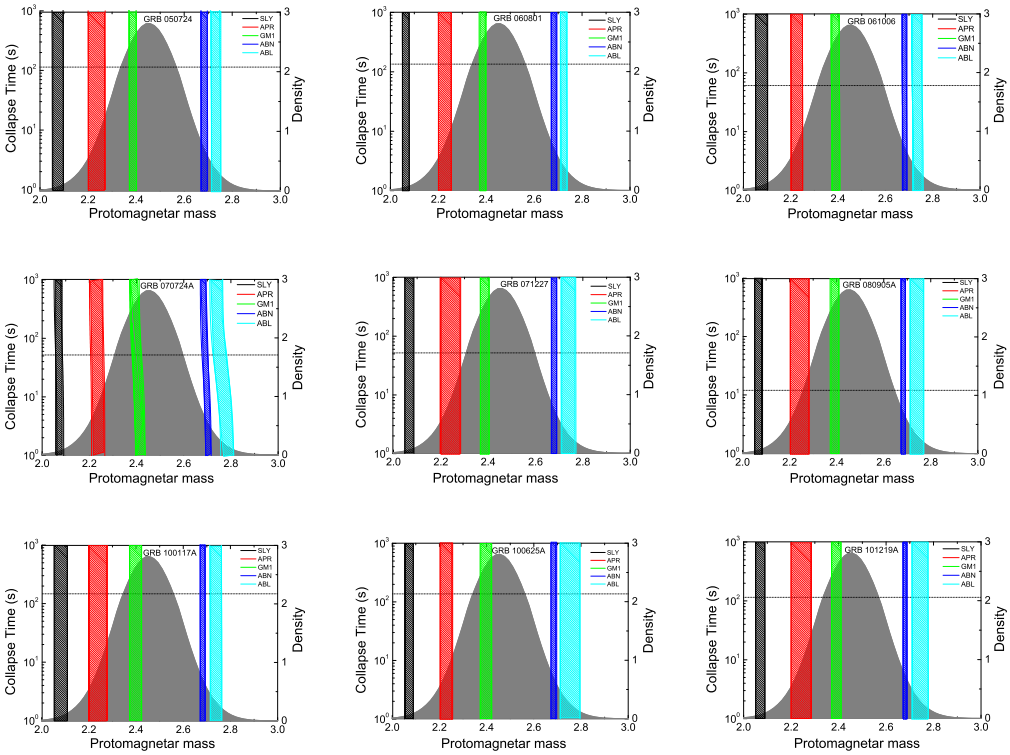

Figure 39 The collapse time as a function of the protomagnetar mass. The shaded region is the protomagnetar mass distribution derived from the total mass distribution of the Galactic NS-NS binary systems. The predicted results for 5 equations-of-state are shown in each panel: SLy (black), APR (red), GM1 (green), AB-N (blue), AB-L (cyan). The horizontal dot line is the observed collapse time for each GRB.

REFERENCES

Abdo, A. A., Ackermann, M., Arimoto, M., et al. 2009, Science, 323, 1688

Abramowicz, M. A., Czerny, B., Lasota, J. P., & Szuszkiewicz, E. 1988, ApJ, 332, 646

Akmal, A., Pandharipande, V. R., & Ravenhall, D. G. 1998, Phys. Rev. C, 58, 1804

Amati, L., Guidorzi, C., Frontera, F., et al. 2008, MNRAS, 391, 577

Arnett, W. D., & Bowers, R. L. 1977, ApJ, 33, 415

Axelsson, M., Baldini, L., Barbiellini, G., et al. 2012, ApJ, 757, L31

Band, D., Matteson, J., Ford, L., et al. 1993, ApJ, 413, 281

Bannister, K. W., Murphy, T., Gaensler, B. M., & Reynolds, J. E. 2012, ApJ, 757, 38

Barthelmy, S. D., Chincarini, G., Burrows, D. N., et al. 2005, Nature, 438, 994

Begelman, M. C. 1978, MNRAS, 184, 53

Berger, E., Kulkarni, S. R., Fox, D. B., et al. 2005, ApJ, 634, 501

Berger, E., Price, P. A., Cenko, S. B., et al. 2005, Nature, 438, 988

Berger, E. 2014, Annual Review of Astronomy and Astrophysics, 52, 43

Bernardini, M. G., Campana, S., Ghisellini, G., et al. 2013, ApJ, 775, 67

Blandford, R. D., & Znajek, R. L. 1977, MNRAS, 179, 433

Bloom, J. S., Kulkarni, S. R., & Djorgovski, S. G. 2002, AJ, 123, 1111

Bloom, J. S., Kulkarni, S. R., Djorgovski, S. G., et al. 1999, Nature, 401, 453

Bloom, J. S., Prochaska, J. X., Pooley, D., et al. 2006, ApJ, 638, 354

Bloom, J. S., Frail, D. A., & Sari, R. 2001, AJ, 121, 2879

Bonnell, J. T., Norris, J. P., Nemiroff, R. J., & Scargle, J. D. 1997, ApJ, 490, 79

Briggs, M. S., Band, D. L., Kippen, R. M., et al. 1999, ApJ, 524, 82

Bromberg, O., Nakar, E., Piran, T., & Sari, R. 2013, ApJ, 764, 179

Bromberg, O., Nakar, E., Piran, T., & Sari, R. 2012, ApJ, 749, 110

Bucciantini, N., Metzger, B. D., Thompson, T. A., & Quataert, E. 2012, MNRAS, 419, 1537

Bucciantini, N., Quataert, E., Arons, J., Metzger, B. D., & Thompson, T. A. 2008, MNRAS, 383, L25

Burrows, D. N., Romano, P., Falcone, A., et al. 2005, Science, 309, 1833

Burrows, D. N., Grupe, D., Capalbi, M., et al. 2006, ApJ, 653, 468

Butler, N. R., Kocevski, D., Bloom, J. S., & Curtis, J. L. 2007, ApJ, 671, 656

Campana, S., Mangano, V., Blustin, A. J., et al. 2006, Nature, 442, 1008

Campana, S., Tagliaferri, G., Lazzati, D., et al. 2006, A&A, 454, 113

Cenko, S. B., Perley, D. A., Junkkarinen, V., et al. 2009, GRB Coordinates Network, 9518, 1

Chen, P., & Labun, L. 2013, Phys. Rev. D, 88, 083006

Chen, W.-X., & Beloborodov, A. M. 2007, ApJ, 657, 383

Cheng, K. S., & Dai, Z. G. 1996, Physical Review Letters, 77, 1210

Chincarini, G., Mao, J., Margutti, R., et al. 2010, MNRAS, 406, 2113

Ciolfi, R., & Siegel, D. M. 2015, ApJ, 798, LL36

Cook, G. B., Shapiro, S. L., & Teukolsky, S. A. 1994, ApJ, 424, 823

Costa, E., Frontera, F., Heise, J., et al. 1997, Nature, 387, 783

Cucchiara, A., Levan, A. J., Fox, D. B., et al. 2011, ApJ, 736, 7

Cucchiara, A., Prochaska, J. X., Perley, D., et al. 2013, ApJ, 777, 94

Cui, X.-H., Nagataki, S., Aoi, J., & Xu, R.-X. 2012, Research in Astronomy and Astrophysics, 12, 1255

D'Avanzo, P., D'Elia, V., & Covino, S. 2008, GRB Coordinates Network, 8350, 1

Dai, Z. G. 2004, ApJ, 606, 1000

Dai, Z. G., & Lu, T. 1998, Physical Review Letters, 81, 4301

Dai, Z. G., & Lu, T. 1998, A&A, 333, L87

Dai, Z. G., Wang, X. Y., Wu, X. F., & Zhang, B. 2006, Science, 311, 1127

Dainotti, M. G., Willingale, R., Capozziello, S., Fabrizio Cardone, V., & Ostrowski, M. 2010, ApJ, 722, L215

Dall'Osso, S., Stratta, G., Guetta, D., et al. 2011, A&A, 526, AA121

Della Valle, M., Chincarini, G., Panagia, N., et al. 2006, Nature, 444, 1050

Deng, W., & Zhang, B. 2014, ApJ, 783, LL35

di Serego Alighieri, S., Ni, W.-T., & Pan, W.-P. 2014, ApJ, 792, 35

Douchin, F., & Haensel, P. 2001, A&A, 380, 151

Duez, M. D., Liu, Y. T., Shapiro, S. L., Shibata, M., & Stephens, B. C. 2006, Physical Review Letters, 96, 031101

Eichler, D., Livio, M., Piran, T., & Schramm, D. N. 1989, Nature, 340, 126

Evans, P. A., Beardmore, A. P., Page, K. L., et al. 2009, MNRAS, 397, 1177

Falcke, H., & Rezzolla, L. 2014, A&A, 562, AA137

Fan, Y. Z., Zhang, B., Kobayashi, S., & Mészáros, P. 2005, ApJ, 628, 867

Fan, Y.-Z., Wu, X.-F., & Wei, D.-M. 2013, Phys. Rev. D, 88, 067304

Fan, Y.-Z., & Xu, D. 2006, MNRAS, 372, L19

Fan, Y.-Z., Yu, Y.-W., Xu, D., et al. 2013, ApJ, 779, LL25

Fan, Y.-Z., Zhang, B.-B., Xu, D., Liang, E.-W., & Zhang, B. 2011, ApJ, 726, 32

Fenimore, E. E., Madras, C. D., & Nayakshin, S. 1996, ApJ, 473, 998

Fishman, G. J., & Meegan, C. A. 1995, Annual Review of Astronomy and Astrophysics, 33, 415

Fong, W., & Berger, E. 2013, ApJ, 776, 18

Fong, W., Berger, E., Chornock, R., et al. 2013, ApJ, 769, 56

Fong, W., Berger, E., Chornock, R., et al. 2011, ApJ, 730, 26

Fong, W., Berger, E., & Fox, D. B. 2010, ApJ, 708, 9

Fong, W., Berger, E., Metzger, B. D., et al. 2014, ApJ, 780, 118

Fox, D. B., Frail, D. A., Price, P. A., et al. 2005, Nature, 437, 845

Frail, D. A., Kulkarni, S. R., Sari, R., et al. 2001, ApJ, 562, L55

Freiburghaus, C., Rosswog, S., & Thielemann, F.-K. 1999, ApJ, 525, L121

Fruchter, A. S., Levan, A. J., Strolger, L., et al. 2006, Nature, 441, 463

Fryer, P., Taylor, B., Langmuir, C. H., & Hochstaedter, A. G. 1990, Earth and Planetary Science Letters, 100, 161

Fynbo, J. P. U., Watson, D., Thöne, C. C., et al. 2006, Nature, 444, 1047

Gal-Yam, A., Fox, D. B., Price, P. A., et al. 2006, Nature, 444, 1053

Galama, T. J., Vreeswijk, P. M., van Paradijs, J., et al. 1998, Nature, 395, 670

Gao, H., Ding, X., Wu, X.-F., Zhang, B., & Dai, Z.-G. 2013, ApJ, 771, 86

Gao, H., Lei, W.-H., Zou, Y.-C., Wu, X.-F., & Zhang, B. 2013, New Astron. Rev., 57, 141

Gao, H., Li, Z., & Zhang, B. 2014, ApJ, 788, 189

Gao, W.-H., & Fan, Y.-Z. 2006, Chin. J. Astron. Astrophys., 6, 513

Gehrels, N., Chincarini, G., Giommi, P., et al. 2004, ApJ, 611, 1005

Gehrels, N., Norris, J. P., Barthelmy, S. D., et al. 2006, Nature, 444, 1044

Gehrels, N., Sarazin, C. L., O'Brien, P. T., et al. 2005, Nature, 437, 851

Ghisellini, G., Ghirlanda, G., Nava, L., & Firmani, C. 2007, ApJ, 658, L75

Ghisellini, G., Ghirlanda, G., Nava, L., & Celotti, A. 2010, MNRAS, 403, 926

Giacomazzo, B., & Perna, R. 2013, ApJ, 771, LL26

Glendenning, N. K., & Moszkowski, S. A. 1991, Physical Review Letters, 67, 2414

Gompertz, B. P., O'Brien, P. T., & Wynn, G. A. 2014, MNRAS, 438, 240

Gompertz, B. P., O'Brien, P. T., Wynn, G. A., & Rowlinson, A. 2013, MNRAS, 431, 1745

Greiner, J., Krühler, T., Fynbo, J. P. U., et al. 2009, ApJ, 693, 1610

Grupe, D., Gronwall, C., Wang, X.-Y., et al. 2007, ApJ, 662, 443

Hakkila, J., Haglin, D. J., Pendleton, G. N., et al. 2000, ApJ, 538, 165

Hjorth, J., Sollerman, J., Møller, P., et al. 2003, Nature, 423, 847

Horváth, I. 1998, ApJ, 508, 757

Horváth, I., Bagoly, Z., Balázs, L. G., et al. 2010, ApJ, 713, 552

Hotokezaka, K., Kiuchi, K., Kyutoku, K., et al. 2013, Phys. Rev. D, 88, 044026

Hotokezaka, K., Kiuchi, K., Kyutoku, K., et al. 2013, Phys. Rev. D, 87, 024001

Hu, Y.-D., Liang, E.-W., Xi, S.-Q., et al. 2014, ApJ, 789, 145

Hullinger, D., Barbier, L., Barthelmy, S., et al. 2005, GRB Coordinates Network, 4400, 1

Kann, D. A., Klose, S., Zhang, B., et al. 2011, ApJ, 734, 96

Katz, J. I. 1977, ApJ, 215, 265

Kiziltan, B., Kottas, A., De Yoreo, M., & Thorsett, S. E. 2013, ApJ, 778, 66

Klebesadel, R. W., Strong, I. B., & Olson, R. A. 1973, ApJ, 182, L85

Kluźniak, W., & Ruderman, M. 1998, ApJ, 505, L113

Kocevski, D., & Petrosian, V. 2013, ApJ, 765, 116

Kocevski, D., & West, A. A. 2011, ApJ, 735, LL8

Koshut, T. M., Paciesas, W. S., Kouveliotou, C., et al. 1996, ApJ, 463, 570

Kouveliotou, C., Meegan, C. A., Fishman, G. J., et al. 1993, ApJ, 413, L101

Kumar, P., Narayan, R., & Johnson, J. L. 2008, MNRAS, 388, 1729

Kumar, P., Narayan, R., & Johnson, J. L. 2008, Science, 321, 376

Kumar, P., & Panaitescu, A. 2000, ApJ, 541, L9

Kumar, P., & Zhang, B. 2014, arXiv:1410.0679

Lü, H.-J., Liang, E.-W., Zhang, B.-B., & Zhang, B. 2010, ApJ, 725, 1965

Lü, H.-J., & Zhang, B. 2014, ApJ, 785, 74

Lü, H.-J., Zhang, B., Liang, E.-W., Zhang, B.-B., & Sakamoto, T. 2014, MNRAS, 442, 1922

Landsman, W., de Pasquale, M., Kuin, P., et al. 2008, GRB Coordinates Network, 8601, 1

Lasky, P. D., Haskell, B., Ravi, V., Howell, E. J., & Coward, D. M. 2014, Phys. Rev. D, 89, 047302

Lattimer, J. M., & Prakash, M. 2004, Science, 304, 536

Lattimer, J. M., Prakash, M., Masak, D., & Yahil, A. 1990, ApJ, 355, 241

Lee, H. K., Wijers, R. A. M. J., & Brown, G. E. 2000, Physics Reports, 325, 83

Lei, W. H., Wang, D. X., Zhang, L., et al. 2009, ApJ, 700, 1970

Lei, W.-H., Zhang, B., & Liang, E.-W. 2013, ApJ, 765, 125

Leibler, C. N., & Berger, E. 2010, ApJ, 725, 1202

Levan, A. J., Fynbo, J. P. U., Hjorth, J., et al. 2009, GRB Coordinates Network, 9958, 1

Levesque, E. M., Bloom, J. S., Butler, N. R., et al. 2010, MNRAS, 401, 963

Li, L.-X. 2000, Phys. Rev. D, 61, 084016

Liang, E.-W., Lü, H.-J., Hou, S.-J., Zhang, B.-B., & Zhang, B. 2009, ApJ, 707, 328

Liang, E.-W., Racusin, J. L., Zhang, B., Zhang, B.-B., & Burrows, D. N. 2008, ApJ, 675, 528

Liang, E.-W., Yi, S.-X., Zhang, J., et al. 2010, ApJ, 725, 2209

Liang, E.-W., Zhang, B.-B., & Zhang, B. 2007, ApJ, 670, 565

Lithwick, Y., & Sari, R. 2001, ApJ, 555, 540

Liu, T., Liang, E.-W., Gu, W.-M., et al. 2012, ApJ, 760, 63

Lloyd-Ronning, N. M., & Zhang, B. 2004, ApJ, 613, 477

Lorimer, D. R., Bailes, M., McLaughlin, M. A., Narkevic, D. J., & Crawford, F. 2007, Science, 318, 777

Lu, R.-J., Wei, J.-J., Qin, S.-F., & Liang, E.-W. 2012, ApJ, 745, 168

Lyford, N. D., Baumgarte, T. W., & Shapiro, S. L. 2003, ApJ, 583, 410

Lyons, N., O'Brien, P. T., Zhang, B., et al. 2010, MNRAS, 402, 705

Margutti, R., Guidorzi, C., Chincarini, G., et al. 2010, MNRAS, 406, 2149

Mészáros, P., & Rees, M. J. 1997, ApJ, 482, L29

Meszaros, P., & Rees, M. J. 1993, ApJ, 405, 278

Mészáros, P. 2006, Reports on Progress in Physics, 69, 2259

MacFadyen, A. I., & Woosley, S. E. 1999, ApJ, 524, 262

Markwardt, C. B. 2009, Astronomical Data Analysis Software and Systems XVIII, 411, 251

Meegan, C. A., Fishman, G. J., Wilson, R. B., et al. 1992, Nature, 355, 143

Metzger, B. D., Giannios, D., Thompson, T. A., Bucciantini, N., & Quataert, E. 2011, MNRAS, 413, 2031

Metzger, M. R., Djorgovski, S. G., Kulkarni, S. R., et al. 1997, Nature, 387, 878

Metzger, B. D., Quataert, E., & Thompson, T. A. 2008, MNRAS, 385, 1455

Metzger, B. D., & Piro, A. L. 2014, MNRAS, 439, 3916

Mukherjee, S., Feigelson, E. D., Jogesh Babu, G., et al. 1998, ApJ, 508, 314

Mundell, C. G., Melandri, A., Guidorzi, C., et al. 2007, ApJ, 660, 489

Narayan, R., Paczynski, B., & Piran, T. 1992, ApJ, 395, L83

Narayan, R., Piran, T., & Kumar, P. 2001, ApJ, 557, 949

Nemmen, R. S., Georganopoulos, M., Guiriec, S., et al. 2012, Science, 338, 1445

Norris, J. P., & Bonnell, J. T. 2006, ApJ, 643, 266

Nousek, J. A., Kouveliotou, C., Grupe, D., et al. 2006, ApJ, 642, 389

O'Brien, P. T., Willingale, R., Osborne, J., et al. 2006, ApJ, 647, 1213

Paczynski, B. 1986, ApJ, 308, L43

Paczynski, B. 1991, , 41, 157

Paczynski B., 1991, AcA, 41, 257

Panaitescu, A., & Kumar, P. 2002, ApJ, 571, 779

Panaitescu, A., Mészáros, P., Burrows, D., et al. 2006, MNRAS, 369, 2059

Perley, D. A., Metzger, B. D., Granot, J., et al. 2009, ApJ, 696, 1871

Pian, E., Mazzali, P. A., Masetti, N., et al. 2006, Nature, 442, 1011

Popham, R., Woosley, S. E., & Fryer, C. 1999, ApJ, 518, 356

Qin, Y., Liang, E.-W., Liang, Y.-F., et al. 2013, ApJ, 763, 15

Qin, Y.-P. 2008, ApJ, 683, 900

Racusin, J. L., Karpov, S. V., Sokolowski, M., et al. 2008, Nature, 455, 183

Racusin, J. L., Liang, E. W., Burrows, D. N., et al. 2009, ApJ, 698, 43

Ravi, V., & Lasky, P. D. 2014, MNRAS, 441, 2433

Rees, M. J., & Meszaros, P. 1994, ApJ, 430, L93

Rees, M. J., & Meszaros, P. 1992, MNRAS, 258, 41P

Rees, M. J., & Mészáros, P. 1998, ApJ, 496, L1

Rezzolla, L., Baiotti, L., Giacomazzo, B., Link, D., & Font, J. A. 2010, Classical and Quantum Gravity, 27, 114105

Rezzolla, L., Giacomazzo, B., Baiotti, L., et al. 2011, ApJ, 732, LL6

Rezzolla, L., & Kumar, P. 2014, arXiv:1410.8560

Roming, P. W. A., Kennedy, T. E., Mason, K. O., et al. 2005, Space Sci. Rev., 120, 95

Rosswog, S., Ramirez-Ruiz, E., & Davies, M. B. 2003, MNRAS, 345, 1077

Rowlinson, A., Gompertz, B. P., Dainotti, M., et al. 2014, MNRAS, 443, 1779

Rowlinson, A., O'Brien, P. T., Metzger, B. D., Tanvir, N. R., & Levan, A. J. 2013, MNRAS, 430, 1061

Rowlinson, A., O'Brien, P. T., Tanvir, N. R., et al. 2010, MNRAS, 409, 531

Ruffert, M., Janka, H.-T., Takahashi, K., & Schaefer, G. 1997, A&A, 319, 122

Ryde, F., Axelsson, M., Zhang, B. B., et al. 2010, ApJ, 709, L172

Sakamoto, T., Barthelmy, S. D., Barbier, L., et al. 2008, ApJ, 175, 179

Sakamoto, T., Barthelmy, S. D., Baumgartner, W. H., et al. 2011, ApJ, 195, 2

Sakamoto, T., Hill, J. E., Yamazaki, R., et al. 2007, ApJ, 669, 1115

Sakamoto, T., Sato, G., Barbier, L., et al. 2009, ApJ, 693, 922

Salvaterra, R., Campana, S., Vergani, S. D., et al. 2012, ApJ, 749, 68

Salvaterra, R., Della Valle, M., Campana, S., et al. 2009, Nature, 461, 1258

Sari, R., & Mészáros, P. 2000, ApJ, 535, L33

Sari, R., & Piran, T. 1999, A&AS, 138, 537

Schady, P., de Pasquale, M., Page, M. J., et al. 2007, MNRAS, 380, 1041

Schmidt, M. 2001, ApJ, 552, 36

Schmidt, M., Higdon, J. C., & Hueter, G. 1988, ApJ, 329, L85

Shapiro, S. L., & Teukolsky, S. A. 1983, Research supported by the National Science Foundation. New York, Wiley-Interscience, 1983, 663 p.,

Siegel, D. M., Ciolfi, R., & Rezzolla, L. 2014, ApJ, 785, LL6

Soderberg, A. M., Berger, E., Kasliwal, M., et al. 2006, ApJ, 650, 261

Stanek, K. Z., Matheson, T., Garnavich, P. M., et al. 2003, ApJ, 591, L17

Tanvir, N. R., Fox, D. B., Levan, A. J., et al. 2009, Nature, 461, 1254

Thöne, C. C., Campana, S., Lazzati, D., et al. 2011, MNRAS, 414, 479

Thompson, C. 1994, MNRAS, 270, 480

Thornton, D., Stappers, B., Bailes, M., et al. 2013, Science, 341, 53

Troja, E., Cusumano, G., O'Brien, P. T., et al. 2007, ApJ, 665, 599

Uhm, Z. L., Zhang, B., Hascoët, R., et al. 2012, ApJ, 761, 147

Usov, V. V. 1992, Nature, 357, 472

Valentim, R., Rangel, E., & Horvath, J. E. 2011, MNRAS, 414, 1427

Virgili, F. J., Qin, Y., Zhang, B., & Liang, E. 2012, MNRAS, 424, 2821

Virgili, F. J., Zhang, B., O'Brien, P., & Troja, E. 2011, ApJ, 727, 109

von Kienlin, A., Meegan, C. A., Paciesas, W. S., et al. 2014, ApJ, 211, 13

Vreeswijk, P. M., Fynbo, J. P. U., Malesani, D., Hjorth, J., & de Ugarte Postigo, A. 2008, GRB Coordinates Network, 8191, 1

Wheeler, J. C., Yi, I., Höflich, P., & Wang, L. 2000, ApJ, 537, 810

Wiersema, K., Levan, A., Kamble, A., Tanvir, N., & Malesani, D. 2009, GRB Coordinates Network, 9673, 1

Willingale, R., O'Brien, P. T., Osborne, J. P., et al. 2007, ApJ, 662, 1093

Woosley, S. E. 1993, ApJ, 405, 273

Xin, L.-P., Liang, E.-W., Wei, J.-Y., et al. 2011, MNRAS, 410, 27

Xu, D., de Ugarte Postigo, A., Leloudas, G., et al. 2013, ApJ, 776, 98

Xu, M., & Huang, Y. F. 2012, A&A, 538, AA134

Yi, S. X., Dai, Z. G., Wu, X. F., & Wang, F. Y. 2014, arXiv:1401.1601

Yost, S. A., Harrison, F. A., Sari, R., & Frail, D. A. 2003, ApJ, 597, 459

Yu, Y. W., & Dai, Z. G. 2007, A&A, 470, 119

Yu, Y.-W., Cheng, K. S., & Cao, X.-F. 2010, ApJ, 715, 477

Yu, Y.-W., Zhang, B., & Gao, H. 2013, ApJ, 776, LL40

Yuan, F., & Zhang, B. 2012, ApJ, 757, 56

Zalamea, I., & Beloborodov, A. M. 2011, MNRAS, 410, 2302

Zhang, B.-B., Liang, E.-W., & Zhang, B. 2007, ApJ, 666, 1002

Zhang, B.-B., Zhang, B., Liang, E.-W., et al. 2011, ApJ, 730, 141

Zhang, B.-B., Zhang, B., Murase, K., Connaughton, V., & Briggs, M. S. 2014, ApJ, 787, 66

Zhang, B. 2014, ApJ, 780, LL21

Zhang, B. 2013, ApJ, 763, LL22

Zhang, B. 2012, Death of Massive Stars: Supernovae and Gamma-Ray Bursts, 279, 102

Zhang, B. 2011, Comptes Rendus Physique, 12, 206

Zhang, B. 2006, Nature, 444, 1010

Zhang, B., Fan, Y. Z., Dyks, J., et al. 2006, ApJ, 642, 354

Zhang, B., Kobayashi, S., & Mészáros, P. 2003, ApJ, 595, 950

Zhang, B., Liang, E., Page, K. L., et al. 2007, ApJ, 655, 989

Zhang, B., & Mészáros, P. 2004, International Journal of Modern Physics A, 19, 2385

Zhang, B., & Mészáros, P. 2001, ApJ, 552, L35

Zhang, B., & Pe'er, A. 2009, ApJ, 700, L65

Zhang, B., & Yan, H. 2011, ApJ, 726, 90

Zhang, B., Zhang, B.-B., Liang, E.-W., et al. 2007, ApJ, 655, L25

Zhang, B., Zhang, B.-B., Virgili, F. J., et al. 2009, ApJ, 703, 1696

Zhang, F.-W., Shao, L., Yan, J.-Z., & Wei, D.-M. 2012, ApJ, 750, 88

Zhang, K., Wang, T.-G., Yan, L., & Dong, X.-B. 2013, ApJ, 768, 22

Zheng, Z., Ofek, E. O., Kulkarni, S. R., Neill, J. D., & Juric, M. 2014, ApJ, 797, 71

Zhou, B., Li, X., Wang, T., Fan, Y.-Z., & Wei, D.-M. 2014, Phys. Rev. D, 89, 107303

CURRICULUM VITA

Graduate College
University of Nevada, Las Vegas

HOUJUN Lü

Degrees:
Bachelor of Science 2007
Neijiang Normal University

Master of Science 2010
Guangxi University

Publication list of my Ph.D study:

[9] **HouJun Lü**, Bing Zhang, Weihua Lei, Ye Li, Paul D Lasky, *The Millisecond Magnetar central engine in short GRBs*,The Astrophysical Journal, (Accepted, arXiv:1501.02589), 2015.

[8] **HouJun Lü**, Bing Zhang. *A test of the millisecond magnetar central engine model of GRBs with Swift data*, The Astrophysical Journal, 785, 74, 2014

[7] **HouJun Lü**, Bing Zhang, En Wei Liang, Bin Bin Zhang, Sakamoto, Takanori, *The "amplitude" parameter of Gamma-Ray Bursts and its implications for GRB classification*, Monthly Notices of the Royal Astronomical Society, 422, 1922, 2014

[6] En-Wei Liang, Liang Li, He Gao, Bing Zhang, Yun-Feng Liang, Xue-Feng Wu, Shuang-Xi Yi, Zi-Gao Dai, Qing-Wen Tang, Jie-Min Chen, **Hou-Jun Lü**, Jin Zhang, Rui-Jing Lu, Lian-Zhong Lü, Jian-Yan Wei, *A Comprehensive Study of Gamma-Ray Burst Optical Emission. II. Afterglow Onset and Late Re-brightening Components*, The Astrophysics Journal 774,13, 2013

[5] Qin Ying, Liang En-Wei, Liang Yun-Feng, Yi Shuang-Xi, Lin Lin, Zhang Bin-Bin, Zhang Jin, **Lü Hou-Jun**, Lu Rui-Jing, Lü Lian-Zhong, Zhang Bing, *A Comprehensive Analysis of Fermi Gamma-Ray Burst Data. III. Energy-dependent T 90 Distributions of GBM GRBs and Instrumental Selection Effect on Duration Classification*, The Astrophysical Journal, 763, 15, 2013

[4] Lu Rui-Jing, Wei Jun-Jie, Liang En-Wei, Zhang Bin-Bin, **Lü Hou-Jun**, Lian-Zhong Lü, Lei Wei-Hua, Zhang Bing, *A Comprehensive Analysis of Fermi Gamma-ray Burst Data: II. E_{mp}-Evolution Patterns and Implications for the Observed Spectrum-Luminosity Relations*, The Astrophysical Journal, 756, 112, 2012

[3] Li Liang, Liang En-Wei, Tang Qing-Wen, Chen Jie-Min, Xi Shao-Qiang, **Lü Hou Jun**, Zhang Bing, Zhang Jin, Yi Shuang-Xi, Lu Rui-Jing, Lü Lian-Zhong, Wei Jian-Yan, *A Comprehensive Study of Gamma-Ray Burst Optical Emission: I. Flares and Early Shallow Decay Component*, The Astrophysical Journal, 758, 27, 2012

[2] Lü Jing, Zou Yuan-Chuan, Lei Wei-Hua, Zhang Bing, Wu Qing-Wen, Wang Ding-Xiong, Liang En-Wei, **Lü Hou-Jun**, *Lorentz Factor-Isotropic Luminosity/Energy Correlations of GRBS and Their Interpretation*, The Astrophysical Journal, 751, 49, 2012

[1] Jia Lan-Wei, Wu Xue-Feng, **Lü Hou-Jun**, Hou Shu-Jin, Liang En-Wei, *Physical origin of multi-wavelength emission of GRB 100418A and implications for its progenitor*, Research in Astronomy and Astrophysics, 12, 411, 2012

Dissertation Title:

CONSTRAINING THE PROGENITOR AND CENTRAL ENGINE OF GAMMA-RAY BURSTS WITH OBSERVATIONAL DATA

Dissertation Examination Committee:

Chairperson, Bing Zhang, Ph.D.

Committee Member, Daniel Proga, Ph.D.

Committee Member, Stephen Lepp, Ph.D.

Graduate Faculty Representative, Pengtao Sun, Ph.D.